Studies of Rotordynamic Forces Generated by Annular Flows

Thesis by

Robert V. Uy

In Partial Fulfillment of the Requirements

for the Degree of

Doctor of Philosophy

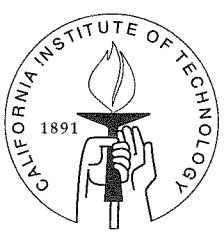

California Institute of Technology

Pasadena, California

1998

(Submitted May 27, 1998)

Acknowledgements

I would like to thank my advisor, Professor Christopher Brennen for his support, encouragement, and guidance during my years at Caltech. Professors Allan Acosta and Thomas Caughey provided valuable technical advice during the course of this project. I would also like to thank Professors Tim Colonius and Tony Leonard for their useful suggestions.

The help of Mike Gerfen of Central Engineering Services and John Van Deusen and Rodney Rojas of the Mechanical Engineering Shop with the construction of test articles and maintenence of the facility is greatly appreciated. I would also like to thank Dana Young, Cecilia Lin, and Jackie Beard for their help with administrative matters.

The assistance of Christopher Hunter, Brian Bircumshaw, Rajat Kongovi, Roberto Zenit, Joe Sivo, Dr. Yoshi Yoshida, and Yun Hsu with my research program is greatly appreciated. I would also like to express my gratitude to Anna Karion, Trish Waniewski, Clancy Rowley, Anders Carlson and Fabrizio D'Auria for help with the computers and system administration tasks.

I would like to thank Tony Eastland and George Prueger of the Rotating Machinery Analysis Division of Boeing North American for Rocketdyne's financial support and technical guidance.

Finally, my thanks to Mike, Donna, Cindy, Dave, Jeanne, Eric, and my parents Ligaya and Vicente for their unconditional support and encouragement during my stay at Caltech.

Abstract

Fluid-induced rotordynamic forces in pumping machinery are well documented but poorly understood. The present research focuses on the rotordynamics due to fluid flow in annuli, in particular, the discharge-to-suction leakage flow in centrifugal pumps. There are indications that the contribution of the front shroud leakage flow can be of the same order of magnitude as contributions from the nonuniform pressure acting on the impeller discharge. Previous investigations have established some of the basic traits of these flows. This work further elaborates both the experimental and computational approach to quantify and predict the shroud contribution to the rotordynamic stability of pumping machinery.

Experimental results presented show the contributions of the curvature of the leakage path to the rotordynamics both with and without inlet swirl. The effect of different inlet swirl rates at constant flow rate is examined. Anti-swirl devices are evaluated for their effectiveness in reducing instability. Geometrical changes to the high-pressure and low-pressure seals for the leakage path are quantified. All results are in good agreement with other reported measurements.

Childs' bulk flow model for leakage paths is carefully examined, and convective relations for vorticity and total pressure are deduced. This analysis suggests a new solution procedure of the bulk flow equations which does not resort to linearization or assumed harmonic forms of the flow variables.

Contents

List of Figures

List of Tables

Nomenclature

B	Depth of logarithmic spiral channel on swirl vane
C	Direct damping coefficient, normalized by $\rho\pi\omega^2 R_2^2 L\varepsilon$
c	Cross-coupled damping coefficient, normalized by $\rho\pi\omega^2 R_2^2 L\varepsilon$
DS, DT	Length increments in the s and θ direction
F_n	Force normal to whirl orbit normalized by $\rho\pi\omega^2 R_2^2 L\varepsilon$
F_t	Force tangent to whirl orbit normalized by $\rho\pi\omega^2 R_2^2 L\varepsilon$
g_S, g_R	Shear stresses in rotating coordinate system on the stator and rotor respectively
H	Clearance between impeller shroud and housing
h	Film thickness in Hir's Model
JS, JT	Mesh locations in the s and θ direction for the Streamfunction Vorticity Method
K	Direct stiffness coefficient, normalized by $\rho\pi\omega^2 R_2^2 L\varepsilon$
k	Cross-coupled stiffness coefficient, normalized by $\rho\pi\omega^2 R_2^2 L\varepsilon$
L	Axial length of the impeller
M	Direct added mass coefficient, normalized by $\rho\pi\omega^2 R_2^2 L\varepsilon$

m	Empirical frictional exponent in Hir's Model
m_R, m_S	Empirical frictional exponent for rotor and stator respectively
n	Empirical frictional constant for Hir's Model
n_R, n_S	Empirical frictional constants for rotor and stator respectively
P	Total pressure, defined in a rotating coordinate system in equation (4.18)
p	Static pressure
Q	Volumetric leakage flow rate
R	Radius of the rotor
R_2	Tip radius of rotor and leakage inlet
s	Path coordinate
u_s	Gap averaged leakage path velocity of fluid
u_θ	Gap averaged circumferential velocity of fluid
α	Turning angle of logarithmic spiral channel on swirl vane
β_1, β_2	Terms identified in Childs' perturbation model with significant effects on force resonance
Γ	The vorticity defined by equation (4.23)
ε	Eccentricity of whirl orbit
η	Dynamic viscosity in Hir's Model
Θ	Circumferential coordinate of the bulk flow model in fixed frame
θ	Circumferential coordinate in steady frame
Λ	Leakage inlet swirl ratio, $u_\theta/\omega R_2$
ν	Kinematic viscosity
ξ	Streamline coordinate
ρ	Fluid density

τ	Wall shear stress in Hir's Model
τ_{Ss}, τ_{Rs}	Wall shear stress terms in the s direction acting on the stator and rotor respectively
$\tau_{S\theta}, \tau_{R\theta}$	Wall shear stress terms in the θ direction acting on the stator and rotor respectively
ϕ	Leakage flow coefficient, $u_s/\omega R_2$
ψ	Stream function introduced in Streamfunction Vorticity method
Ω	Whirl radian frequency
ω	Main shaft radian frequency

Chapter 1 Introduction

1.1 Background

The presence of fluid-induced rotordynamic forces in turbomachinery has been well documented, but is still poorly understood. Previous studies have been conducted both experimentally and computationally, given the presence of such destabilizing forces and the problems that have been incurred by high-speed machinery. Increasing power requirements and size restrictions has meant a corresponding increase in the rotational speed of modern turbomachinery, and the fluid forces typically scale with the square of the rotational speed. Cases of fluid-induced forces altering the expected dynamic behavior of undersea petroleum, boiler feed, and rocket engine pumping applications have prompted investigations into the area of fluid/structure interactions in an attempt to predict the magnitude and onset of destablizing forces during the initial design of such machinery.

Fluid-induced rotordynamic forces can arise from many sources in rotating machinery. Seals and annuli formed by the both the front and rear shrouds of centrifugal pumps can have important effects. The blade interaction with stationary parts of a diffuser or volute and non-uniformities in the discharge can also give rise to rotordynamic effects. Much work has been done in the area of turbulent annular seals. Computations of the forces due to fluid flow in seals have proven to be fairly reliable.

The flow in the passage formed by the discharge-to-inlet leakage path of a shrouded centrifugal pump has been studied experimentally, but is still poorly characterized by models adapted from the analysis of turbulent annular seals. To now most attempts to computationally determine the destabilizing forces have met with limited success. In the design phase, the time and cost of full three-dimensional computational fluid dynamic codes has resulted in the need for simpler tools to analyze the effects of machine geometry on fluid-induced forces. The fluid processes in the annulus formed

by the front shroud of a centrifugal pump are highly complex and may not readily lend themselves to simple analysis. With this in mind, this thesis attempts to organize some new and some existing experimental data on effects of flow passage geometry, and documents some approaches to predicting the experimental data using computational schemes.

1.2 Notation

The dynamical behavior of a mass and rotating shaft is often characterized by the displacement of the mass from the axis of rotation as a function of the main shaft speed. The main shaft speed at which large displacements from the axis of rotation occur are termed critical speeds, and are similar to resonant frequencies of spring-mass-damper systems. In the case where the mass is a pump impeller, the fluid-induced forces can have significant effects on the dynamic behavior, changing the critical speeds of the shaft system and causing unforseen limitations to the operating range.

The hydrodynamic force acting on a rotor or impeller in a circular whirling orbit can be expressed as the sum of steady time averaged forces in the stationary frame and components due to instantaneous displacement of the rotor from the centerline. Using assumptions about the displacements due to the circular whirl orbit, the normal and tangential forces described below can be deduced. The details of this procedure have been well documented (Jery, 1986; Franz, 1989).

Figure 1.1 shows a schematic of the hydrodynamic forces that act on a rotating impeller whirling in a circular orbit. The unsteady fluid forces acting on the impeller due to the imposed whirl motion (eccentricity ϵ, whirl frequency Ω) are decomposed into a force normal to the direction of whirl motion, F_n, and a force in the direction of forward whirl motion, F_t. The normal and tangential forces are traditionally presented in dimensionless form as functions of the whirl frequency ratio, Ω/ω. More specifically, it is convenient for rotordynamicists to fit F_n, to a quadratic function of the whirl frequency ratio, Ω/ω, and to fit the dimensionless tangential force, F_t, to a linear

function. The resulting expressions are given by:

$$F_n = M\left(\frac{\Omega}{\omega}\right)^2 - c\left(\frac{\Omega}{\omega}\right) - K \tag{1.1}$$

$$F_t = -C\left(\frac{\Omega}{\omega}\right) + k \tag{1.2}$$

where the dimensionless coefficients are the direct added mass (M), direct damping (C), cross-coupled damping (c), direct stiffness (K), and the cross-coupled stiffness (k). It should be noted that the fluid-induced forces may not always conform to these simple functions of the whirl frequency ratio, however this assumption is common in rotordynamics literature. All five of the force coefficients are directly evaluated from curve fits of the graphs of F_n and F_t against Ω/ω.

For consideration of stability, a positive normal force F_n will cause the eccentricity to increase and hence be destabilizing. From equation 1.1, a large negative direct stiffness when no whirl motion is present ($\Omega/\omega = 0$) would correspond to such a case. When Ω/ω is positive, a positive tangential force F_t would also be destabilizing as this would drive the forward whirl motion. As can be seen from equation 1.2, a positive cross-coupled stiffness would correspond to such a condition, and also be the tangential force acting at zero whirl frequency ratio.

A convenient measure of the rotordynamic stability is the ratio of cross-coupled stiffness to the direct damping (i.e. k/C) which is termed the whirl ratio. This defines the range of positive whirl frequency ratios for which the tangential force is destabilizing.

1.3 Literature Survey

Fluid-induced rotordynamic forces can arise from any number of sources in modern high-speed turbomachinery. For example, work in turbulent annular seals has been carried out by many researchers (Childs, 1983a; Nordmann & Massmann, 1984; San Andres, 1993). A number of computational tools have been developed for turbulent annular seals which have proven reliable and useful. Perhaps the most simple of

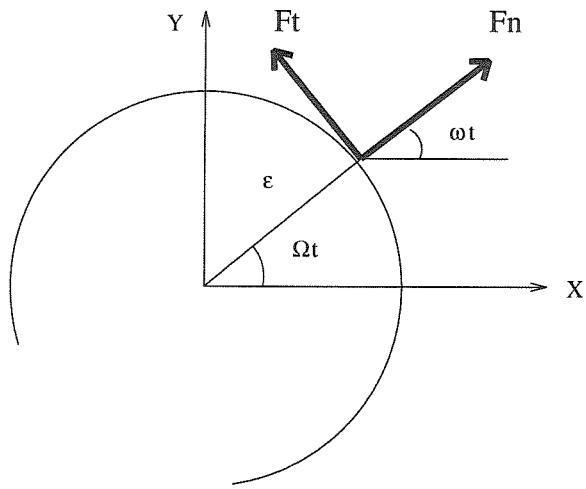

Figure 1.1: Schematic of the unsteady fluid-induced forces acting on an impeller whirling in a circular orbit.

these is the bulk flow model first proposed by Hirs and elaborated by Childs. Some significant results of this research were the experimental characterization of the rotordynamics of seals (Nordmann & Massmann, 1984), identification of the inertial terms as essential in modeling the forces (Childs, 1983a), and the sensitivity to inlet swirl of the bulk flow model (Childs, 1983b).

Some success has been acheived using the same bulk flow analysis in predicting the contributions of a centrifugal pump back shroud flow to forces and moments. Flow along the back shroud of an impeller can be important in applications such as multi-stage pumps where this type of leakage is possible. This flow and its resulting fluid force contributions have been examined experimentally and using a bulk flow analysis (Tsujimoto *et al.* , 1997). It was found that the unsteady wall shear stresses had only small effects on the flow in the passage, and that the the inlet loss condition played a significant role in the success of the bulk flow model.

On the opposite side of the back shroud, several investigations into the fluid-induced rotordynamic forces generated by discharge-to-suction leakage flows have been conducted. The contribution of the front shroud flow to the unsteady forces was identified in early work done at Caltech (Adkins & Brennen, 1988). Jery (1986)

used a dummy impeller with no vanes that matched the geometry of a normal test impeller to again examine the contribution of the shroud.

Bolleter (1987,1989) measured and quantified some of the effects of the front shroud geometry on the unsteady forces acting on a centrifugal pump using a rocking arm mechanism to vertically translate a spinning impeller. The forces reported by Bolleter were much larger than those reported by Adkins and Jery, and this was eventually attributed to the smaller clearances. The effect of a wear ring (radial clearance) seal was also measured and its contribution to the impeller forces determined. It was noted for the wear ring that a significant amount of the measured forces were due to the seal rather than the shroud. Table 1.1 shows the rotordynamic force coefficients for this wear ring seal and impeller. It should be noted that the nondimensionalization of these coefficients used the impeller discharge width rather than the leakage path axial length. For the normal force, a stabilizing effect on the direct stiffness, K, is noted for the seal. Bolleter, for the same wear ring geometry, also reports the effects of a swirl brake designed to reduce the inlet swirl into the seal, located near the discharge of the leakage path just upstream of the seal. With the anti-swirl brake, an increase in the direct stiffness and direct damping are noted. Decreases in the cross-coupled damping, cross-coupled stiffness, and direct added mass were also reported for this anti-swirl brake.

	K	k	C	c	M
Measured, total	1.5	12.3	8.8	8.5	6.5
Measured, seal	3.7	4.6	5.4	-.1	-.2
Difference, attributed to impeller	-2.2	7.7	3.4	8.6	6.7

Table 1.1: Force coefficients for wear ring impeller, Bolleter (1989)

To further investigate the front shroud force problem, Guinzburg (1992, 1993, 1994) examined the effect of eccentricity, rotational speed, and shroud clearance on the rotordynamic forces using a solid rotor to model the front shroud of an impeller. To summarize, the functional dependence of the rotordynamic forces on whirl frequency ratio was similar for the rotor and impellers. Including the eccentricity of the whirl

orbit in the nondimensionalization of the forces demonstrated that the forces scaled linearly. Shaft speeds from 500 to 2000 *rpm* were tested and the forces were shown to be independent of the shaft speed. The effect of increasing the flow rate was to cause the normal force to increase, while decreasing the region of foward whirl where the tangential force was destabilizing. The rotordynamic forces were roughly inversely porportional to the clearance, which explained the discrepancy between Bolleter's data and that from Caltech. Figure 1.2 shows the effect of clearance for selected tests (Guinzburg, 1992). The occurence of resonance like phenomena in the predictions of Childs' bulk flow model also led Guinzburg to examine the effect of swirl in the flow entering the leakage path. The effect of swirl was destabilizing on the rotordynamic forces. The rotordynamic force coefficients of these tests appear in figure 1.3. No resonances were observed in the experiments, leading to some controversy about the limitations of Childs' model.

To examine the possiblity of errors in the bulk flow approach, Sivo conducted measurements of the flow field in the annulus of the same model leakage path using laser doppler velocimetry (Sivo *et al.* , 1994b). Regions of flow recirculation and reversal were noted, especially close to the impeller near the tip. The results agreed qualitatively with other reported flow recirculation zones in the leakage passage of an impeller (Guelich *et al.* , 1989). Given the destabilizing nature of fluid pre-rotation into the leakage path, Sivo (1995) also investigated the effect of the anti-swirl devices in the leakage path for reducing the unsteady forces. Some benefit of these devices in reducing the unsteady forces was observed, mostly for very small flow rates. Figure 1.4 shows the rotordynamic force coefficients as functions of flow coefficient for a test with and without anti-swirl devices. Chapter 3 compares the data of Guinzburg and Sivo with results from the current research in more detail.

Other efforts have also concentrated on calculation of the leakage flow forces. A model with deformable finite elements, more complex than the traditional bulk flow analysis has proved capable of predicting the same flow reversal type phenomenon (Baskharone & Hensel, 1993) in the leakage flow. Baskharone's work points out some of the deficiencies in Childs' model in assuming a harmonic perturbation of the pres-

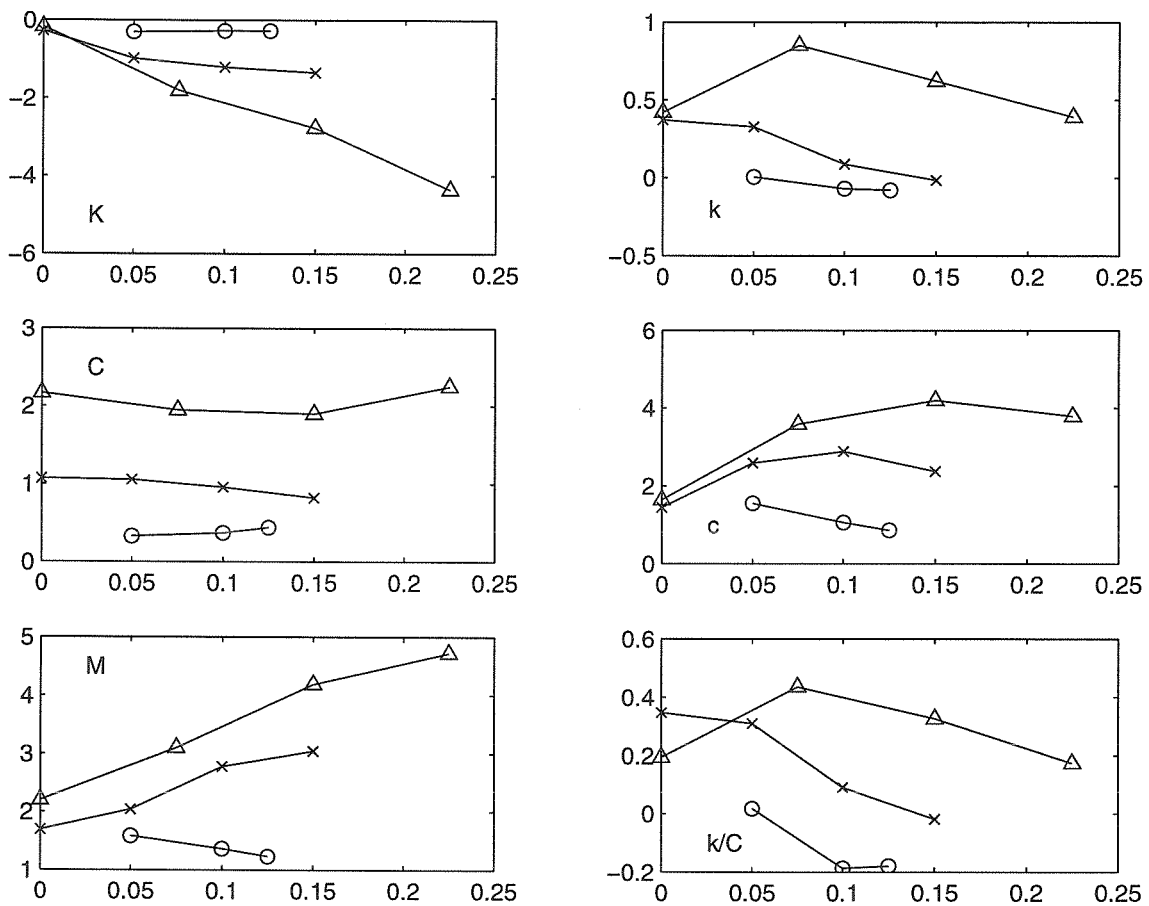

Figure 1.2: Rotordynamic coefficients versus flow coefficient ϕ at 1000 rpm, $\varepsilon = 0.118$ cm with $H = 0.140$ cm ($\triangle$), $H = 0.213$ cm ($\times$) and $H = 0.424$ cm ($\circ$). Guinzburg (1992)

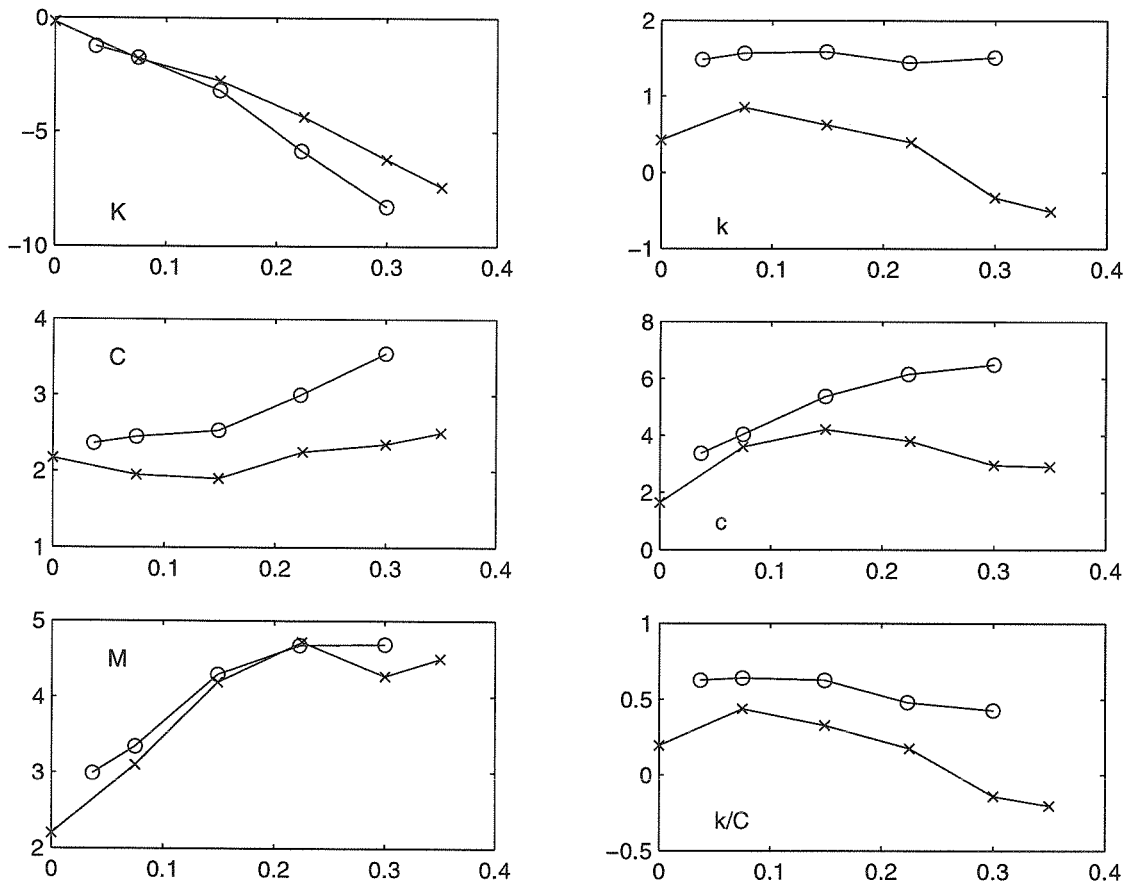

Figure 1.3: Rotordynamic coefficients versus flow coefficient ϕ at 1000 rpm, $H = 0.140$ cm, $\varepsilon = 0.118$ cm without inlet swirl ($\times$) and with inlet swirl ($\circ$). Guinzburg (1993)

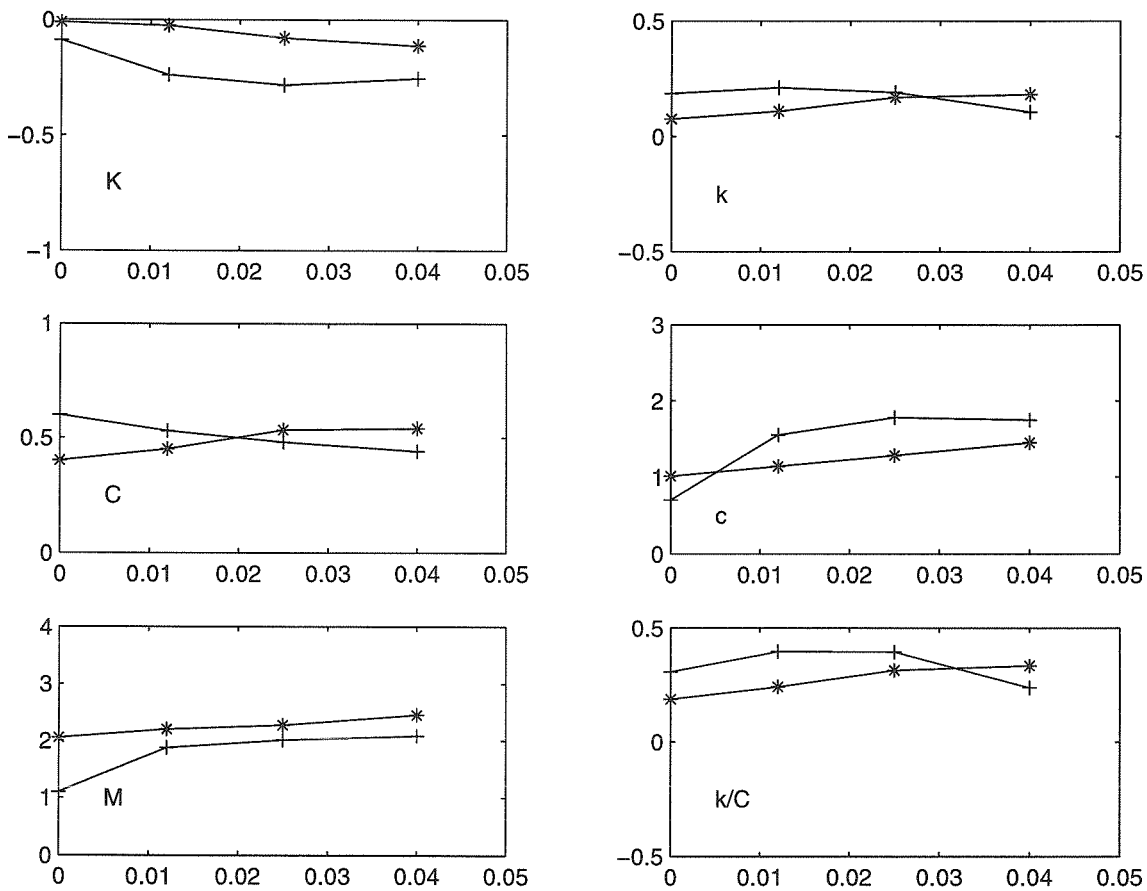

Figure 1.4: Rotordynamic coefficients versus flowcoefficient ϕ for the conical rotor with and without anti-swirl ribs. Data at 2000 rpm, for $H = 0.424$ cm, $\varepsilon = 0.118$ cm with $(*)$ and without $(+)$ anti-swirl devices (Sivo 1995).

sure, however the finite element model does not appear to predict the experimental forces with better accuracy. More experimental results can be expected from test-rigs using magnetic bearing technologies (Matros *et al.* , 1994).

1.4 Research Objective

The objective of this research is to further refine both the experimental and computational methods of studying and quantifying rotordynamic forces in discharge-to-suction leakage flows of centrifugal pump impellers.

Some new leakage path geometries more closely modeling those of typical centrifugal pumps will be examined, with some differences being noted from previous investigations. The bulk flow approach is examined in detail for insight into the physical properties of rotordynamic flows. A new solution approach with fewer assumptions about the functional form of the flow variables is proposed.

Chapter 2 Leakage Flow Test Apparatus

2.1 Rotor Force Test Facility

The experiments described in this work were conducted in the Rotor Force Test Facility at the California Institute of Technology. This apparatus has existed in one form or another for over 20 years (Ng, 1976), and has been used for various tests of turbomachinery and related components.

The present setup of the Rotor Force Test Facility (see figure 2.1) was first used by Jery (1986) to measure both the steady and unsteady fluid-induced forces on whirling centrifugal pump impellers. To measure the fluid forces on a rotating whirling pump without actually approaching the critical speed of the shaft and mass system, an eccentric drive was constructed to apply a whirl motion to the rotating main shaft. Jery describes the construction, operation and calibration of a six force component internal force balance, which was used to measure forces on rotating machinery (Jery, 1986).

The eccentric drive mechanism consists of a set of adjustable offset bearings and is used to impose a whirling motion onto the main rotation of the impeller. The radius of the whirl orbit (eccentricity) can be varied. Using a seperate belt drive connected to a whirl motor, the speed of the whirl orbit is varied throughout a range of subsynchronous whirl frequencies over the course of a typical test. The speeds of both the main motor and the whirl motor are set by a frequency divider box which has seperate outputs for two motor feedback controllers. The phase of the two motions is aligned with the aid of a strobe. The frequency divider box output is also sent to the data acquisition system, allowing the exact location of the impeller in both its main rotation and whirl rotation to be known at any given time.

An auxilliary pump has also been added to the existing loop, to simulate a leakage flow through the passages formed by the solid rotor. This device contains a

turbine flow meter and bypass loops which are adjusted manually by means of valves to regulate the flow rate. A schematic diagram of this unit appears in Guinzburg (Guinzburg, 1992). This device was used by both Guinzburg and Sivo.

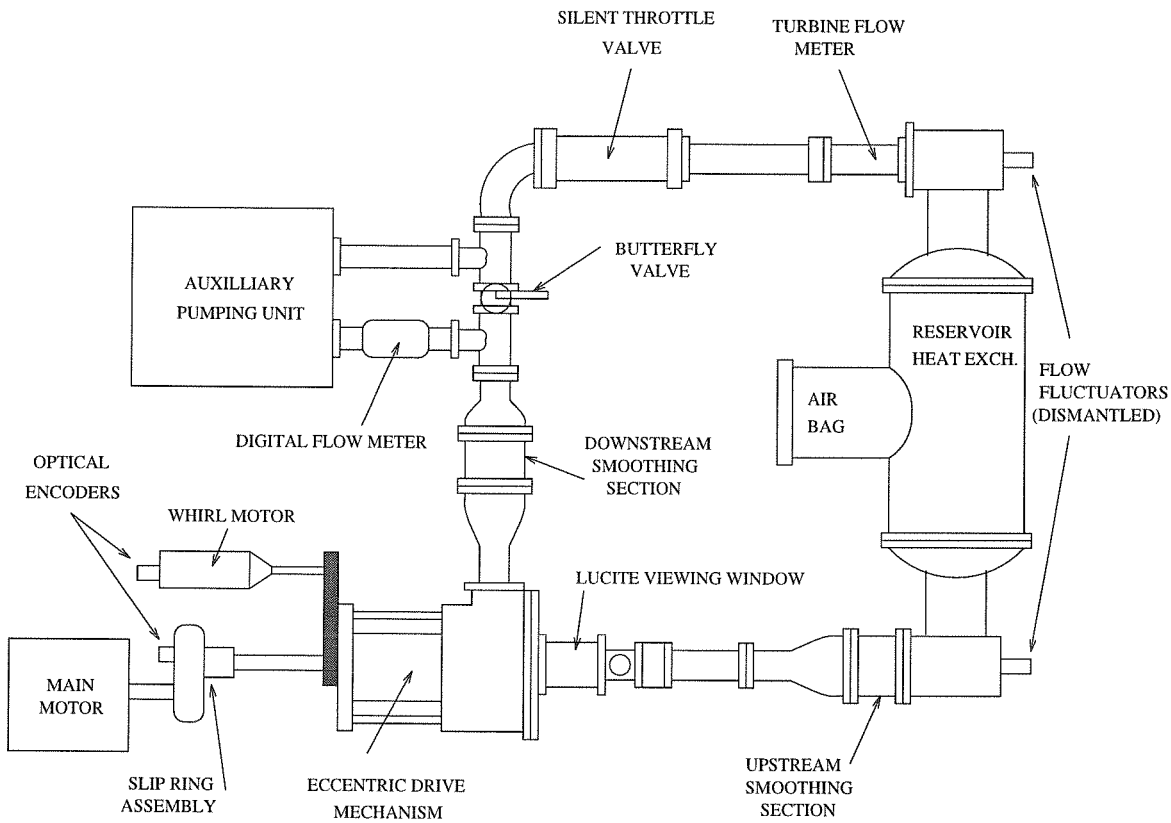

Figure 2.1: Schematic of the Rotor Force Test Facility.

Many components of the Rotor Force Test Facility were not used in the current tests. In particular, the silent throttle valve and turbine flow meter in the main loop were not employed as their functions were handled by the bypass valves and flow meter of the auxilliary pumping unit. The air bladder and heat exchanger were also not used for tests of the leakage flow.

The working fluid is water containing a solution of sodium chromate for corrosion inhibition, and pH balanced using potassium hydroxide. The main components of the test section apparatus consist of a solid or dummy impeller (rotor), a housing (stator), the rotating dynamometer (or internal force balance), the eccentric whirl

mechanism, and a leakage discharge seal. The full setup of the main test section is shown schematically in Figure 2.2. The main shaft is driven by a 15 kW motor through a reduction gear, offering speeds to around 3000 rpm. A slip ring assembly is located near the gearbox and allows a rotating connection between individual strain gauge bridges of the balance and the bridge amplifiers. The whirl motion is produced independently by a 1.5 kW motor, and is driven by a toothed belt and sprocket drive.

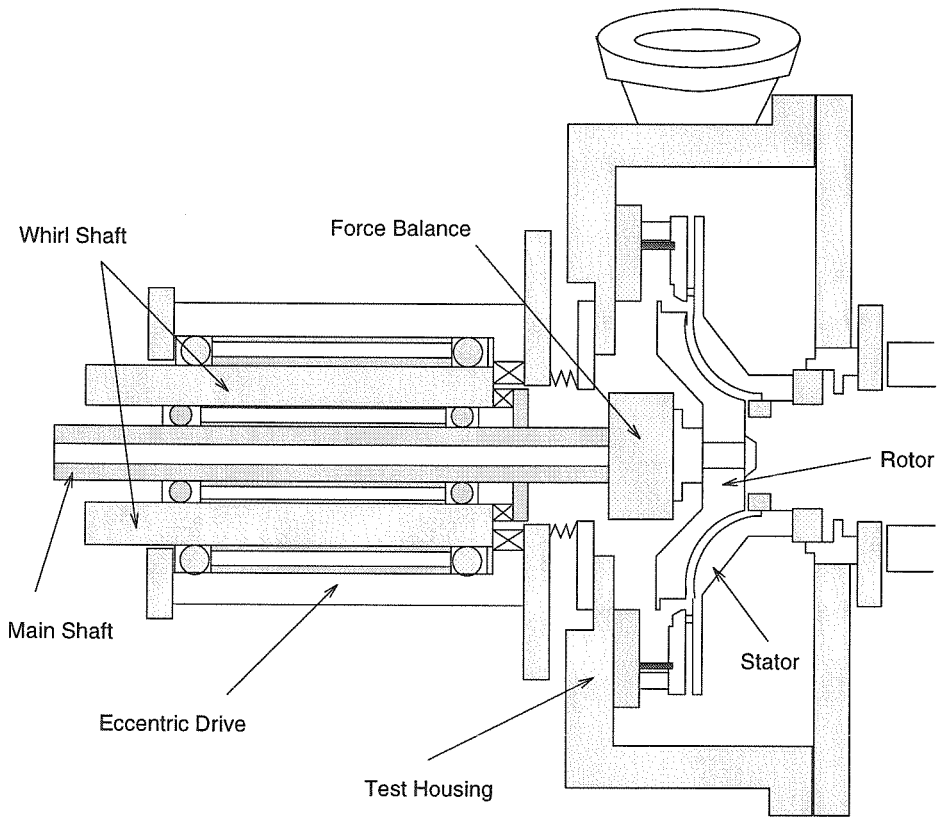

Figure 2.2: Experimental Setup, showing eccentric drive and contoured impeller.

In order to isolate the leakage flow forces in these experiments, a solid rotor was employed. The force contributions due to blade interactions with the volute are thereby negated. The dummy impeller, as closely as possible, attempts to model the front shroud clearance of a typical centrifugal pump. For these tests, fluid is forced through the housing "exit" and into the leakage path formed by the rotor and stator. It then exits to the rest of the loop of the RFTF through the "inlet" of the main

housing. Various ports on the main housing can be modified to allow manometer tubes and other instrument wiring to enter.

A range of suitable leakage flow rates was determined by examining data provided by Rocketdyne of typical pump operating parameters, and appears in Appendix A.

2.2 Leakage Paths

Experiments to compare different geometries of pump discharge-to-suction leakage paths were conducted in the Rotor Force Test Facility (RFTF). One experimental configuration, with the conical rotor and stator forming the leakage path, is shown in the center of Figure 2.3. This conical shroud with the straight 45 degree leakage path was extensively tested by Guinzburg and Sivo. The contoured rotor and stator form the leakage path depicted on the right of Figure 2.3. The conical model was constructed as a first approximation. The contoured rotor was made to match the axial length and eye-to-tip ratio (the ratio of an impeller's inlet diameter to the discharge diameter) of the conic model, but have more typical geometry. A final rotor and stator were made to model the leakage path of the Space Shuttle Main Engine (SSME) High Pressure Oxidizer Turbopump (HPOTP) as closely as possible. It was much shorter in axial length than the previous two impellers and has a much larger eye radius. Sketches and a table comparing the three paths are included in figure 2.3.

Both contoured rotors were designed using a 3rd order polynomial chosen such that the contour was parallel to the centerline at the eye and perpendicular to the centerline at the tip. A matching stator was constructed to maintain a constant normal clearance H=0.30 *cm*. The rotors and stators were machined using CNC controlled tooling. For ease of analysis, the tip radius (corresponding to the discharge radius of a pump) of all of the dummy impellers is the same.

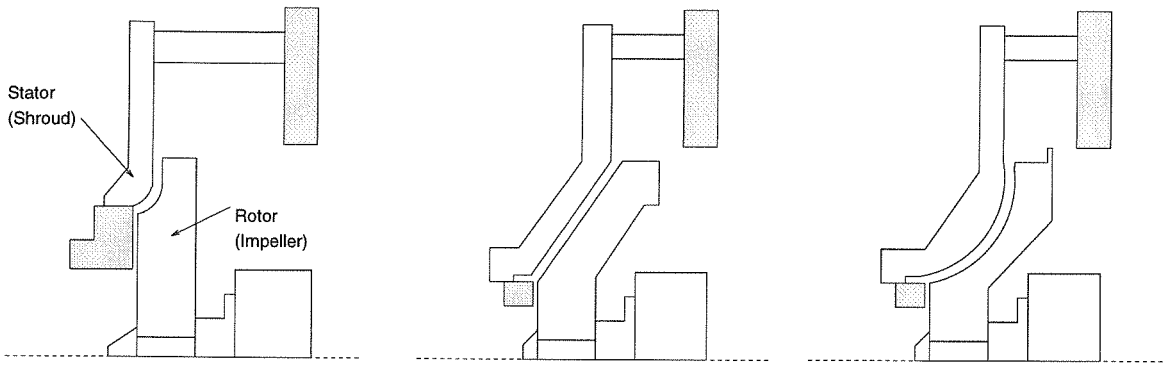

	Short Contoured Rotor	Conical Rotor	Contoured Rotor
Path	3rd order polynomial	45 degree straight	3rd order polynomial
Eye/tip diameter	.700	.474	.474
Axial length/ tip diameter	.088	.268	.229

Figure 2.3: Test matrix of rotor geometries

2.3 Seals

The low pressure side of the leakage path corresponds to the inlet or suction of a normal centrifugal pump (eye), while the high pressure side corresponds to the discharge of a typical pump (tip). Seals at both the low pressure and high pressure side of the rotor were used and their effects on the rotordynamic forces examined in the course of these investigations. A low pressure seal was always present, and this usually was an axial clearance device that modeled a typical face seal on a centrifugal pump. An axial clearance seal is typical of the low pressure seal found in many industrial centrifugal pump applications. This is illustrated in the right half of figure 2.4. The distance from the outer radius of the impeller eye to the inner radius of the axial clearance seal was 1.14 *cm*. The clearance was set to 0.05 *cm* for virtually all tests, but could be varied if necessary.

Figure 2.4 also shows a low pressure seal with radial clearance. The low pressure radial clearance seal models a turbulent annular seal. A radial clearance seal is typical in rocket engine designs, where a frictional contact seal may not be possible,

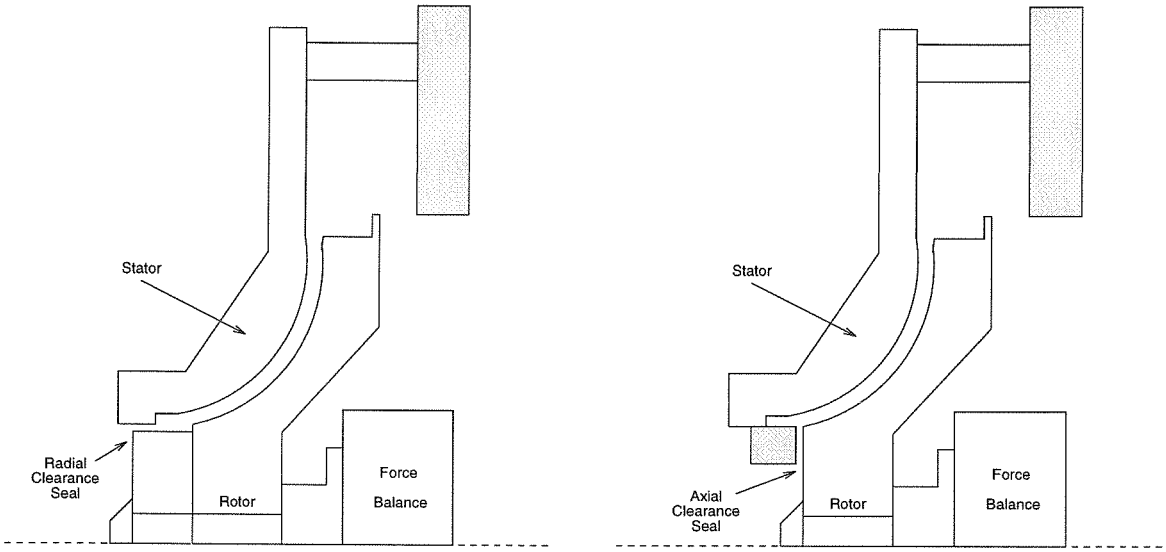

Figure 2.4: Experimental Configuration: Contoured rotor with radial clearance (left) and axial clearance (right) low pressure seal.

and losses induced by labyrinth type structures attempt to minimize leakage. The geometry was selected to match the leakage path volume (between the seal surface and the impeller) of the axial clearance seal for a direct comparison. A sealing section of axial length 0.51 *cm* was formed between the rotating member and the threads of the axial clearance seal on the stator. An imposed radial clearance of 0.09 *cm* was used to accomodate the eccentricity.

The high pressure seal tested took the form of an orifice formed by a stationary ring mounted on the stator, and a ring mounted on the conical rotor. This is illustrated in Figure 2.5. This high-pressure orifice has been considered on pump designs such as the Space Shuttle Alternate Turbopump Design (ATD) for the purposes of thrust balance, and was examined previously (Sivo *et al.* , 1994a).

A lucite ring which overlapped the base of the impeller (either by 1.02 *cm* or 1.08 *cm*) was used to form the rotating part of the orifice. The stationary housing was fitted with an existing aluminum ring which formed the non-rotating part of the orifice. The outer radius of the lucite rings and the inner radius of the aluminum ring produced a radial clearance of .0508 *cm*. For these experiments, the leakage path clearance was set to H =.254 *cm*.

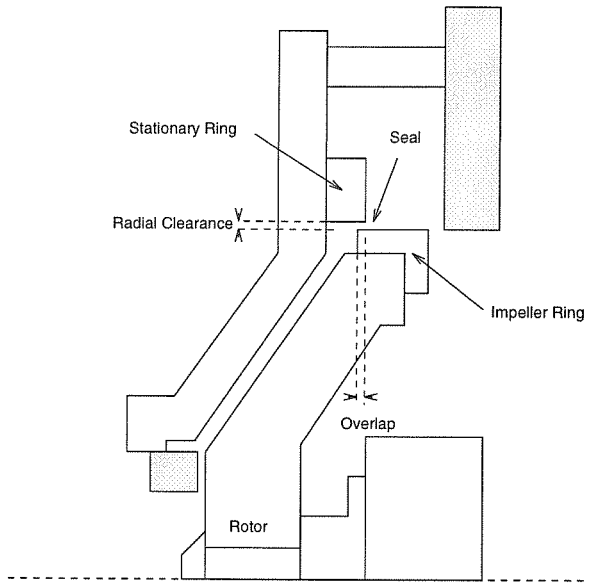

Figure 2.5: Experimental Configuration: Conic path with radial clearance high-pressure orifice seal.

The effect of axial overlap was studied with the high pressure orifice. A non-overlapping orifice with .0254 *cm* of axial clearance, an axially overlapping orifice of .038 *cm*, and an orifice with no axial overlap but no axial clearance were tested, along with the case in which no orifice was present, which was accomplished by removal of the stationary aluminum ring.

2.4 Inlet Guide Vanes

The effect of inlet swirl was investigated by installing a swirl vane at the leakage inlet to introduce pre-rotation in the direction of shaft rotation. In this study of leakage paths, inlet refers to the beginning of the leakage annulus, which corresponds to the discharge of a typical centrifugal pump and should not be confused with the pump inlet at the suction side. Figure 2.6 shows a typical vane consisting of a logarithmic spiral channel with a turning angle of 6 degrees, and its installation relative to the rotor and stator. The inlet swirl ratio, Λ (the ratio of the leakage flow circumferential velocity to the impeller tip velocity) is varied by changing the leakage flow rate and

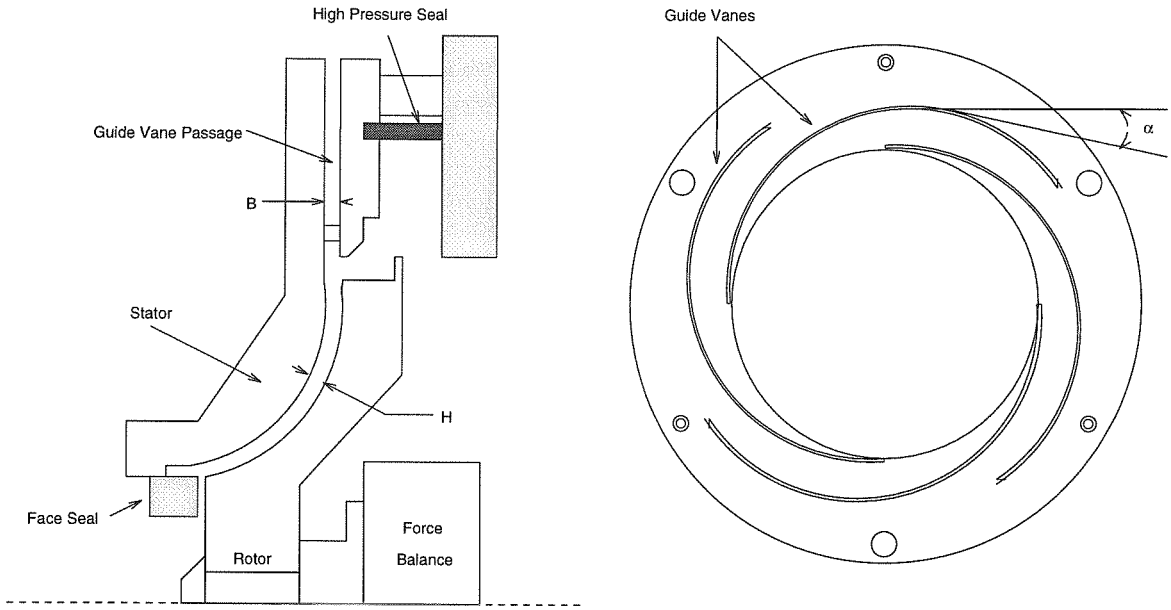

Figure 2.6: Inlet guide vane, 6 degree turning angle

the turning angle. The swirl ratio depends on the flow coefficient and turning angle according to:

$$\frac{\Lambda}{\phi} = \frac{H}{B \tan \alpha} \tag{2.1}$$

where $B = 0.318\ cm$ is the depth of the logarithmic spiral channel. A derivation of equation 2.1 (which assumes all leakage flow is constrained along the vane) can be found in Guinzburg (1993). For the present tests, two vanes with turning angles of 1^o, and 6^o were constructed to allow variation of α or ϕ while maintaining the same Λ. An existing 2^o swirl vane was also used. To investigate the effects of the added structure around the impeller, a turning vane with radial channels was also made to investigate the case of no swirl.

Typical values for Λ were taken from Rocketdyne data, which appears in Appendix A.

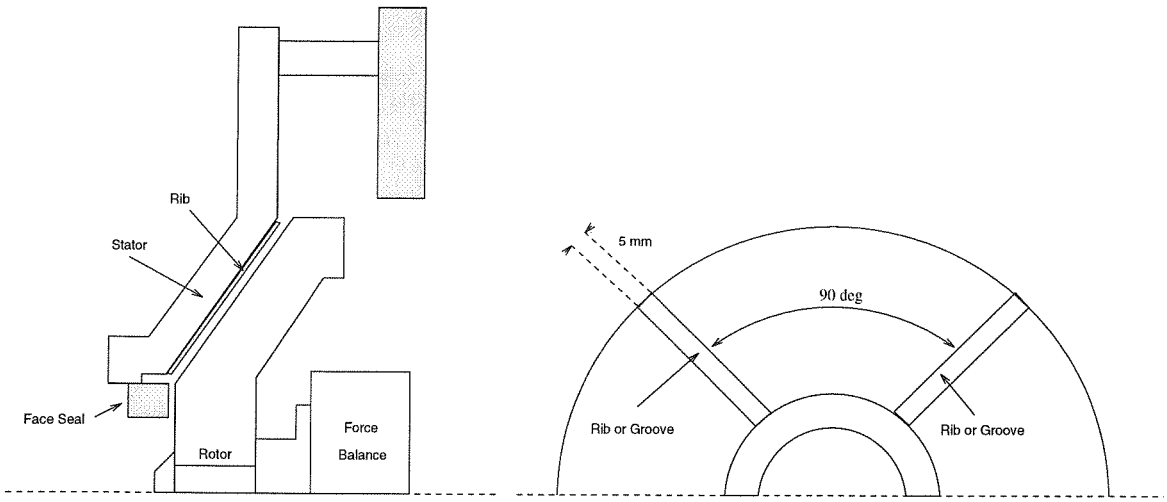

Figure 2.7: Anti swirl rib/groove locations.

2.5 Swirl Reduction Devices

The use of swirl reduction techniques has also been examined. Previous investigations (Sivo *et al.* , 1995) have demonstrated some benefit from fitting anti-swirl ribs to the surface of the stator, as this reduced the destabilizing forces. The inner surface of the conical stationary housing has been designed to accept meridional ribs or swirl brakes along the length of the leakage annulus. Four equally spaced ribs, .5 *cm* wide and .16 *cm* high were installed for the purpose of these tests. Results from Sivo demonstrated that more ribs did not produce significantly different results than tests with four ribs. Also, the effectiveness of ribs which did not extend the entire length of the leakage path were examined. For these tests, ribs along half the leakage path were mounted towards the tip and the eye of the stator.

The effectiveness of grooves machined into the stator surface has also been studied. For these tests, grooves which duplicated the height and width of the ribs were cut into the surface of the conical stator.

A diagram showing the anti-swirl ribs is presented in figure 2.7.

2.6 Experimental Method

The experiments were conducted with various main shaft speeds, although for any given comparison of geometries, the main shaft speed was held constant. A series of sub-synchronous whirl frequency tests were conducted. This involved changing the output of the frequency divider box to give a whirl frequency ratio of -.7 to +.7. At each whirl frequency, the phase of the main and whirl motors was checked using a strobe lamp. Between each run, the whirl motor was shut down and started up again to slowly reach the next whirl frequency ratio.

Data was obtained by using a data acquisition system connected to the strain gauge conditioning amplifiers. A clock signal from the frequency divider box was also sent to the data acquisition system ensuring accurate timing. The details of the software and hardware can be found in Franz (1989). Samples of 128 points per strain gage bridge per cycle were taken, and then averaged over 256 cycles, with each cycle being an integral number of revolutions of the whirl motor and hence the whirl motion. Data was then processed and reduced to a set of normalized normal and tangential forces for each whirl frequency ratio, using a normalizing force based on tip speed and axial length of the impeller, $\rho\pi\omega^2 R_2^2 L\varepsilon$. The internal force balance was calibrated using a system of pulleys, cables and weights which applied a static loads for any of the six force components. The details of the calibration procedure can be found elsewhere (Jery, 1986). The calibration is checked by running the dynamometer with mounted rotor and observing the steady force component in the vertical direction, which should equal the weight of the rotor.

Data were taken twice for each case, a "dry run" where the rotor was operated in air, with a water bearing protecting the seals of the eccentric drive, and a "wet run" in which the rotor was operated in a submerged state with the auxilliary pump generating a flow through the leakage passage. Data collected during a "dry run" was taken for each main shaft frequency at each whirl frequency for each of the rotors and any variation, including the additional rotating members added during the radial clearance low pressure seal and the high pressure orifice tests. This data, taken from

the rotor motion in air, was then subtracted from the "wet run" data to ensure proper isolation of the fluid forces. Buoyancy of the impeller was also calculated, using the force balance to measure both a dry weight of the impeller and a submerged weight. The vertically upward buoyancy force was then subtracted from the "wet run" data.

The leakage flow was provided by the auxilliary pumping unit, and throttled using the valves on the bypass loops. The flowrate was monitored using a Great Plains Industries digital flow meter mounted on the feed pipe of the auxilliary pumping unit, and manually recorded. The turbine flow meter and silent throttle valve of the main loop were not utilized. For tests with zero flow rate, the valves connecting the main loop to the auxilliary loop were shut. The normal and tangential forces resulting from a "wet run" are then fitted using a least squares curve fit to determine the rotordynamic force coefficient (See figure 3.1).

2.6.1 Experimental Error

The possibility of error in the measurements of the unsteady rotordynamic forces was considered carefully. Errors from hardware have been discussed previously (Jery, 1986) and the variance of force measurements with the current data acquisition system also examined (Franz, 1989).

The non-dimensionalization of the forces uses the normalizing force $\rho\pi\omega^2 R_2^2 L\varepsilon$. The largest uncertainty in this factor during the data processing is the eccentricity ε. The eccentricity has been verified many times with dial indicators for various static positions of the dummy impeller in both the rotational and whirl motions. However, a check of the displacement of the test article during a typical submerged test was considered advisable to verify the rotor motion. It was also used to confirm the rotational and whirl frequencies.

Bently displacement transducers were provided by Rocketdyne to measure the motion of the contoured impeller during a typical submerged test. Figure 2.8 shows the location of the transducers in the test section. A special rotating member was added to the contoured impeller to increase the surface area for the transducer measurement.

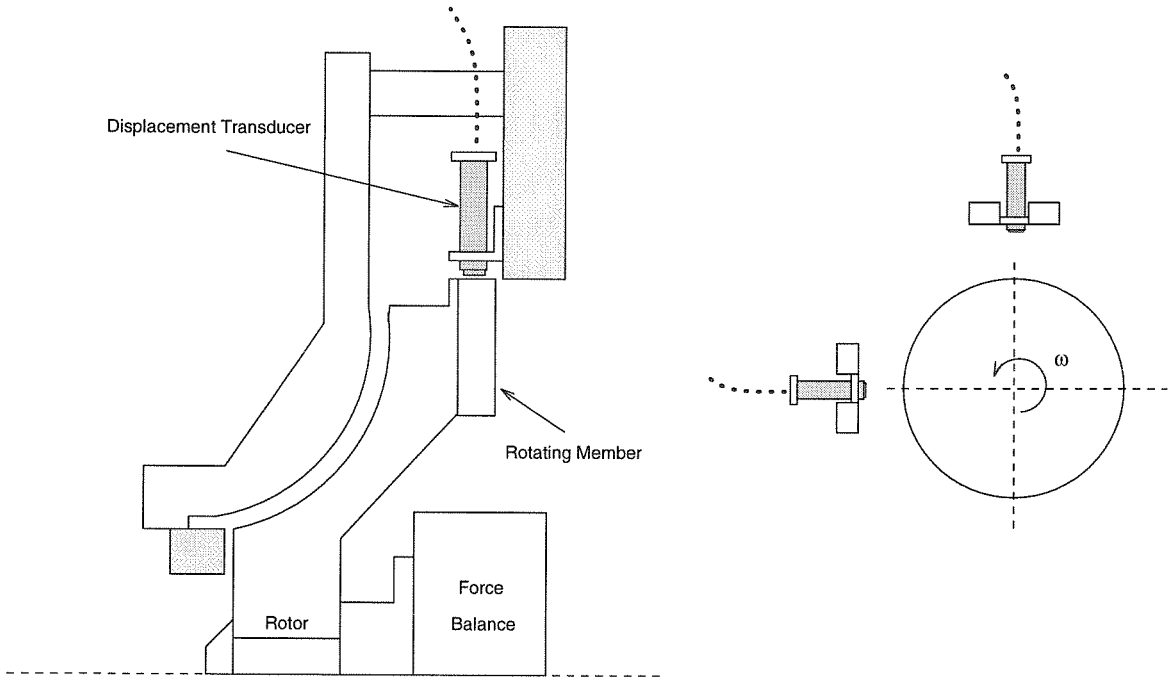

Figure 2.8: Bently displacement transducer locations.

The transducer output confirmed article out of roundness and eccentricity, and both were found to be similar to static measurements with the dial gauge under all flow conditions. Both the dial gauge and the displacement transducers confirmed a deviation from the nominal value of the eccentricity (0.0254 cm) of 0.00127 cm, or 5%. The whirl frequency ratio was also verified from the plots of the displacement.

Figure 2.9 shows sample plots of the displacement versus time for the contoured shroud at 1000 rpm with various whirl frequency ratios. The whirl motion can be seen as the main component of the waveforms. However, a smaller component at the main shaft frequency is also superposed, and is caused by the machining tolerances of the test impeller. It was concluded that the potential error in the normalized forces due to the uncertainty in the eccentricity is $\pm$ 5%.

An examination of the potential errors in the force measurements rather than the eccentricity was also conducted. Here it is postulated that the largest source of uncertainty is probably from the bridge/amplifier electronics, with temperature drift from the time of the last rebalancing of the strain gauge amplifier circuits being the

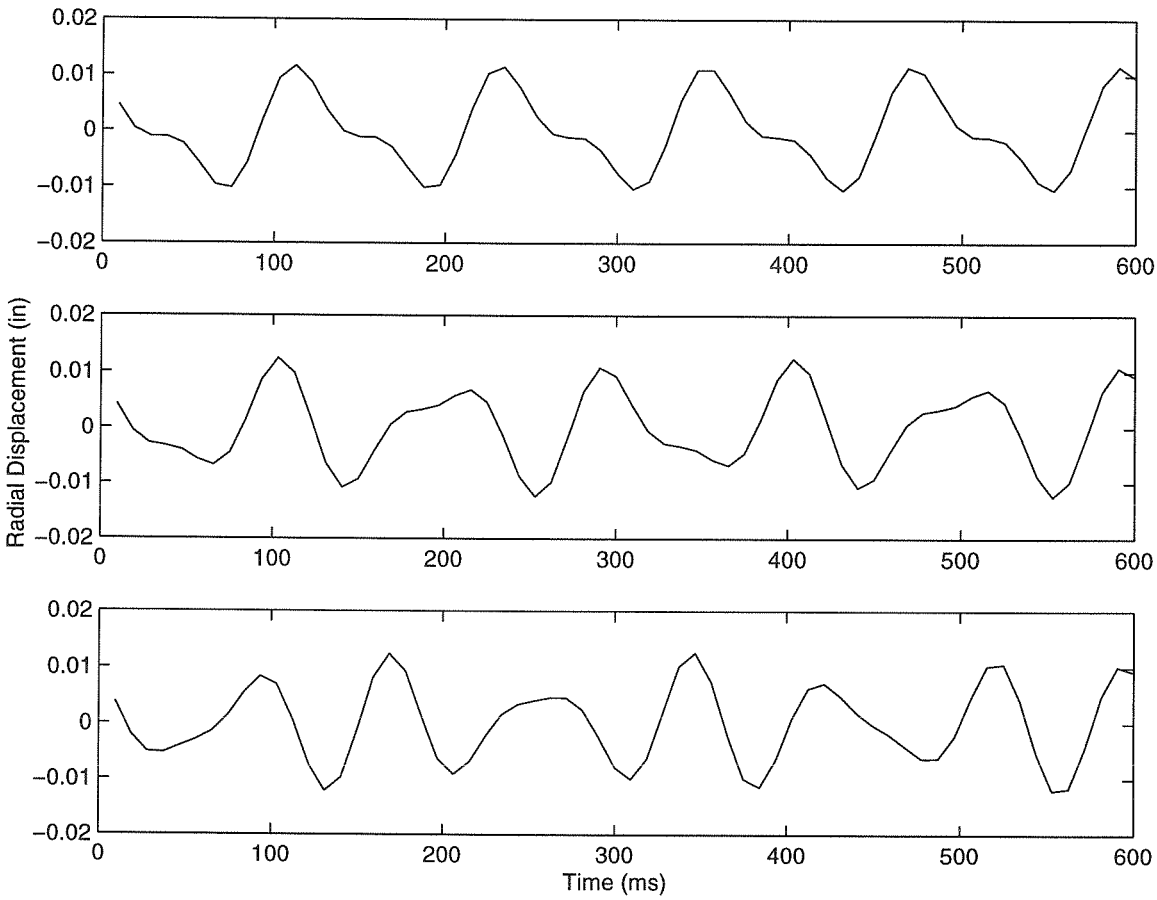

Figure 2.9: Plot of radial displacement versus time for Bently transducers and contoured rotor. $\Omega/\omega = .5$ (top), .6 (middle), and .7 (bottom).

greatest contributor.

A nominal set of tests with the zero swirl vane (straight guides) at 1000 *rpm* and a .77 *l/s* flow rate (relatively high) was conducted, with no re-zeroing of the strain gauge amplifiers during 3 hours of continuous operation. The set of whirl frequencies, $-0.7 < \Omega/\omega < 0.7$ was swept three times during this period, and the forces and the resulting force coefficients from the least squares fit were examined. Flow rate uncertainty for this test is less than 1%.

The unsteady normal and tangential force for this set of experiments are presented in figure 2.10. The "reported data" were taken on a seperate occasion. The other tests are listed in order as they were taken during the 3 hour operation. Examining the measurements for the normal force, reassuring repeatability and consistency is observed. The "dip" in the normal force at $\Omega/\omega = .2$ is duplicated in every case. There is slightly more scatter in the plot of the tangential force, but again, larger deviations such as at $\Omega/\omega = .1$ are repeated in every case.

For each of the tests, to determine the uncertainty in the rotordynamic coefficients (see section 1.2), a least squares fit of the data was performed. The coefficients were then averaged to find a mean value, and a standard deviation from this mean value was calculated for all the sets of data. This deviation as a percentage of the mean value is used as a measure of uncertainty for each of the rotordynamic force coefficients. The uncertainty associated with each rotordynamic coefficient was:

$M = 4.3\ \%$

$c = 1.3\ \%$

$K = 8.0\ \%$

$C = 5.4\ \%$

$k = 5.1\ \%$

$k/C = 5.0\ \%$

The rotordynamic coefficients of the normal force seemed to have the largest and smallest percentage error.

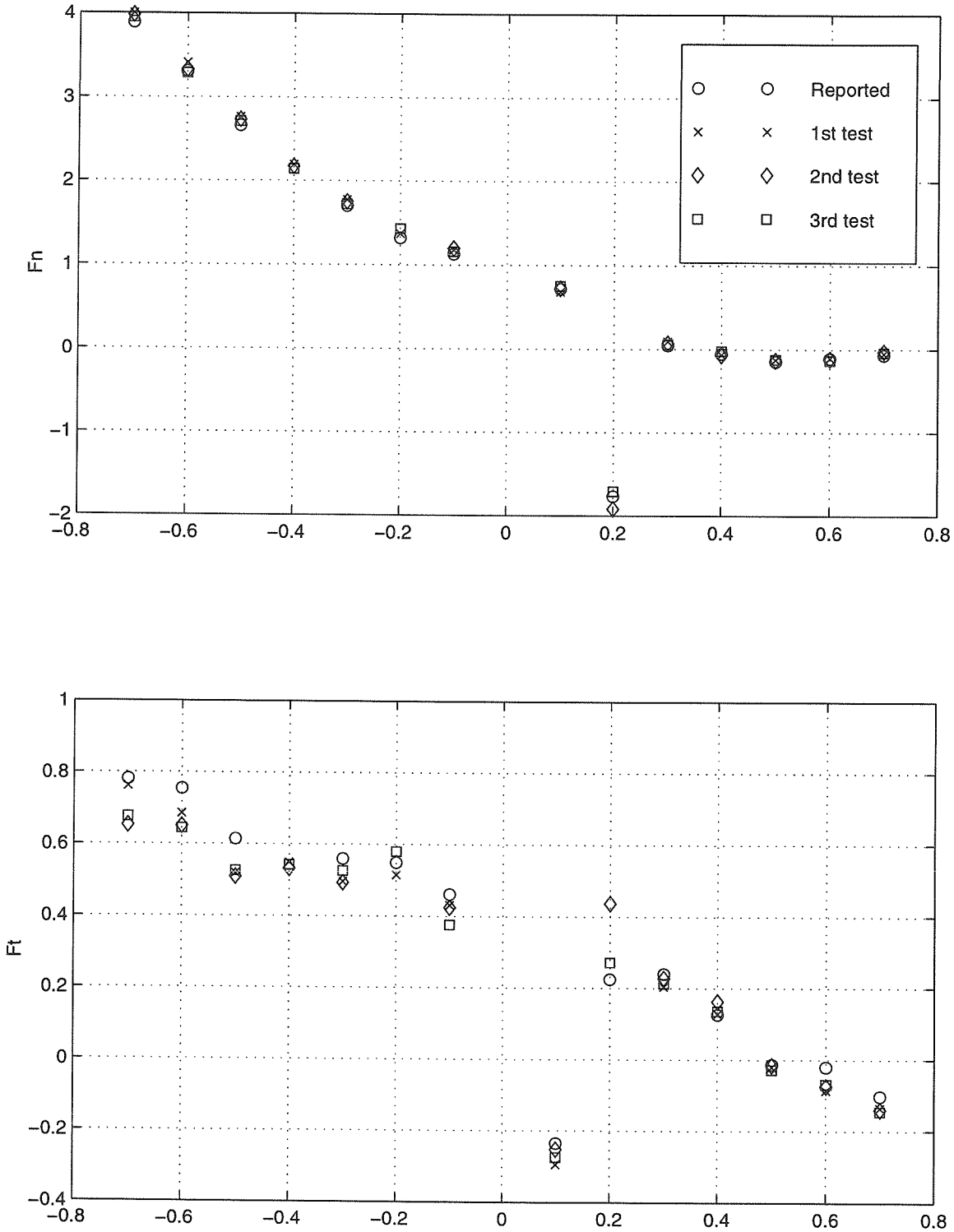

Figure 2.10: Unsteady rotordynamic forces plotted as functions of the whirl frequency ratio, Ω/ω. Reported data taken seperately, 1st test completed within 1hr, 2nd test completed after 2hrs, 3rd test completed after 3 hrs of operation.

Chapter 3 Experimental Results

3.1 Introduction

A number of the effects of leakage path geometry have been investigated previously. The functional dependence of the rotordynamic forces on whirl frequency ratio was similar for the dummy impeller and actual impellers. The effect of eccentricity was insignificant when using the normalizing force, $\rho\pi\omega^2 R_2^2 L\varepsilon$, indicating that previous tests lie within the linear response regime. Shaft speeds of 500 to 2000 *rpm* were tested and the forces were shown to be independent of the shaft speed. With the conical impeller, a region of forward whirl for which the tangential force is destabilizing is found to decrease with increasing flow rate. Increasing the flow rate also increased the magnitude of the normal force. The dimensionless rotordynamic forces are roughly inversely proportional to the clearance. The effect of inlet swirl was to increase the tangential force and hence be destablizing. The inlet swirl also caused a decrease in the normal force at positive whirl ratios, leading to larger cross-coupled damping. Anti-swirl devices in the leakage path were found to offer some decrease in the whirl ratio of the tangential force for low flow coefficients. The reader is referred to Guinzburg (1992-1994) and Sivo (1994-1995) for details of the described effects.

The following effects are detailed in Bolleter (1989). The effect of a wear ring seal compared with a face seal for impellers was studied. The wear ring seal results in a larger (in some cases positive) direct stiffness which corresponds to a stable normal force. The cross-coupled stiffness and direct damping are also larger for the wear ring compared with the face seal, while the direct damping is similar, resulting in a much larger tangential force. When the contributions to the unsteady forces of the seal were tested independently, it was found that these three rotordynamic force coefficients were dominated by the seal. The added mass and cross-coupled damping were dominated by the impeller shroud.

3.2 Forces and Curve Fitting

Rotordynamic force coefficients provide a convenient means of reducing force data for ease of comparison. From the previous investigations discussed in the introduction, fluid parameters such as the leakage flow rate and inlet swirl appear to have significant effects on the forces, and so it seems appropriate to examine the force coefficients as functions of these parameters. The validity of the second order curve fit for the normal force and the first order curve fit for the tangential force is a subject of concern. Figure 3.1 shows a typical plot of the rotordynamic forces versus the whirl frequency ratio for the conical leakage path. As can be seen from the curve fit, the quadratic fit to the normal force is accurate for the experimental data presented, however, it seems that the curvature and hence the coefficients M and c may change depending on the number of experimental data points taken beyond the whirl frequency ratio $\Omega/\omega =$ .7. As all tests presented do not include data beyond this whirl frequency ratio, the coefficients of the normal force should be consistent. The linear fit to the tangential force also appears appropriate for the data collected, but there are points, particularly the value of F_t at $\Omega/\omega = .1$, that are not modeled well by this straight line.

Figure 3.2 shows the rotordynamic forces as functions of the whirl frequency ratio for the tests with swirl vanes on the contoured leakage path. For the tests with inlet swirl, $\Lambda = .5$, a quadratic curve fit appears appropriate with little loss in accuracy. The tangential force for the case with swirl is more complex; however a linear fit would seem to provide a reasonable approximation to the force. With no inlet swirl, the high flow rate case, $\phi = .055$ appears to be problematic. A "dip" in normal force at $\Omega/\omega = .2$ would adversely affect a least squares curve fit. Similar phenomena in the tangential force at $\Omega/\omega =$ -.4 and .1 would also lead to a poor curve fit. For a majority of the data collected however, the phenomena seen in this particular case are absent and the curve fitting seems to be a reasonable method of obtaining force coefficients for comparison. It is interesting to note the trends of the forces with flow rate in figure 3.2, which are similar to those in previous studies.

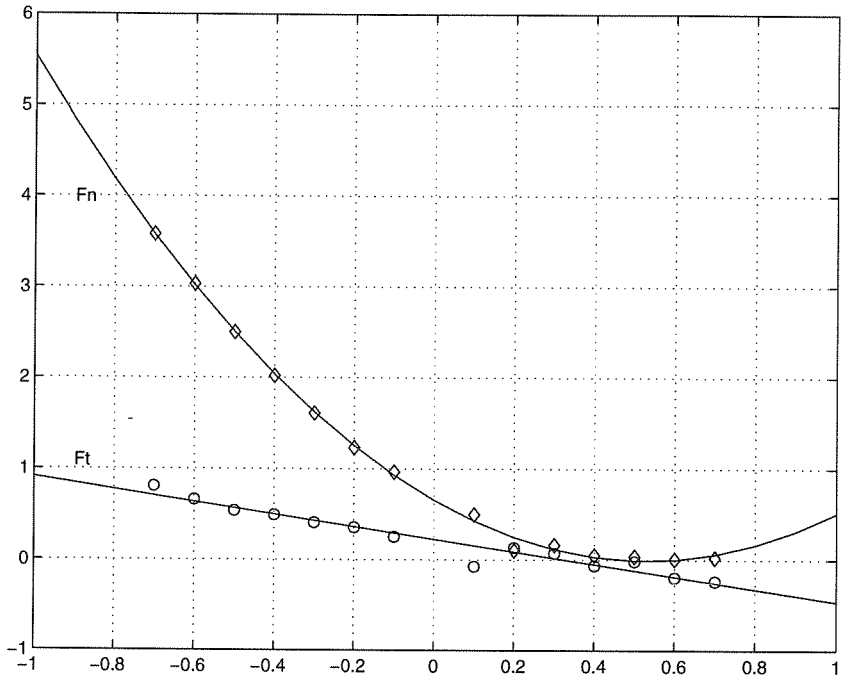

Figure 3.1: Experimental rotordynamic forces plotted versus whirl frequency ratio Ω/ω, including resulting curve fits.

3.3 Comparison of Leakage Path Geometries

Variations in leakage path geometry were examined using the various dummy impellers and stators described in the previous chapter. The conical stator and rotor with its 45 degree leakage path was tested and compared to the contoured rotor and stator which matched in eye diameter, tip diameter, axial length, and leakage path clearance. A rotor and stator with a large eye diameter and short axial length, which modeled the geometry of the Space Shuttle Main Engine High Pressure Oxidizer Turbopump (HPOTP), was also examined.

For this comparison, a constant main shaft speed, ω, of 1000 *rpm* was used. The range of flow coefficients from 0 to .033 were studied using various flow rates. A constant leakage path clearance of $H = .30$ *cm* was also used. The rotordynamic force coefficients were derived from a least squares quadratic and linear fit of the normal and tangential forces respectively, F_n and F_t, which were measured over the range of

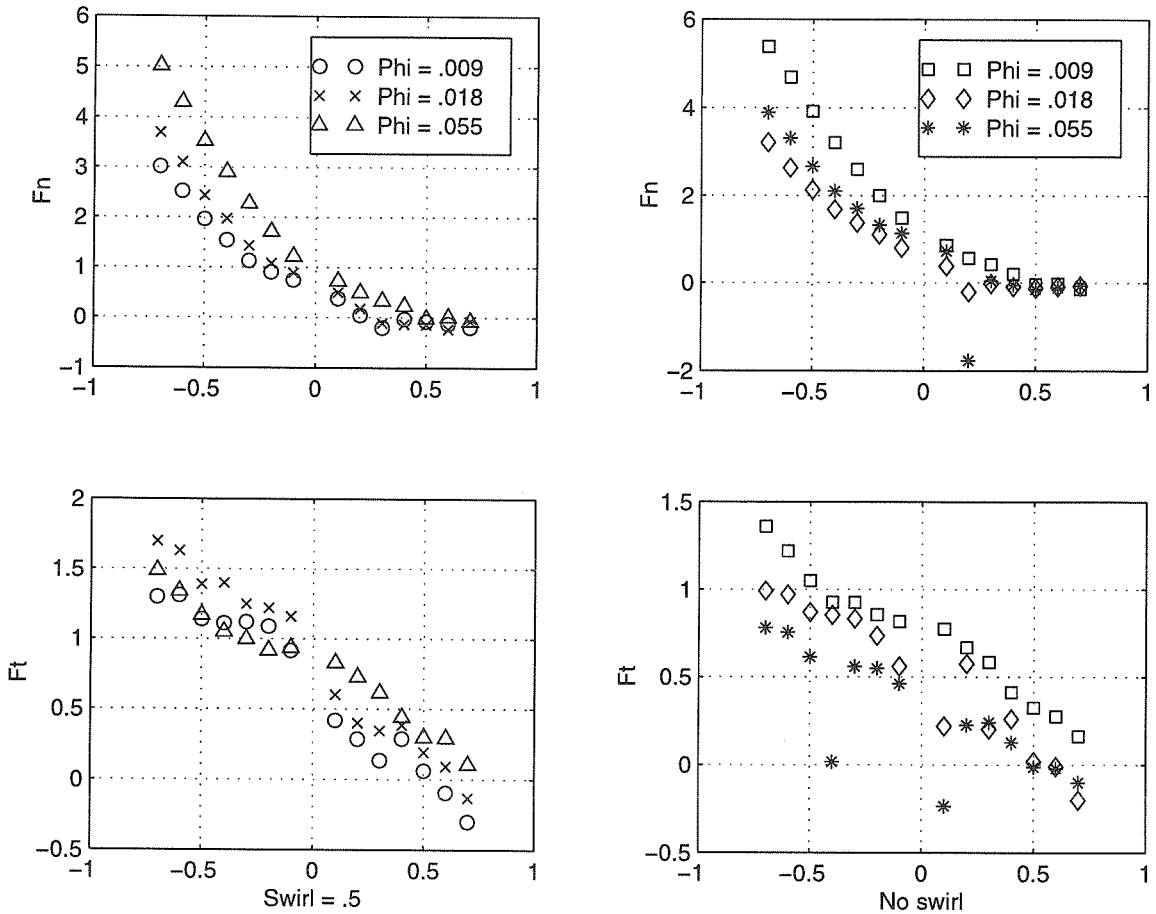

Figure 3.2: Experimental rotordynamic forces plotted versus whirl frequency ratio Ω/ω, with inlet swirl, $\Lambda = .5$ (left) and without inlet swirl (right).

whirl frequency ratios, $-0.7 < \Omega/\omega < 0.7$. Figure 3.3 presents the dimensionless rotordynamic force coefficients as functions of the leakage flow coefficient, and compares the conical and contoured leakage path geometries.

Except for the cross-coupled stiffness, all of the rotordynamic force coefficients match in both trend and magnitude for the contoured and conic dummy impellers, showing that the effect of the geometry of the passage is relatively small provided that parameters such as the eye/tip diameter and axial length are the same. The effect of having a shorter path (which alters the non-dimensionalization due to the axial length) with a larger eye/tip diameter ratio, is also fairly pronounced when comparing

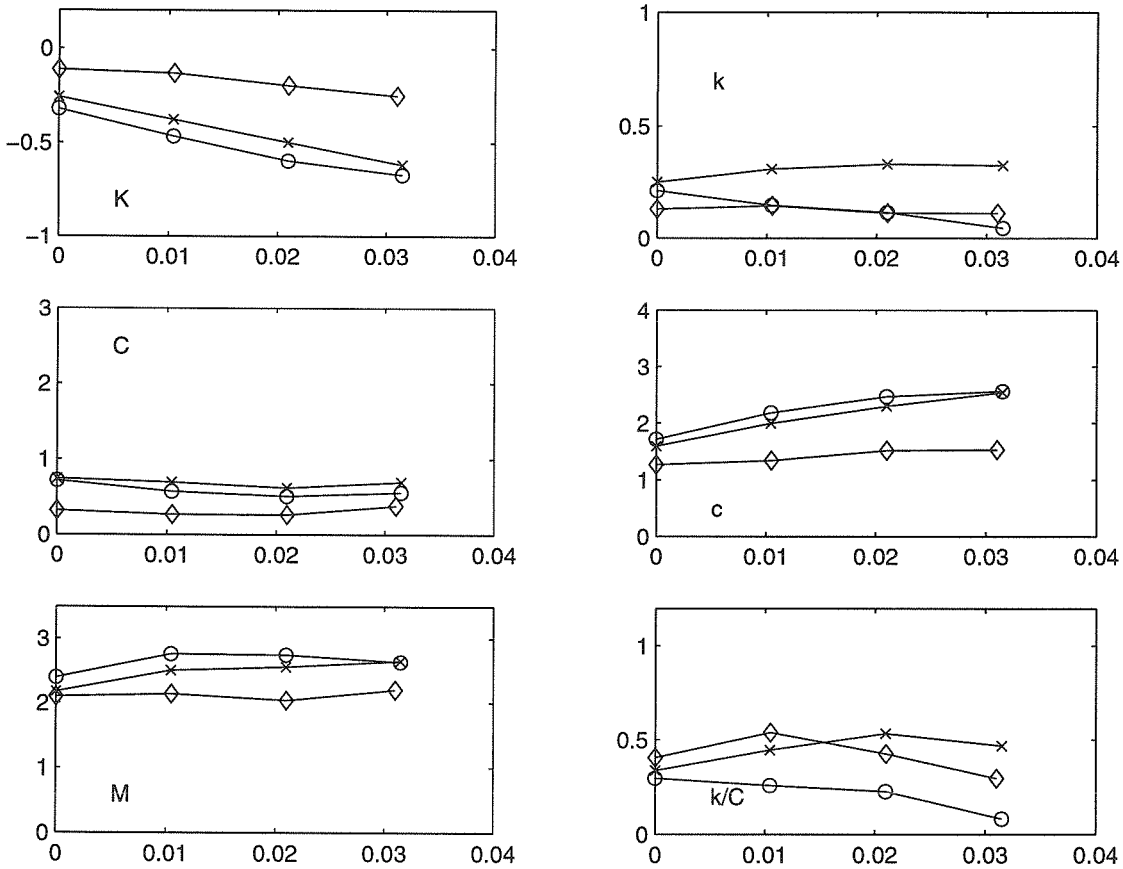

Figure 3.3: Experimental rotordynamic coefficients versus flow coefficient ϕ for the conic ($\circ$), contoured ($\times$), and short contoured ($\diamond$) leakage paths.

all three geometries. The forces for this short rotor are much smaller in magnitude. The coefficients K, c, M, are virtually identical for the conic and contoured geometries, reflecting the fact that the path shape has little effect on the normal force, F_n. The short contoured geometry normal force coefficents follow the same trends as the other two leakage paths, but are smaller in magnitude across the entire range of flow coefficients.

The contoured rotor has a larger cross-coupled stiffness, k, than the conic rotor over the entire whirl frequency range. The cross-coupled stiffness for the short dummy impeller follows the same trend as the contoured impeller, but at a smaller magnitude. The direct damping C, seems to be fairly uniform for all three rotors, with the short

rotor showing a slightly smaller magnitude. The change in k produces a corresponding change in the whirl ratio, k/C. Earlier, it was reported by Guinzburg (1992) and Sivo (1995), that, with the conical geometry, the whirl ratio decreased with increasing flow coefficient, and this is confirmed with the present experiments with the conical geometry. However, the contoured geometry produces a k/C which increases with increasing flow coefficient. This trend may reverse at higher flow coefficients, as suggested by the fact that the short geometry shows a decreasing trend for the whirl ratio k/C. Indeed, in the tests with inlet swirl described later, the contoured path was subjected to much larger flow rates and the whirl ratio decreased at larger values of ϕ than are shown here.

3.4 Seals

A change in the low pressure seal of the leakage path constitutes a substantial change in path geometry, and the effects of the different seal geometries are significant. This is possibly due to the change in pressure gradient along the leakage path. Figure 3.4 presents the dimensionless rotordynamic force coefficients obtained from the low pressure seal experiments as functions of the leakage flow coefficient.

The wear ring seal (radial clearance) has a larger magnitude tangential force over the range of flow coefficients examined in comparison to the face seal (axial clearance) geometry. For the radial clearance seal, the cross-coupled stiffness, k, and direct damping, C, increase with increasing flow coefficient while for the axial clearance seal, the coefficients of the tangential force remain relatively constant. Despite the larger tangential forces in the radial clearance seal, the effect on the whirl ratio, k/C is small since both k and C seem to increase by equal amounts.

The direct added mass and cross-coupled damping are approximately the same for both seals, but the direct stiffness K increases with increasing flow coefficient for the radial clearance seal. This leads to a normal force which becomes more stabilizing as the flow rate is increased, and this is quite different from all previous Caltech investigations which used the axial clearance seal. The data does however appear

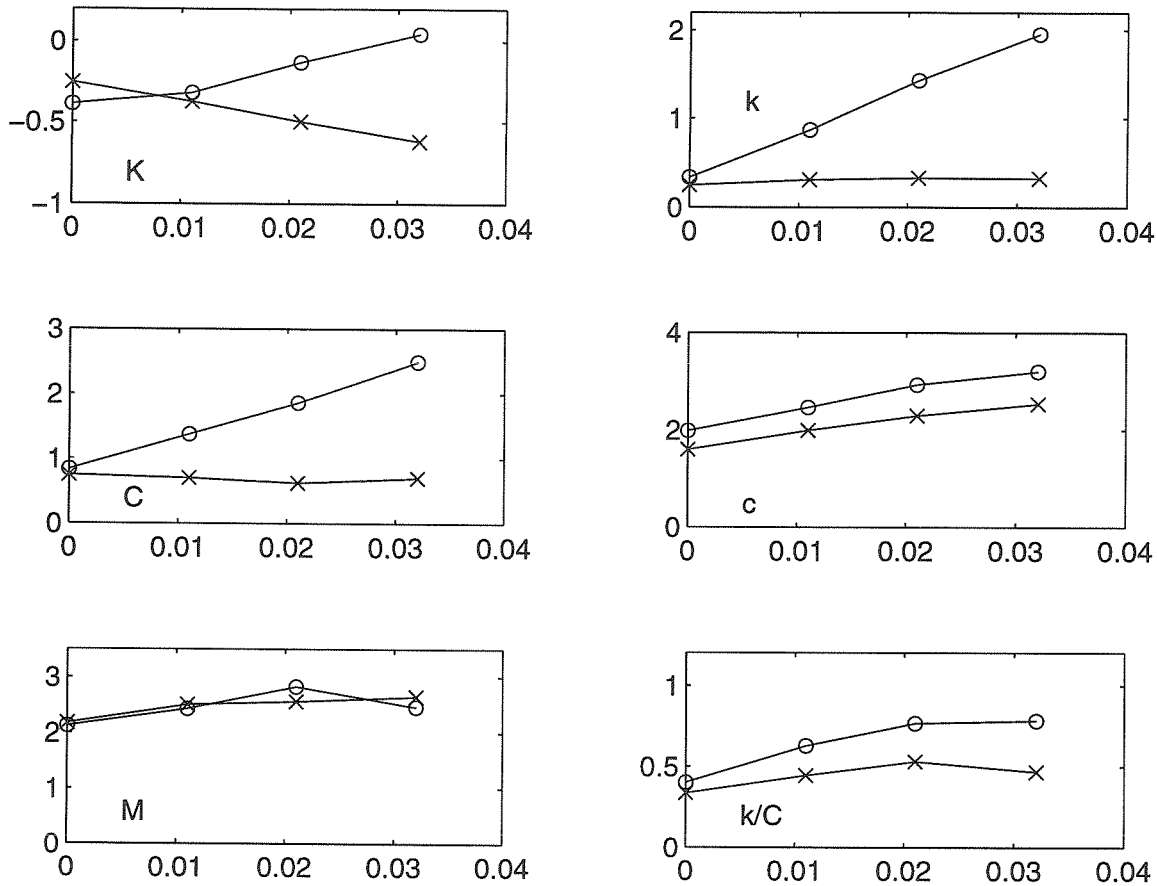

Figure 3.4: Experimental rotordynamic coefficients plotted against flow coefficient ϕ for radial (o) clearance and axial ($\times$) clearance low pressure seal.

similar to results reported by Bolleter for a wear ring seal and face seal comparison (1989).

The results for the high pressure seal are shown in figure 3.5. It appears as though the orifice seal geometry on the high pressure side, whether overlapped, non-overlapped, or retracted, has no effect on the forces. However, all three configurations of the high pressure orifice cause increases in both the tangential and normal forces acting on the impeller when compared to the case in which no orifice is present. The values of C and k are increased in the presence of the orifice, leading to higher magnitudes of the tangential force. The whirl ratio, k/C, is also increased due to the orifice, and the decreasing trend with increasing flow coefficient is once again

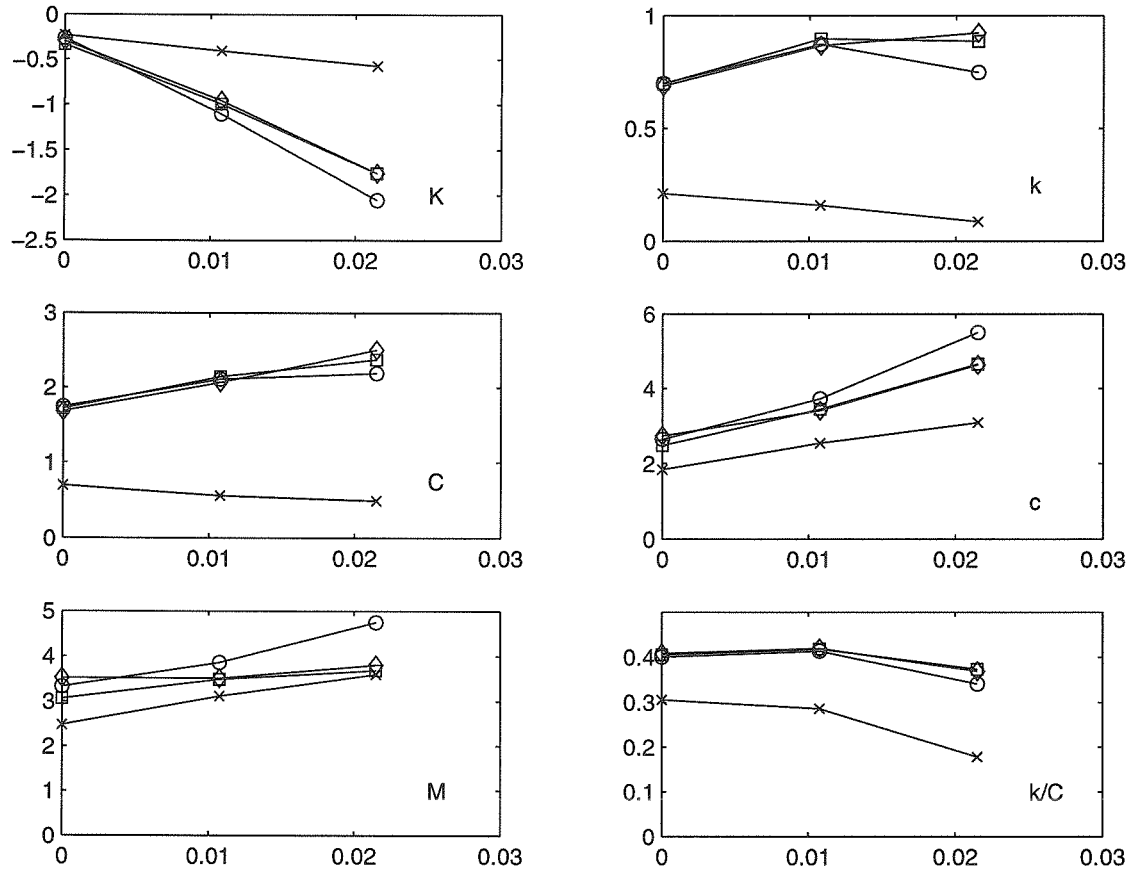

Figure 3.5: Experimental rotordynamic coefficients versus flow coefficient ϕ for the high pressure orifice, conical geometry. Overlapping ($\circ$), neutral ($\diamond$), retracted ($\square$), and no ($\times$) orifice seal.

observed.

The effect on the direct stiffness of the high pressure orifice is opposite of that observed in the radial clearance seal. As the flow increases, the direct stiffness decreases leading to greater destabilizing effects in the normal force. Again, the seal configuration does not appear to greatly affect the added mass and cross-coupled damping.

3.5 Effects of Inlet Swirl

Using relation 2.1, a set of experiments was designed to determine the effect of inlet swirl on the unsteady rotordynamic forces in the contoured leakage path. The three swirl vanes of different turning angles were employed to alter the inlet swirl ratio, and a swirl vane with perpendicular channels was used to generate the data for zero inlet swirl. Figure 3.6 shows plots of the dimensionless rotordynamic force coefficients obtained from the swirl experiments as functions of the leakage flow coefficient. It appears as though the amount of inlet swirl, Λ, has little effect on the forces for any flow rate. However, the effect of swirl is destabilizing compared to the case with no swirl, as previously observed by Guinzburg (1992).

The force coefficients for the tangential force are larger when swirl is present compared to the case with no swirl. For the tests with swirl the cross-coupled stiffness appears to remain at an almost constant level for various values of Λ, while the direct damping shows a tendency to first increase and then decrease slightly with increasing flow coefficient. This leads to a whirl ratio, k/C, that increases with increasing flow coefficient and so the tangential force does not exhibit a substantial reduction as the flow coefficient increases. In the case with no swirl, however, a reduction of the whirl ratio is observed for the contoured dummy impeller at higher flow rates.

Upon examination of the coefficients which determine the normal force, the same trends for M, c, and K observed for the conical rotor by Guinzburg and Sivo are also seen in the present experiments. The added mass does not exhibit an appreciable difference in the cases with and without swirl, but the direct stiffness is higher and the cross-coupled damping is smaller with no inlet swirl. In summary, the fluid circumferential velocity affects the rotordynamic behavior significantly if it is nonzero, but the amount of pre-rotation has little influence on the rotordynamics.

The effect of swirl on the leakage path geometry was also considered. Some differences are noted, which presumably arise from the difference in the contoured and conic shape of the path. Figure 3.7 shows the rotordynamic force coefficients for both leakage paths. The coefficients of the normal force appear to be similar, but there are

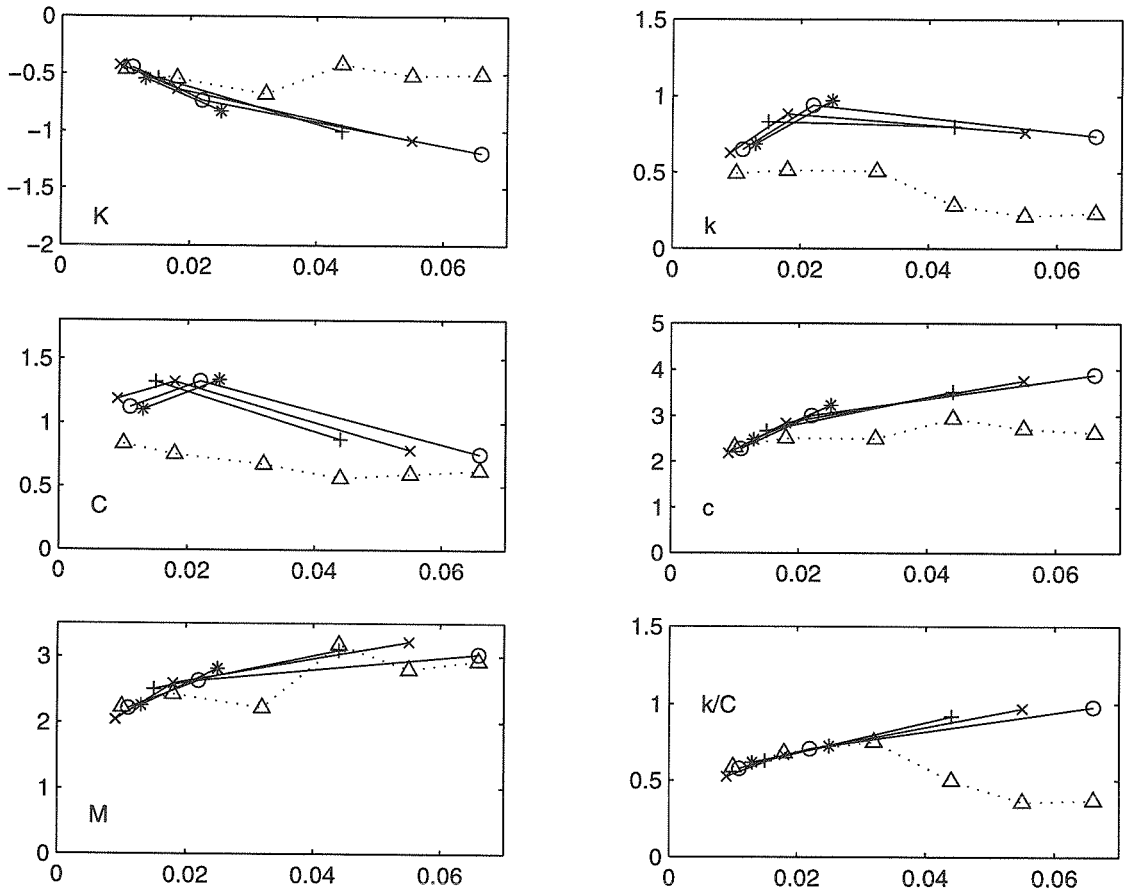

Figure 3.6: Experimental rotordynamic coefficients plotted against flow coefficient ϕ for tests with inlet swirl, $\Lambda = 0.0$ ($\triangle$), 0.4 (+), 0.5 ($\times$), 0.6 ($\circ$), and 0.7 ($*$).

significant differences in the trend and magnitude of the cross-coupled stiffness and direct damping, leading to a differences in the whirl ratio where the contoured rotor shows an increasing trend with flow rate, while the conic rotor indicates a decreasing trend.

3.6 Effects of Anti-Swirl Devices

Of course, fluid swirl is generated in the leakage passage and the question arises as to whether modification of that motion would alter the destabilizing rotordynamic

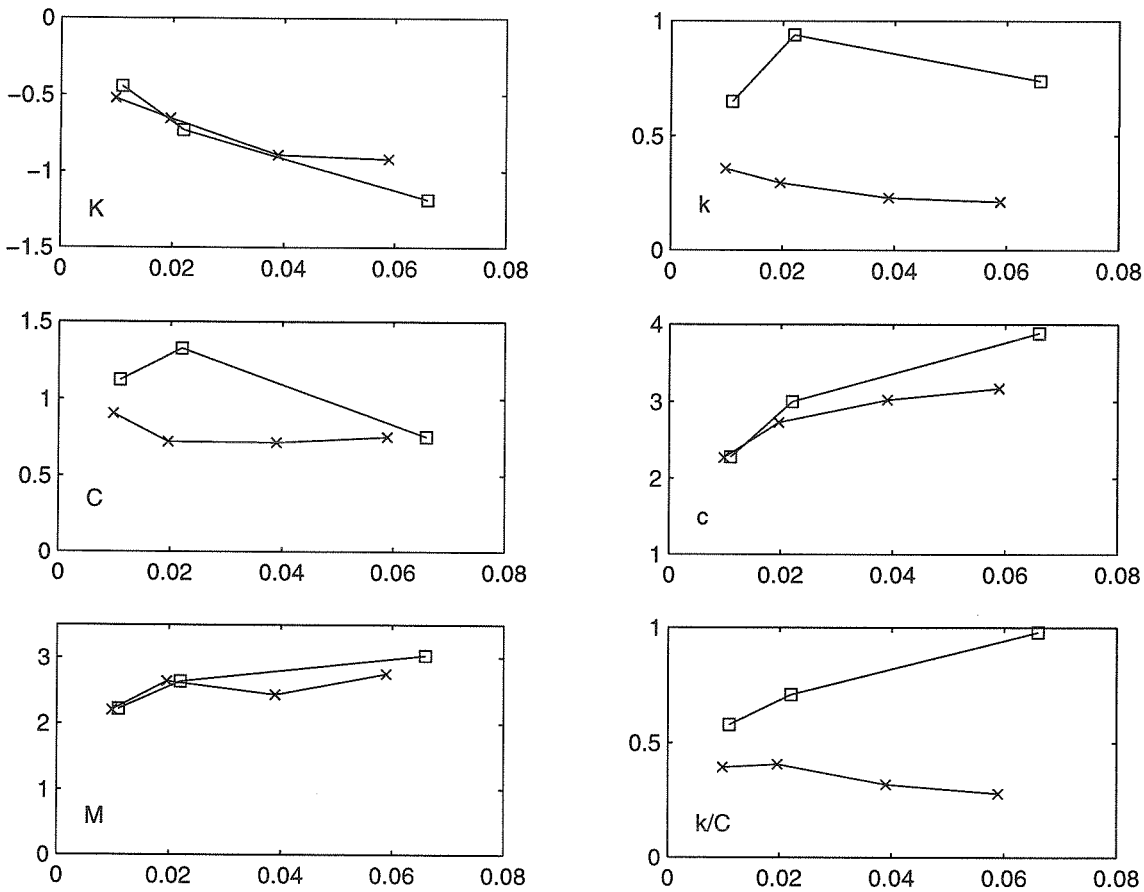

Figure 3.7: Experimental rotordynamic coefficients plotted against flow coefficient ϕ for tests with inlet swirl, for the contoured path ($\square, \Lambda = .6$), and for the conical path ($\times$).

forces. Thus, the effect of anti-swirl ribs and grooves installed in the leakage path is considered. Work by Sivo (1995) identified some benefit to having anti-swirl measures in the leakage path, but only for very small flow coefficients.

Figure 3.8 shows plots of the dimensionless rotordynamic force coefficients obtained from the anti-swirl rib experiments as functions of the leakage flow coefficient for the conical path. These experiments are similar to those of Sivo (1995), who studied various numbers of anti-swirl ribs in the conical leakage path, and demonstrated that the number of ribs did not contribute significantly to the rotordynamic forces due to the leakage flow. The effect of positioning four anti-swirl ribs is shown, for

ribs which run the entire length of the leakage path, and for ribs which run half the length of the leakage path, positioned towards the tip of the impeller and the eye of the dummy impeller.

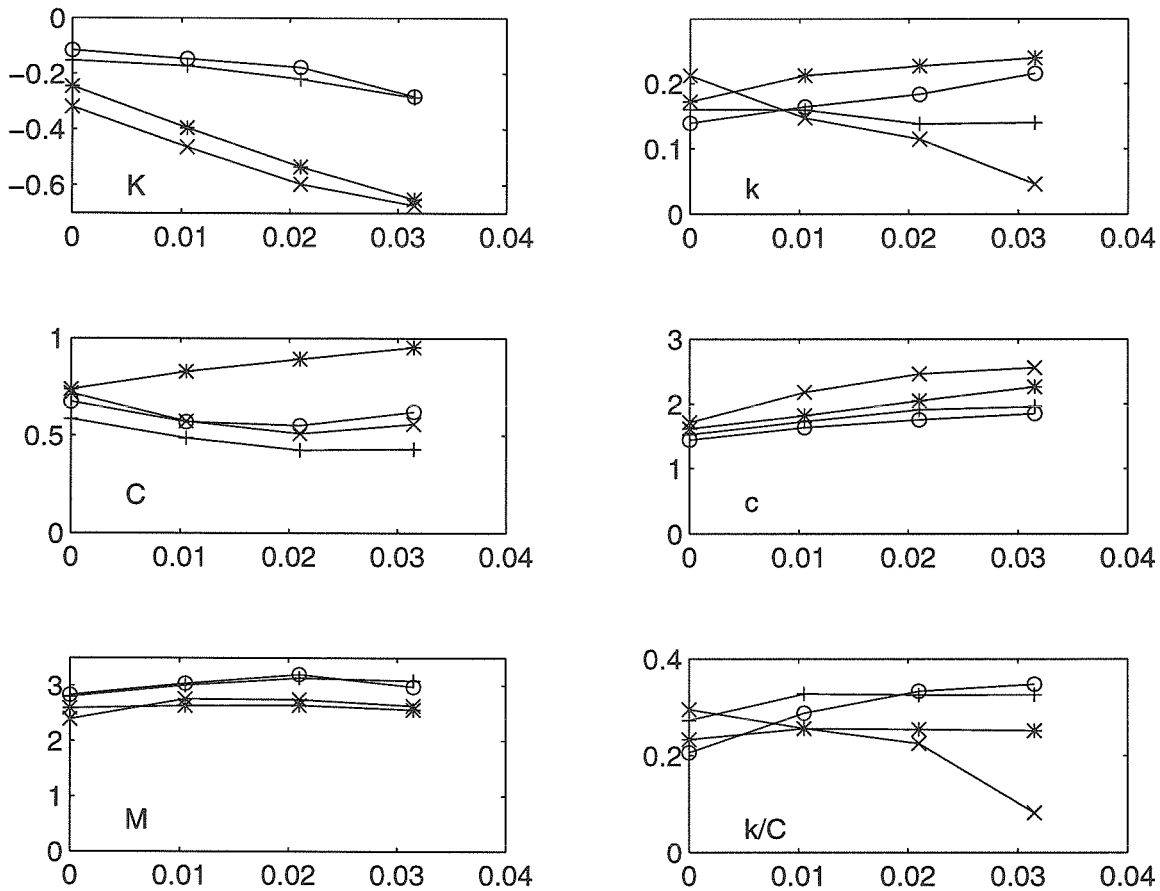

Figure 3.8: Rotordynamic coefficients plotted against the flow coefficient ϕ for the experimental tests with no anti-swirl devices (x), 4 anti-swirl ribs full length (o), half-length at the tip (+), and half-length at the eye (*).

The direct damping appears to be similar for the case with no ribs, full length ribs, and half-length ribs at the tip. The direct damping is altered by the presence of the half-length ribs at the eye. All ribs seem to affect the cross-coupled stiffness in a similar manner, offering a slight reduction at small flow rates over the case with no devices at all. This leads to a whirl ratio which reflects the same behavior observed by Sivo, a slight benefit at small flow coefficients. The eye ribs have a smaller whirl

ratio at higher flow rates compared to the full length and tip ribs.

The added mass and cross-coupled damping are not noticeably affected by the devices, however an increase is observed in the direct stiffness for the ribs at the tip and the full length ribs. The reduction of swirl velocity close to the inlet has a beneficial effect on reducing the normal force.

Figure 3.9 shows the rotordynamic force coefficients as functions of flow coefficient for the conic shroud, comparing grooves and ribs as anti-swirl measures. This time, the tests are conducted with the 2^o swirl vane, so that there is some inlet pre-rotation of the fluid as it enters the leakage path.

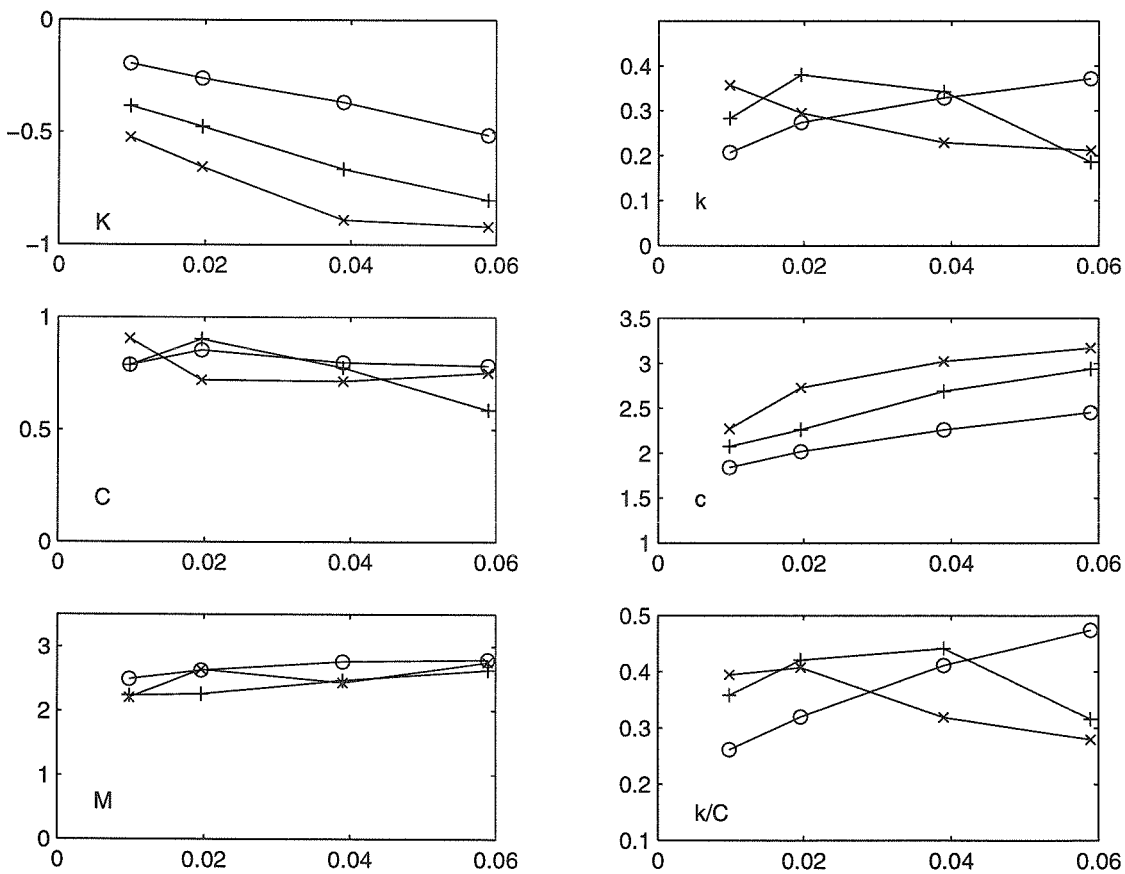

Figure 3.9: Rotordynamic coefficients plotted against the flow coefficient ϕ for the experimental tests with inlet swirl. No anti-swirl devices ($\times$), 4 full length anti-swirl ribs ($\circ$), 4 full length anti-swirl grooves ($+$).

The same clearance of $H = .3048\ cm$ is used through all the tests. The direct stiffness K is smallest and the cross-coupled damping c largest for the cases with no anti-swirl measures. These coefficients are improved for the case with grooves, and experience the greatest benefit in stability for the anti-swirl ribs. The direct added mass remains approximately the same for all three cases.

The direct damping of the tangential force shows roughly the same magnitude and constant trend with increasing flow coefficient for all three cases. This is different from the case with swirl on the contoured leakage path reported in the previous section, and may stem from the geometrical differences. The cross-coupled stiffness k, decreases for no anti-swirl devices, and increases with increasing flow coefficient for the case with ribs. With grooves, the cross-coupled stiffness first increases and then decreases with flow coefficient. This leads to a whirl ratio k/C which shows some improvement for anti-swirl devices at very low flow rates, and then a detrimental effect as the flow rates increase. The anti-swirl grooves decrease the whirl ratio at higher flow coefficients, and it is not clear if this trend will mean an improvement over no devices at flow rates higher than those tested. The whirl ratio, in the presence of swirl, shows a decreasing trend for the conical impeller, which is similar to Guinzburg's and Sivo's results but different for the contoured impeller discussed previously.

It seems that all the anti-swirl devices give some benefit in reducing the destablizing region of the tangential force, but only for small flow rates. Anti-swirl devices have some effect on increasing the direct stiffness, aiding the stability of the normal force.

3.7 Comparison of Experimental Data

The data of Guinzburg and Sivo are examined for consistency with some of the current experimental results. These prior investigations used the conical geometry and a 2^o swirl vane for the cases with inlet swirl. While the clearances and eccentricities are widely varied, trends in the rotordynamic forces seem repeatable and consistent.

Figure 3.10 shows the rotordynamic force coefficients as functions of flow coefficient

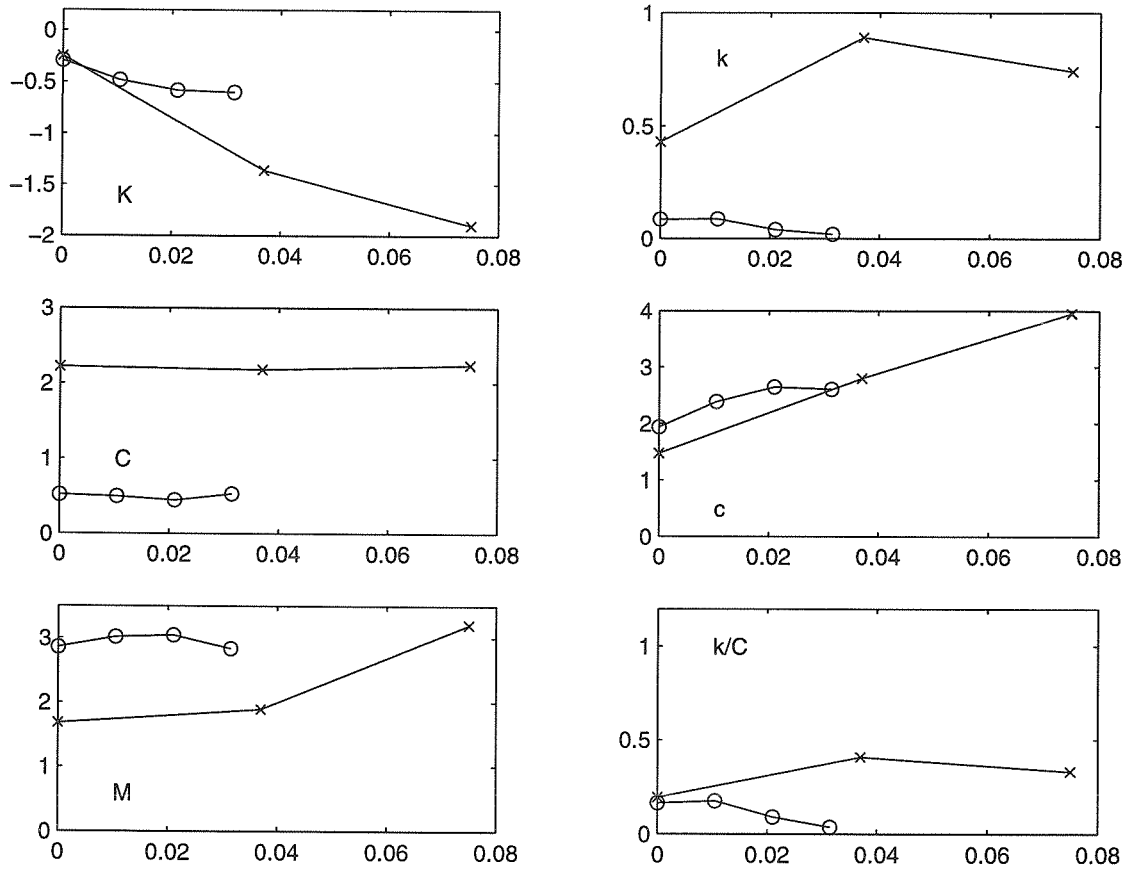

Figure 3.10: Rotordynamic coefficients versus flow coefficient, ϕ, for the case of a conical impeller at 2000 *rpm* and $\varepsilon = 0.025$ *cm*, for H = 0.140 *cm* ($\times$, Guinzburg 1992), and H = 0.305 *cm* ($\circ$, current).

obtained by Guinzburg (1992) with comparable data from the current tests. The conical rotor at 2000 *rpm* was used, with the leakage path clearance H= 0.140 *cm* in Guinzburg's test, and H=0.305 *cm* in the current tests. The eccentricity is 0.025 *cm* in both cases. The trends in most of the force coefficients seem to match well, however the magnitudes of the forces for Guinzburg's tests are much larger with the exception of the direct added mass M and cross-coupled damping c. The smaller clearance is expected to cause such an increase in the measured forces, and so these results seem reasonable.

Figure 3.11 shows the rotordynamic force coefficients as a function of the flow

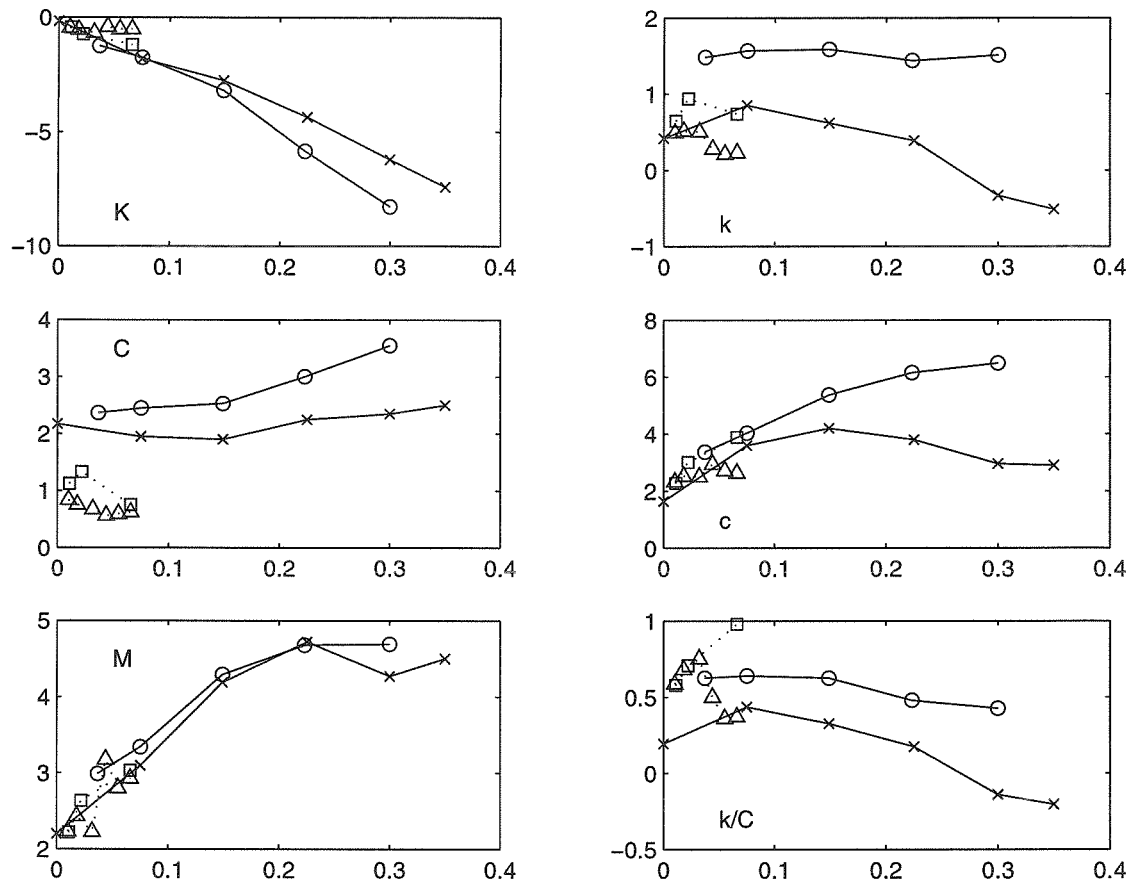

Figure 3.11: Rotordynamic coefficients plotted against the flow coefficient ϕ for the conic geometry (Guinzburg 1993) at 1000 *rpm*, $H = 0.140$ *cm*, and $\varepsilon = 0.118$ *cm* with ($\circ$), and without inlet swirl ($\times$); For the contoured geometry (current) at 1000 *rpm*, $H = 0.305$ *cm*, and $\varepsilon = 0.025$ *cm* with ($\square, \Lambda = 0.6$) and without inlet swirl ($\triangle$).

coefficient for Guinzburg's (1993) and the current tests with and without inlet swirl. Guinzburg's data is for a conical shroud with a clearance of 0.140 *cm*, an eccentricity of 0.118 *cm*, and for flow coefficients over a large range, at 1000 *rpm*. The current data is for a contoured shroud with clearance of 0.305 *cm*, an eccentricity of 0.0254 *cm*, and for a much smaller range of flow coefficients at 1000 *rpm*. It should be noted that the no inlet swirl case studied by Guinzburg is the only set of data which was collected without using an inlet guide vane, as the current zero inlet swirl data were taken using a set of radial vanes for consistency purposes.

As can be seen in figure 3.11, good agreement is observed between the coefficients of the normal force. The trends with increasing flow rate are matched well, and the direct added mass and cross-coupled damping have similar magnitudes for both the case with and without inlet swirl. For the cases with no inlet swirl, similar trends are noted between this plot and figure 3.10, and therefore the path clearance appears to be the explanation of the difference in the magnitudes of the direct stiffness, K.

The force coefficients of the tangential force differ in magnitude and trend, but again the magnitude difference is best explained by a glance at figure 3.10 and noting the leakage path clearances. The differences in trend of the direct damping and cross-coupled stiffness with flow rate appear to be due to the curvature of the contoured rotor compared with the conical rotor as compared in figure 3.7. In both sets of reported data, the same relative difference between the tangential force coeffients with swirl and without inlet swirl is observed. Seperate plots of Guinzburg's data and the current data can be seen in figures 1.3 and 3.6 for clarity.

Figure 3.12 reproduces the data from Sivo (1995) and from the current tests for the conical impeller with and without anti-swirl ribs in the leakage path. The data from Sivo is taken over a larger range of flow coefficients, and the eccentricity and leakage path clearance are both larger in Sivo's tests. The ratio of the eccentricity to the clearance, ε/H, is 0.0833 for the current tests and 0.278 for Sivo's. It is possible that non-linear affects may need to be accounted for with Sivo's data.

The normal force coefficients show the same benefit of improved direct stiffness with the addition of the anti-swirl ribs. The relative difference for cases with ribs and without ribs in the cross-coupled damping and direct added mass is also similar.

The whirl ratio for both sets of data is also similar. The benefit of the ribs occurs only at very small flow coefficients, and the reduction of the whirl ratio with increasing flow rate is observed for the cases without ribs. This is interesting because it appears that the trend of the direct damping is different between Sivo's research and the current work.

For the cases depicted in figure 3.12, the magnitudes of the rotordynamic coefficients can probably be attributed to the clearance, H. The trends with flow rate is

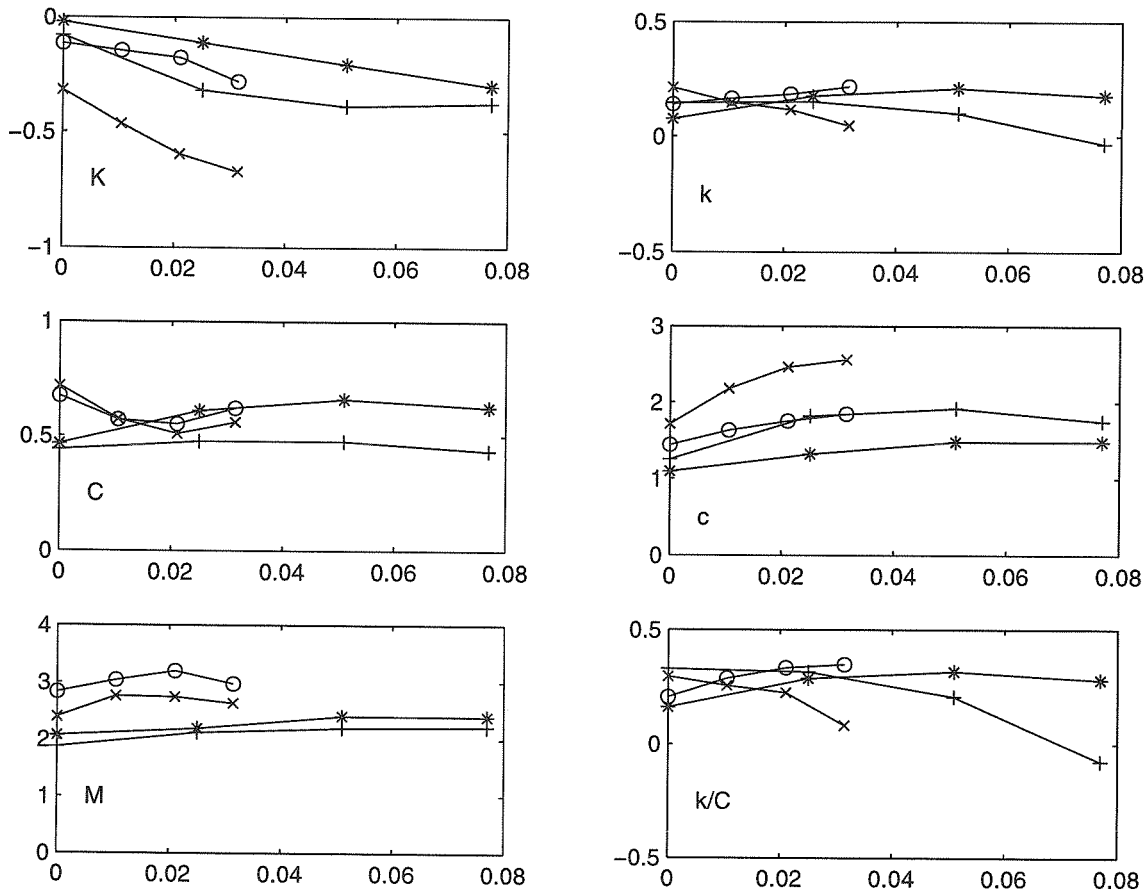

Figure 3.12: Rotordynamic coefficients for the conical rotor with and without anti-swirl ribs. Data at 1000 *rpm*, for $H = 0.424$ *cm*, $\varepsilon = 0.118$ *cm* with $(*)$ and without $(+)$ ribs (Sivo 1995). And for $H = 0.305$ *cm*, $\varepsilon = 0.025$ *cm* with$(\circ)$ and without $(\times)$ ribs (current).

similar between both data sets, with the exception of the direct damping, C. It is not clear why this occurs, but the large eccentricity to clearance ratio in Sivo's tests may partially explain the discrepancy.

Some of the differences observed between rotordynamic force measurements in centrifugal pump leakage paths gathered by various researchers at the Rotor Force Test Facility have been explored. Many similarities are observed in the data as well, despite differences in rotor geometry and test hardware. Throughout the tests examined, the normal force measurements are the most consistent, while the tangential force measurements are sensitive to changes in flow conditions and geometry.

3.8 Discussion

The experimental data from the current research shows good agreement with previous work in the area of fluid-induced rotordynamic forces in pump leakage paths. The functional dependence of the forces on whirl frequency ratio was fairly consistent and allowed use of the rotordynamic force coefficients for meaningful comparisons. The reduction of the whirl ratio with increasing flow coefficient was observed with the conical geometry, and there are indications that this is also the case for contoured rotors with more typical geometry, but this occurs at much higher flow rates than those tested. The increase in the normal force as the flow rate increases is also observed.

A short axial length decreases the magnitude of all the rotordynamic force coefficients. As the forces are nondimensionalized by the axial length, this implies that the forces are quite small for the shorter contoured impeller, and that the nondimensionalization with the axial length will not reduce the forces on the rotors with similar profiles to uniform values. The effect of the curvature in comparing impellers of similar axial length appears only in the cross-coupled stiffness for the case with no swirl, but is significant for both tangential force coefficients for the case with swirl.

The effect of the wear ring and face seal with the contoured leakage path seems to match the effects observed for similar impellers tested by Bolleter. The low pressure seal plays a large role in determining the behavior of the entire annulus, especially in increasing the direct stiffness. This may be simply the Lomakin effect (Brennen, 1994) contribution from the radial clearance seal. Due to a reduced axial velocity, the entrance losses to the seal are smaller, and hence the mean pressure is higher on the side of the seal with smaller clearance. This higher pressure gives rise to a restoring force on the side of the seal with smaller clearance, and therefore a positive direct stiffness. However, a calculation using Childs' "short seal" analytic solution for just the seal of the impeller yielded a stiffness which, when added to the value of the stiffness for the impeller alone, should cause an increase of about 10%. There may be more than a Lomakin effect causing the increase in stiffness, or perhaps there

are interactions between the seal and the shroud which invalidate the summation of the coefficients of the seperate devices. Table 1.1 seems to indicate that the seal is responsible for a much larger contribution to the stiffness than this simple calculation would indicate.

The high pressure seal has the opposite effect: the direct stiffness decreases when compared to the case without the orifice. The tangential force with an orifice is also much larger in magnitude. Again, the cross-coupled damping and direct added mass are not affected as much as the other rotordynamic force coefficients.

The tests with inlet swirl indicate that fluid effects are similar to the geometrical effects of the seals. The direct stiffness, direct damping, and cross-coupled stiffness appear to show the greatest change between cases with and without inlet swirl. The magnitude of the fluid pre-rotation into the path does not appear to be very great. It is postulated that the effect of inlet swirl is felt only at the inlet of the leakage path, and that the viscous effects dominate thereafter. Inlet swirl seems to have very different effects on the tangential force for the conic and contoured geometries, and appears to be more destabilizing with increasing flow rate for the case with curvature.

The experiments with anti-swirl ribs of different lengths in the leakage path seem to corroborate this idea. Almost no change is noted for the direct added mass and cross-coupled stiffness. Any anti-swirl structure at the inlet, either full length or tip ribs, appears to offer an increase in the direct stiffness. The eye ribs offer increases in the tangential force coefficients, indicating that disrupting the flow midway through the leakage path has some beneficial effect on the rotordynamic stability by reducing the whirl ratio compared with other rib configurations. This finding is consistent with Bolleter's swirl brake for the increased direct damping, and may be consistent with the cross-coupled stiffness depending on the leakage flow rate.

From the experiments, it is clear that the inlet and discharge of the leakage path will have very important effects on the rotordynamic behavior of shrouded centrifugal pumps. Whether structural parameters like seal geometry and anti-swirl ribs, or fluid parameters such as varying inlet swirl, the resulting changes in the direct stiffness, cross-coupled stiffness, and direct damping will affect the rotordynamic stability and

present challenging problems in defining the boundary conditions in any numerical simulation.

Chapter 4 Theoretical Model

4.1 Bulk Flow Model

The bulk-flow model of the discharge-to-inlet leakage flow developed by Childs (1989) is particularly valuable for its simplicity and ease of computation. Based on Hirs (1973) lubrication equations, the bulk flow model uses simple correlations for the shear stresses based on the gap averaged flow velocities. This model, in its perturbation solution form, is widely regarded as a useful rotordynamic analysis tool for problems with relatively simple computational domains.

As presented by Childs, the bulk flow model assumes that the three-dimensional, unsteady, turbulent flow in an annulus can be accurately approximated by reducing the dimensions of the flow from three to two, by using a simple correlation between the shear stresses and gap averaged velocities, and by treating the rotordynamic flow as a linear perturbation on the mean flow. Each of these assumptions should be carefully considered when using this approach to model the flow in a more complex computational domain such as a centrifugal pump leakage annulus.

The assumption that the dimensions of the flow can be reduced from three to two is common and leads to the Reynolds lubrication equations. It implies that the velocity profiles within the annulus are self-similar and therefore, the equations of the flow can be averaged over the gap without excessive error. This may have limitations under certain conditions noted in experiments in which flow reversals and recirculation zones occur in the leakage path (Sivo *et al.* , 1994b; Guelich *et al.* , 1989). These changes in flow direction may lead to frictional stresses which are acting in a direction opposite to those predicted by the gap averaged velocity. Certain 3-D computational analyses have observed these flow reversals (Baskharone & Hensel, 1993). With regions of recirculation occuring in different parts of the gap, and changing with different flow rates and impeller speeds, a serious limitation may be noted with this assumption of

a two-dimensional domain.

The Reynolds number of most leakage flows is very high. This means the bulk flow model requires expressions which relate the turbulent shear stresses to the averaged velocities in the gap. In the current form of the bulk flow model, the shear stresses on the rotor and the stator are calculated using friction coefficients (Hirs, 1973). These are defined by:

$$\frac{\tau}{\frac{1}{2}\rho u^2} = n\left(\frac{\rho u h}{\eta}\right)^m \tag{4.1}$$

where u is the gap-averaged velocity relative to the surface under consideration, and the m and n are denoted by m_S and n_S for the stator and m_R and n_R for the rotor. These expressions, which are a simple and heuristic extrapolation from the correlations for turbulent flow in a pipe, are taken from the work of Hirs who does, however, recommend that the coefficients m and n be "fitted to individual experiments." The frictional coefficients are dependent on six physical parameters, including the curvature of the surface, inertial effects, and roughness. Other work suggests different empirical coefficients for the same smooth concentric seal studied by Hirs (Yamada, 1962). Thus, the coefficients may not fully account for the curvature of the rotor in a particular leakage geometry or the inertial effects due to the curved path of the bulk flow. Nor will the roughness parameters be easy to gauge. Given the ease with which the frictional factors can be altered in the computational model, it is reasonable to consider fitting them so as to match the experimental data base provided one could have reasonable confidence that one was not sweeping other and different deficiences under this rug. As stated previously any reversal in flow direction near the impeller implies a serious error in the correlation of equation 4.1. The sign of the wall-shear stress term for the rotor should change in a region of reverse flow. This could, in part, be incorporated into the bulk flow analysis by using smaller values of n_R.

In fact, the use of the above expressions for the turbulent shear stresses are subject to an even more general criticism. They are correlations for steady turbulent flows based, primarily, on experimental observations of steady flows. In contrast, the rotordynamic flows of concern here are fundamentally unsteady. The problem is that

very little is known about turbulent flows which are unsteady in the sense that the flow is being externally excited in an unsteady way. Therefore, correlations such as that given above are useful as there are no alternatives, but it must be recognized that the unsteady flows of the present context may lead to substantial deviations from these correlations. At present, this issue can only be resolved by careful comparison of the experimental and model results.

Finally, Childs treats the rotordynamic flow as a linear perturbation on the mean flow in the annulus. While this may be an accurate assumption for very small eccentricities, there is currently no way to know at what eccentricity this linearization begins to lose accuracy.

Even if the basic equations are accurate, there is more doubt about the boundary conditions that Childs' employs at the inlet to and discharge from the leakage flow. For example, Childs' deploys a constant pressure condition as well as a uniform swirl velocity condition at inlet. Perhaps the first should be a constant total head condition instead. Moreover, it is assumed that the hydraulic loss through the orifices at inlet and discharge are related only to the meridional velocity (or flow rate) and are independent of the swirl velocity.

So, while Childs' model was certainly a major step forward, there remain many questions which require resolution before a reliable predictive tool is available.

4.2 Description of Bulk Flow Model

Black and his co-workers (Black, 1969; Black & Jensen, 1970) were the first to attempt to identify and model the rotordynamics of turbulent annular seals. Bulk flow models (similar to those of Reynolds lubrication equations) were used. Several deficiencies in this early work caused Childs (1983a, 1983b) to publish a revised version of the bulk flow model for turbulent annular seals (Childs & Dressman, 1982; Childs & Dressman, 1985; Childs & Kim, 1985; Childs & Scharrer, 1986) and later to extend this model (Childs, 1987; Childs, 1989) to examine the rotordynamic characteristics of discharge-to-suction leakage flows around shrouded centrifugal pump impellers. The geometry

is sketched in figure 4.1, and is described by coordinates of the meridian of the gap as given by $Z(s)$ and $R(s)$, $0 < s < L$, where the coordinate, s, is measured along that meridian. The clearance is denoted by $H(s, \Theta, t)$ where the mean, non-whirling clearance is given by $\bar{H}(s)$.

The equations governing the bulk flow are averaged over the gap. This leads to a continuity equation of the form:

$$\frac{\partial H}{\partial t} + \frac{\partial}{\partial s}(Hu_s) + \frac{1}{R}\frac{\partial}{\partial \Theta}(Hu_\Theta) + \frac{Hu_s}{R}\frac{dR}{ds} = 0 \tag{4.2}$$

where u_s and u_Θ are gap-averaged velocities in the s and Θ directions. The meridional and circumferential momentum equations are:

$$-\frac{1}{\rho}\frac{\partial p}{\partial s} = \frac{\tau_{Ss}}{\rho H} + \frac{\tau_{Rs}}{\rho H} - \frac{u_\Theta^2}{R}\frac{dR}{ds} + \frac{\partial u_s}{\partial t} + \frac{u_\Theta}{R}\frac{\partial u_s}{\partial \Theta} + u_s\frac{\partial u_s}{\partial s} \tag{4.3}$$

$$-\frac{1}{\rho R}\frac{\partial p}{\partial \Theta} = \frac{\tau_{S\Theta}}{\rho H} + \frac{\tau_{R\Theta}}{\rho H} + \frac{\partial u_\Theta}{\partial t} + \frac{u_\Theta}{R}\frac{\partial u_\Theta}{\partial \Theta} + u_s\frac{\partial u_\Theta}{\partial s} + \frac{u_\Theta u_s}{R}\frac{\partial R}{\partial s} \tag{4.4}$$

We note that the equations not only include the viscous terms commonly included in lubrication analyses (for example, (Pinkus & Sternlicht, 1961)) but also the inertial terms (Fritz, 1970) which are necessary for the evaluation of the rotordynamic coefficients.

To determine the turbulent shear stresses, Childs employed the approach used by Hirs (1973). The turbulent shear stresses, τ_{Ss} and $\tau_{S\Theta}$, applied to the stator by the fluid in the s and Θ directions are given by:

$$\frac{\tau_{Ss}}{\rho u_s} = \frac{\tau_{S\Theta}}{\rho u_\Theta} = \frac{n_S}{2}\left[u_s^2 + u_\Theta^2\right]^{\frac{m_S+1}{2}}(H/\nu)^{m_S} \tag{4.5}$$

and the stresses, τ_{Rs} and $\tau_{R\Theta}$, applied to the rotor by the fluid in the same directions:

$$\frac{\tau_{Rs}}{\rho u_s} = \frac{\tau_{R\Theta}}{\rho(u_\Theta - \Omega R)} = \frac{n_R}{2}\left[u_s^2 + (u_\Theta - \Omega R)^2\right]^{\frac{m_R+1}{2}}(H/\nu)^{m_R} \tag{4.6}$$

where the constants n_S, n_R, m_S and m_R are chosen to fit the available data on

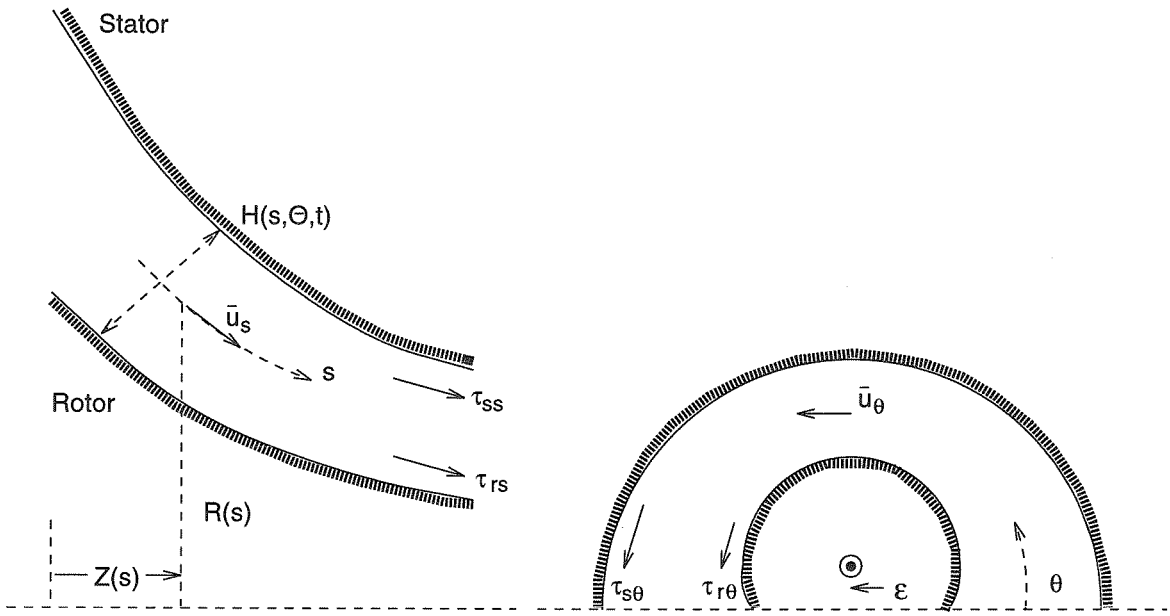

Figure 4.1: Sketch of fluid filled annulus between a rotor and a stator for turbulent lubrication analysis.

turbulent shear stresses. Childs (1983a) uses typical values of these constants from simple pipe flow correlations:

$$n_S = n_R = 0.0664 \quad ; \quad m_S = m_R = -0.25 \tag{4.7}$$

The work of Yamada, (1962) used subsequently by Childs, reported values for these constants to be:

$$n_S = n_R = 0.079 \quad ; \quad m_S = m_R = -0.25 \tag{4.8}$$

These wall shear stress terms are again a simple correlation of the Reynolds number (eqn. 4.1), using the magnitude of the two components of gap-averaged velocity. No consideration is given to the unsteady nature of rotordynamic flows, and the values of the constants are not well established. More realistic values of the frictional factors to account for surface roughness and laminar to turbulent transition have been studied recently and may result in considerable improvement of the estimates of these factors (Zirkelback & San Andres, 1996).

Childs then proceeds to linearize the equations by dividing the clearance, pressure, and velocities into mean components (subscript 0) that would pertain in the absence of whirl, and small, linear perturbations (subscript 1) due to an eccentricity, ϵ, rotating at the whirl frequency, Ω. He develops differential equations for the coefficients which are functions of r only, with the perturbation velocities restrained to harmonic functions of θ. These zero and first order equations can be solved analytically for very simple geometries, such as straight seals.

4.2.1 Childs' Perturbation Solution

Using Childs' approach, the above set of equations, 4.2 to 4.4 can be numerically integrated, particularly in the case of more complex geometries. The perturbation of the mean (zero order) solution is used for deducing the rotordynamic behavior. A detailed description of this method of solution can be found in (Guinzburg, 1992).

In summary, the annulus is assumed to be circumferentially symmetric in the undisplaced position. The velocity and pressure components are then calculated as a functions of coordinates and time. The governing equations are then solved using a perturbation expansion of terms linear in the eccentricity, ε. Guinzburg used a fourth order Runge-Kutta scheme to numerically integrate two ordinary differential equations for p_o and $u_{\theta o}$, as functions of the path variable s, that result from manipulation of the momentum equations 4.3 and 4.4. This requires two initial conditions to solve for $u_{\theta o}(s)$ and $p_o(s)$, which lead to the constant swirl at the inlet for u_θ and a constant pressure condition for the static pressure p.

This version of the bulk flow model predicted large unexplainable resonances in the calculated forces for cases in which inlet swirl was present (the $u_{\theta o}(s)$ is nonzero at $s = 0$). Sivo observed that these resonances could be substantially reduced if, in the analysis (Childs, 1989), the β_0 and β_1 factors of the path velocity term $A_{3\theta}$ in the first-order circumferential momentum equation were set to zero. This amounts to an assumption that the product of the eccentricity and the first-order path velocity is small compared to the zero-order path velocity in the wall shear terms. This is not ob-

vious from the definitions given in Childs (1989) where the first-order circumferential equation is given as:

$$b\frac{L_s}{R_i}\frac{1}{r}\varepsilon\frac{\partial p_1}{\partial\theta} = \varepsilon h_1 A_{1\theta} - \varepsilon u_{\theta 1} A_{2\theta} - \varepsilon u_{s1} A_{3\theta} - (Inertial \quad terms) \tag{4.9}$$

the expansion of the $A_{3\theta}$ term is:

$$A_{3\theta} = \frac{\sigma_r}{2}(u_{\theta 0}-r)[mr-(1+mr)\beta_0(u_{\theta 0}-r)/u_{s0}]+\frac{\sigma_s}{2}u_{\theta 0}[ms-(1-ms)\beta_1 u_{\theta 0}/u_{s0}] \tag{4.10}$$

and the β terms are:

$$\beta_0 = \frac{u_{\theta 0}-r}{b^2 u_{s0}}\frac{1}{(1+[\frac{u_{\theta 0}-r}{bu_{s0}}]^2)} \tag{4.11}$$

$$\beta_1 = \frac{u_{\theta 0}}{b^2 u_{s0}}\frac{1}{(1+[\frac{u_{\theta 0}}{bu_{s0}}]^2)} \tag{4.12}$$

In this formulation, $b = V_i/R_i\omega$, V_i is the inlet path velocity, R_i is the inlet radius, $r = R/R_i$, and L_s is the total length of the leakage path. However, in the derivation of the first-order circumferential equation, from the treatment of the flow variables as the sum of zero and first order terms, an approximation for the average velocity is reached in which, for example in the $\tau_{R\theta}$ term, the following expression results:

$$[1+\frac{1}{b^2}\frac{u_{\theta 0}^2}{u_{s0}^2}(1-\frac{r}{u_{\theta 0}})(1-2\varepsilon\frac{u_{s1}}{u_{s0}})]^{\frac{mr+1}{2}} \tag{4.13}$$

The β_1 term results from retaining the $2\varepsilon u_{s1}/u_{s0}$ in the expression for $\tau_{S\theta}$ and the β_0 term results from retaining an identical term in the equations for $\tau_{R\theta}$. While this approximation is arbitrary (but plausible), it is clear that it plays a very significant role in the prediction of the forces. One practical advantage of this arbitrary omission is that it allows comparison of the general trends predicted by the model without the confusion the resonances introduce.

Figure 4.2 shows the rotordynamic forces plotted as functions of the whirl frequency ratio Ω/ω for the case of contoured impeller, with the β terms and without the β terms, compared with experimental data for a flow coefficient $\phi = 0.009$, and

an inlet swirl ratio $\Lambda = 0.5$. A marked reduction in "resonances" is observed for this case, as well as closer agreement with the experimental data.

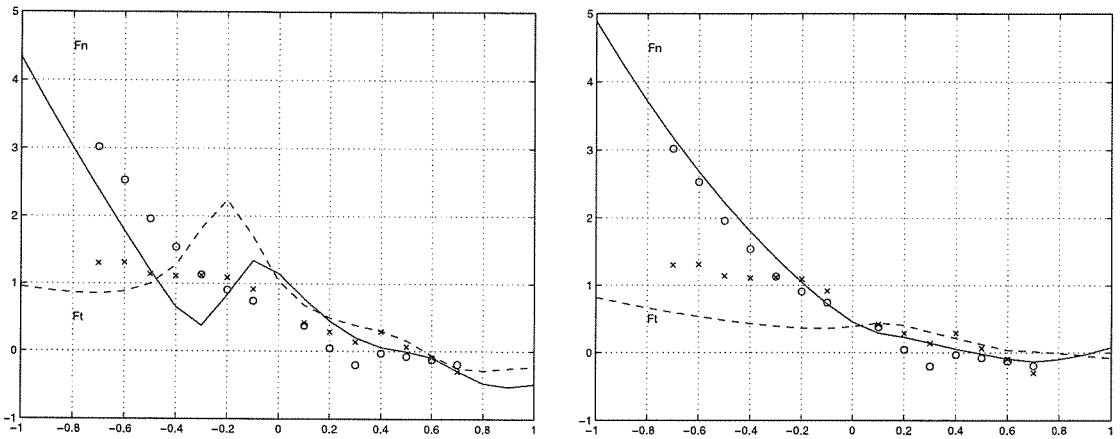

Figure 4.2: Experimental and computed rotordynamic forces plotted against whirl frequency ratio Ω/ω for $\phi = 0.009$ and $\Lambda = 0.5$. With β terms (left) and without β terms (right) included in the evaluation.

4.3 Stream Function and Vorticity Equations

The resonances predicted in Childs' perturbation model caused much controversy, and the work of Guinzburg eventually dismissed the possibility of these abrupt force fluctuations. Childs' perturbation solution of the bulk flow was developed when computing capability was somewhat limited, and so this method of solution proved expedient. By reducing the problem to where the flow variables are assumed to be sinusoidal in the circumferential direction and harmonic in time, a solution could be found with minimum computation. A new method of solving the bulk flow equations without resorting to linearization in eccentricity or assuming harmonic forms for the flow variables is proposed. In this new formulation, evolutionary equations for a vorticity and total pressure will shed some insight into the physical properties of these rotordynamic flows.

For a case with a steady whirl and constant eccentricity, ϵ, rotating at the whirl

frequency, Ω, which is superimposed on the shaft rotation with radian frequency, ω, a method of solving the bulk flow equations using a stream function and vorticity is formulated. With this set of assumptions, the fluid flow in a frame of reference rotating at Ω is steady and it is appropriate to rewrite the equations and to solve them in this rotating frame. Defining, therefore, a new angular variable, θ, and a new angular velocity, u_θ, in this rotating frame such that

$$\theta = \Theta - \Omega t \quad ; \quad u_\theta = u_\Theta - \Omega R \tag{4.14}$$

it follows that the continuity equation, Eqn. 4.2, can be written as

$$\frac{\partial}{\partial \theta}\{H u_\theta\} + \frac{\partial}{\partial s}\{R H u_s\} = 0 \tag{4.15}$$

and this is most easily satisfied by defining a stream function, $\psi(s, \theta)$ such that

$$u_s = \frac{1}{RH}\frac{\partial \psi}{\partial \theta} \quad ; \quad u_\theta = -\frac{1}{H}\frac{\partial \psi}{\partial s} \tag{4.16}$$

It follows that the total volume flow rate, Q, at any meridional location, s, is given by

$$Q = \psi(s, 2\pi) - \psi(s, 0) \tag{4.17}$$

and this provides a periodic boundary condition on ψ in the θ direction.

In the rotating frame of reference, the equations of motion are usefully written using an appropriate total pressure, P, instead of the static pressure, p, where

$$\frac{P}{\rho} = \frac{p}{\rho} + \frac{1}{2}(u_s^2 + u_\theta^2 - R^2\Omega^2) \tag{4.18}$$

and the equations of motion, equations (4.3) and (4.4), then become

$$\frac{\partial}{\partial s}\left(\frac{P}{\rho}\right) = -H u_\theta \Gamma - u_s(g_S + g_R) \tag{4.19}$$

$$\frac{1}{R}\frac{\partial}{\partial\theta}\left(\frac{P}{\rho}\right) = Hu_s\Gamma - (u_\theta + \Omega R)(g_S + g_R) + \omega R g_R \tag{4.20}$$

where the functions, g_S and g_R, are the shear stress terms for the stator and rotor respectively. For want of a better shear stress model, we follow Childs in using Hir's (1973) correlations which, written in terms of the rotating frame, are given by:

$$g_S = \frac{n_S}{2H}\left(\frac{H}{\nu}\right)^{m_S}\left\{u_s^2 + (u_\theta + \Omega R)^2\right\}^{\frac{m_S+1}{2}} \tag{4.21}$$

$$g_R = \frac{n_R}{2H}\left(\frac{H}{\nu}\right)^{m_R}\left\{u_s^2 + (u_\theta + \Omega R - \omega R)^2\right\}^{\frac{m_R+1}{2}} \tag{4.22}$$

The important quantity, Γ, given by

$$\Gamma = \frac{1}{H}\left[-\frac{1}{R}\frac{\partial}{\partial s}(Ru_\theta + \Omega R^2) + \frac{1}{R^2}\frac{\partial}{\partial\theta}(Ru_s)\right] \tag{4.23}$$

plays a crucial role both in understanding the fluid mechanics of these flows and in the solution methodology. This quantity, Γ, can be termed an "effective vorticity", and the existence of such a quantity has led to the development of the current methodology.

The vorticity, Γ, is a fundamental property of the flow; this can be discerned by eliminating P from equations (4.19) and (4.20) to obtain the basic convection equation for Γ:

$$u_s\frac{\partial\Gamma}{\partial s} + u_\theta\frac{1}{R}\frac{\partial\Gamma}{\partial\theta} = \frac{1}{RH}\left[\frac{\partial}{\partial s}\left\{R(u_\theta + \Omega R)(g_S + g_R) - \omega R^2 g_R\right\} - \frac{\partial}{\partial\theta}\left\{u_s(g_S + g_R)\right\}\right] \tag{4.24}$$

which demonstrates that, in the absence of viscous effects ($g_S = g_R = 0$), the vorticity is invariant along any streamline. Conversely, the shear stresses are alone responsible for any change in Γ along a streamline. If ξ is a coordinate measured along a streamline, then equation (4.24) clearly implies that

$$\frac{\partial\Gamma}{\partial\xi} = \frac{1}{RH(u_s^2 + u_\theta^2)^{\frac{1}{2}}}\left[\frac{\partial}{\partial s}\left\{R(u_\theta + \Omega R)(g_S + g_R) - \omega R^2 g_R\right\} - \frac{\partial}{\partial\theta}\left\{u_s(g_S + g_R)\right\}\right] \tag{4.25}$$

The total pressure is obtained by integration similar to that for the vorticity, Γ. From equations (4.19) and (4.20) it follows that

$$\frac{\partial}{\partial \xi}\left(\frac{P}{\rho}\right) = \frac{1}{(u_s^2 + u_\theta^2)^{\frac{1}{2}}}\left[\omega R u_\theta g_R - \left\{u_s^2 + u_\theta(u_\theta + \Omega R)\right\}(g_R + g_S)\right] \tag{4.26}$$

which demonstrates the the total pressure (or energy in the flow) is constant along a streamline in the absence of viscous effects. Furthermore, when written in the above manner, the governing equations, (4.25) and (4.26), indicate a physically reasonable approach to their numerical solution by iterative means.

4.4 Stream Function and Vorticity (SV) Solution

It follows from the last section that one method for the solution of the equations for a rotordynamic flow proceeds as follows:

(1) First, for given or guessed values of the vorticity, $\Gamma(s,\theta)$, we solve the Poisson-like equation (4.23) for the stream function, $\psi(s,\theta)$:

$$\frac{\partial}{\partial s}\left\{\frac{R}{H}\frac{\partial \psi}{\partial s} - \Omega R^2\right\} + \frac{1}{R}\frac{\partial}{\partial \theta}\left\{\frac{1}{H}\frac{\partial \psi}{\partial \theta}\right\} = RH\Gamma \tag{4.27}$$

and thereby obtain new values for $\psi(s,\theta)$, $u_s(s,\theta)$ and $u_\theta(s,\theta)$. For this purpose we deploy boundary conditions on ψ as follows:

(i) Along $s = 0$, we specify an inlet swirl velocity, $u_\theta(0,\theta)$, which, in order to satisfy conservation of angular momentum, should normally be put equal to the swirl velocity in the reservoir upstream of the inlet.

(ii) An appropriate boundary condition at discharge, $s = S$, would be that the pressure in the flow exiting the annulus should be uniform for all θ or

$$\left(\frac{\partial p}{\partial \theta}\right)_{s=S} = 0 \tag{4.28}$$

(iii) The periodic conditions on boundaries at $\theta = 0$ and $\theta = 2\pi$ such that

$$\psi(s, 2\pi) - \psi(s, 0) = Q \tag{4.29}$$

(2) Second, given the new values of $\psi(s,\theta)$, $u_s(s,\theta)$ and $u_\theta(s,\theta)$, we can proceed to integrate along streamlines or otherwise to find new values for $\Gamma(s,\theta)$ using equation (4.25). For this purpose the shear stress functions, g_R and g_S must be evaluated. As the relations for Γ and P, the total pressure, are quite similar, the total pressure can also be calculated during this integration using equation (4.26).

These steps are then repeated until the solution converges.

Having obtained convergence, the total pressure, P, pressure, p, and the rotordynamic forces are evaluated as follows. Since the viscous terms were found to be small in these calculations it is sensible to integrate equation (4.26) along a streamline in parallel with the Γ integration and so obtain the total pressure everywhere. If entrance losses are neglected between the upstream reservoir at the inlet plane ($s = 0$), then this integration begins with a uniform value of $P(0,\theta)$ equal to the total pressure in the reservoir, P_{res}, and this can conveniently be chosen to be zero without loss of generality. On the other hand if entrance losses are to be included then $P(0,\theta)$ can be set to a value smaller than P_{res} by an amount equal to the entrance loss at that particular θ position. Other complications which could be incorporated include a non-uniform upstream reservoir (such as the volute of a pump operating off-design) which would imply a circumferentially varying $P(0,\theta)$. Having obtained $P(s,\theta)$ throughout the flow field, the pressure, $p(s,\theta)$, follows simply from the definition (4.18).

With the pressure (and the viscous shear stresses) it only remains to integrate these to obtain the normal and tangential forces acting on the rotor. With the sign convention as defined in figure 1.1 it follows that:

$$F_n = \int_0^S \left\{1 - \left(\frac{dR}{ds}\right)^2\right\}^{\frac{1}{2}} \int_0^{2\pi} \left(p\cos\theta + \tau_{R\theta}\sin\theta\right) R d\theta \quad ds \tag{4.30}$$

$$F_t = \int_0^S \left\{ 1 - \left(\frac{dR}{ds} \right)^2 \right\}^{\frac{1}{2}} \int_0^{2\pi} \left(p \sin\theta - \tau_{R\theta} \cos\theta \right) R d\theta \quad ds \tag{4.31}$$

In most of the results presented the contributions from the $\tau_{R\theta}$ parts of these integrals are very small and can be neglected.

4.5 Details of SV Method

This section explains the development of the Stream Function/Vorticity Method and its application to test cases of interest. The details of the boundary conditions and programming the convection relations are included. Uncertainties in each of the described boundary conditions lead to differences in the rotordynamic forces and flow variables.

4.5.1 Downstream Boundary Condition

There are two possible ways two formulate the downstream boundary that are considered. According to equation (4.28), a constant static pressure in the circumferential direction is desired. It might also be possible to approximate this with a constant tangential velocity at the discharge. Convergent results have been acheived using both, but large differences in the calculated unsteady forces are observed.

The downstream boundary condition was first formulated as a constant static pressure in the circumferential direction. Initially, the values for u_θ and u_s at the discharge are used to find an average static pressure at the discharge, given by the definition of total pressure:

$$\overline{\frac{2p}{\rho}} = \frac{1}{JT} \sum_{\theta}^{JT} \left(\frac{2P}{\rho} - u_\theta^2 - u_s^2 + R^2\Omega^2 \right) \tag{4.32}$$

Here P is the total pressure which results from the convection and dissipation through the domain. Then, a u_θ, based on the new average static pressure, is calculated at each circumferential point of the discharge, using the same relation as in eqn. (4.32).

$$u_\theta^2 = -\frac{\overline{2p}}{\rho} + \frac{2P}{\rho} - u_s^2 + R^2\Omega^2 \tag{4.33}$$

The value of u_θ is solved for in the above expression using a relaxation method, and a value for the change in ψ, the stream function, at each JT (theta) location is determined using:

$$\Delta\psi = \psi_{(JS-1,JT)} - \psi_{(JS+1,JT)} + 2 * DS * H * (u_\theta) \tag{4.34}$$

The value of the stream function at the position, $JS+1$, just downstream of the discharge, is then recalculated at each angular location as:

$$\psi_{(JS+1,JT)} = \psi_{(JS+1,JT)} + RF * \Delta\psi \tag{4.35}$$

where RF is the relaxation factor of an iterative calculation. The values of the stream function in the remainder of the domain are then solved using Successive Over Relaxation (Press *et al.* , 1992) for the Poisson-like equation, (4.27), subject to a combination of this downstream boundary condition, the upstream boundary condition, and the volumetric flow condition in the circumferential direction.

This downstream boundary condition has some possible drawbacks. The average pressure cannot be directly applied to the stream function values, resulting in the use of equation (4.33) and the tangential velocity. Also, the total pressure P accounts for losses in the path due to viscosity. If there are for example, exit losses to account for at the discharge where the Bernoulli expression (4.18) is not true, then problems might be expected. However, a constant static pressure seems to be a natural boundary condition for this problem, and convergent results have been acheived.

A way to approximate the constant static pressure over the discharge without relying on the Bernoulli equation of total pressure is to alternately represent the downstream boundary condition as a constant tangential velocity around the discharge. Namely:

$$\left(\frac{\partial u_\theta}{\partial\theta}\right)_{s=S} = 0 \tag{4.36}$$

This provides a second possible downstream boundary condition for the solution of the bulk flow equations. At the exit, an average circumferential velocity around the discharge is first calculated using the current values of the stream function, ψ:

$$\overline{u_\theta} = \frac{1}{JT}\sum_{\theta=0}^{JT} \frac{\psi_{(JS+1,JT)} - \psi_{(JS-1,JT)}}{2 * DS * H} \tag{4.37}$$

This value of $\overline{u_\theta}$ is then used to find a change in ψ, the stream function at each JT (theta) location:

$$\Delta\psi = \psi_{(JS-1,JT)} - \psi_{(JS+1,JT)} + 2 * DS * H * (\overline{u_\theta}) \tag{4.38}$$

From here, the determination of the new values of the stream function at the discharge proceeds as described earlier in equation (4.35).

The differences in each of these boundary conditions, applied to the case of the conical leakage path, at a flow coefficient of $\phi = .06$, an inlet swirl of 0.5, and a whirl frequency ratio $\Omega/\omega = .3$ can be seen in the plots of the flow variables, Γ, u_s, u_θ and p (the static pressure) in figures 4.3 (constant p) and 4.4 (constant u_θ). Here JT in the mesh location corresponds to the increments in the circumferential direction, and JS corresponds to increments in the path direction. The velocities are nondimensionalized by the tip speed and the pressure is also normalized by a dynamic pressure based on the tip velocity.

The plots for this particular set of flow parameters and geometry are similar except for the path velocity. While the steady increase in the path velocity is observed in both cases, the profile in the θ direction at the discharge is markedly different. The pressure and circumferential velocity at the discharge in either case appear to be unchanging in the θ-direction. There are, however, very subtle differences in the pressure which cause the normal and tangential force to be very inconsistent. Table 4.1 shows the rotordynamic forces calculated for this test case for each of the downstream boundary conditions.

It is clear that the rotordynamic forces are very sensitive to small changes in the pressure. The pressure drop in this case is approximately 16.6 kPa while in a matching

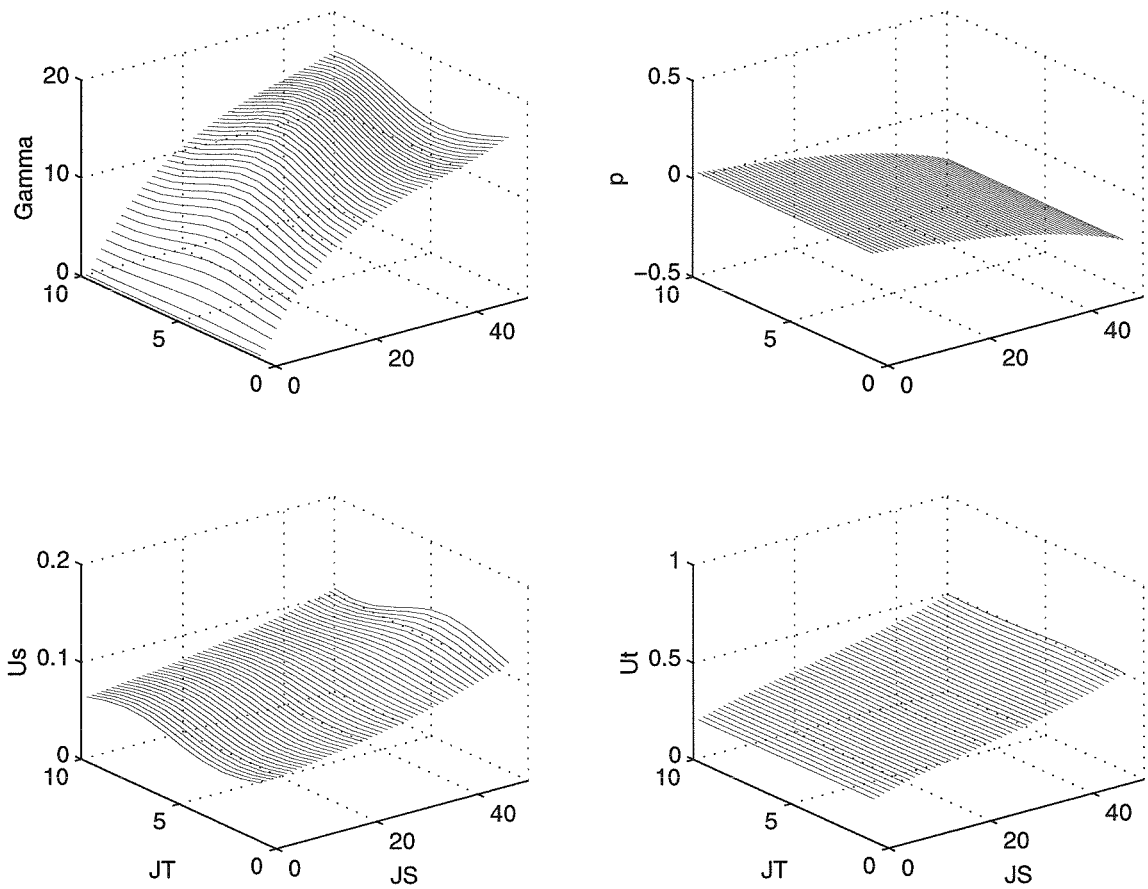

Figure 4.3: Plot of normalized flow variables against mesh location for the conical leakage path. Results using 50x10 grid size, a whirl ratio $\Omega/\omega = .3$ and $\phi = .06$. Constant pressure downstream boundary.

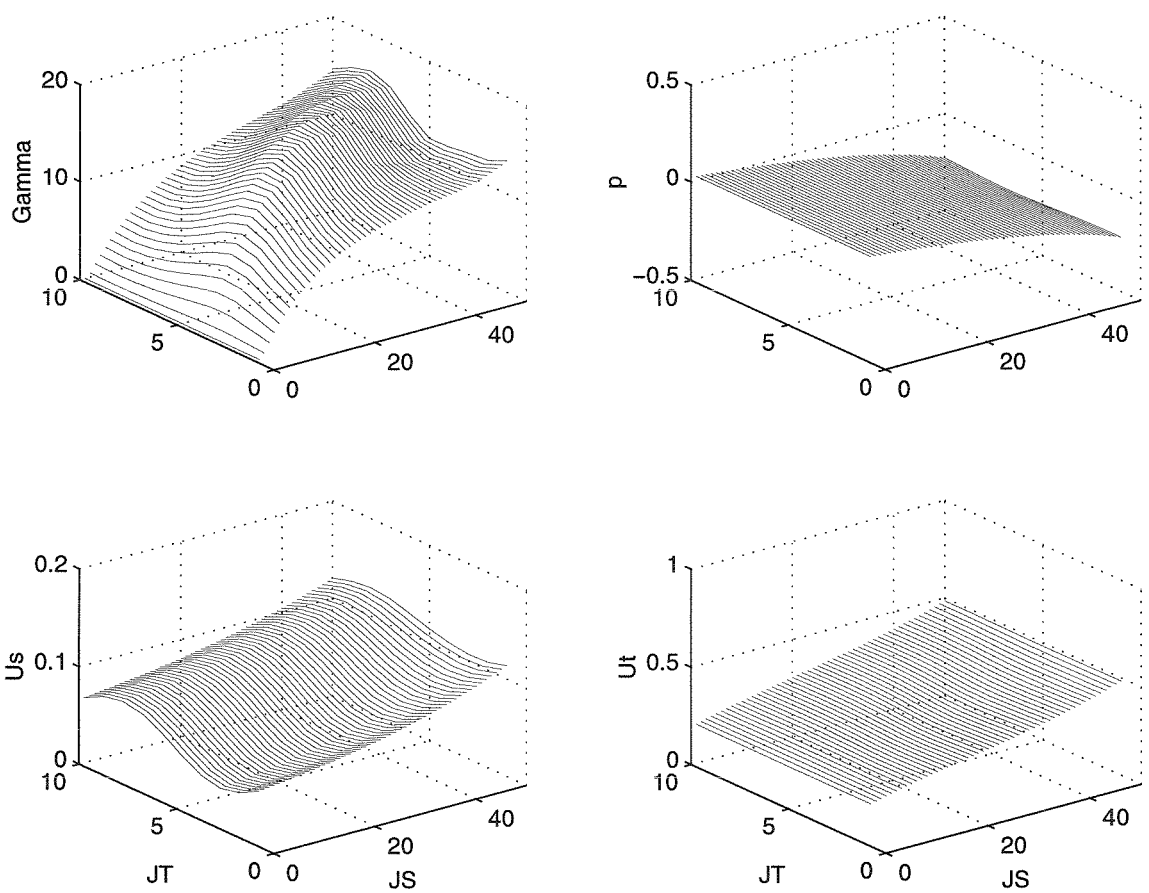

Figure 4.4: Plot of normalized flow variables against mesh location for the conical leakage path. Results using 50x10 grid size, a whirl ratio $\Omega/\omega = .3$ and $\phi = .06$. Constant u_θ downstream boundary.

Downstream Bdry	F_n	F_t
Const p	0.3011	0.277
Const u_θ	0.9658	0.5341

Table 4.1: Forces for the conical leakage path, $\Omega/\omega = .3$, $\phi = .06$ using indicated downstream boundary conditions.

experiment the total pressure drop across the leakage path, including the low pressure seal, was 84.5 kPa, a substantial discrepancy. As the constant pressure downstream boundary condition seems to be most intuitive, the constant circumferential velocity condition will be used only when needed. Unless otherwise noted in subsequent results, the constant pressure downstream boundary is used.

4.5.2 Upstream Boundary Condition

The upstream boundary condition, given as a constant inlet swirl velocity $u_\theta(0,\theta) = \Lambda$, is an important parameter in the calculation. This is readily imposed as a condition on the stream function ψ using the derivation of u_θ in (4.16).

However, from the definition of vorticity (eqn. 4.24), the inlet swirl is only part of the complete initial condition, as the gradients of u_s in the θ direction and $R(u_\theta + R\Omega)$ in the s direction must be properly specified to determine Γ. Through convection, the vorticity values in the rest of the domain are dependent on the upstream value of Γ.

Without knowledge of the two gradients beforehand, only a rough estimate of Γ at the upstream boundary could be made. As the velocity profiles developed in the course of the computation, the values of Γ at the upstream boundary were then adjusted so that the gradients of the path and tangential velocities could be included. The vorticity in the domain was used to extrapolate the upstream values of Γ. This resulted in a calculated upstream vorticity which seemed to be independent of the initial guess.

4.5.3 Convection Calculation

The first version of the SV method involved projecting Γ, and hence the total pressure, P, along a streamline. The bulk flow equations were solved at each node of the mesh by finding the streamline which intersected it, estimating the values of Γ and P at a previous point on the same streamline, and then using the convective relations (4.25) and (4.26) to solve for the two quantities. This worked with some parameter regimes but not in others. When the rotational velocity was far greater than the main path velocity or the clearance was very small, convergence problems were experienced.

To overcome this problem, the equations of Γ and P convection were re-written in terms of the coordinates, s and θ. The equations of convection were then solved using the derivative in the s direction in the following manner:

$$u_s \frac{\partial \Gamma}{\partial s} + u_\theta \frac{1}{R} \frac{\partial \Gamma}{\partial \theta} = f(g_R, g_S) \tag{4.39}$$

where $f(g_R, g_S)$ is a function containing the shear terms of the convective equation 4.24. This relation is simply rewritten:

$$\frac{\partial \Gamma}{\partial s} = -\frac{u_\theta}{R u_s} \frac{\partial \Gamma}{\partial \theta} + \frac{1}{u_s} f(g_R, g_S) \tag{4.40}$$

$$\Gamma_{s+1} = \Gamma_s + \frac{\partial \Gamma}{\partial s} ds \tag{4.41}$$

A similar relation can be derived for the total pressure P. This method worked well in reproducing the data obtained in at least one early trial with streamline convection. An inspection of equation (4.40) reveals a diffusion equation in the s direction with a characteristic velocity given by $u_\theta/(Ru_s)$. Convergence for this type of formulation then depends upon a path step chosen so that the Courant condition (Press *et al.* , 1992) is not violated. In this particular case:

$$DS \leq DT * (\frac{Ru_s}{u_\theta}) \tag{4.42}$$

Using the input data for the conical shroud with inlet swirl = .5, ϕ = .06, and JT =

10, this condition indicates that $JS \geq 45$.

Examining a sample calculation with this method, for the conical leakage path with $\phi = 0.06$ and inlet swirl = 0.5, figure 4.3 showed the flow parameters, Γ, u_s, u_θ and p as functions of the mesh location for a 50x10 grid size. In this figure, the whirl frequency ratio is 0.3. The static pressure decreases while the two velocity components steadily increase in the path direction. The velocity increase is similar to experimental observations (Sivo *et al.* , 1994b), while the static pressure drop has also been measured (Guinzburg, 1992). The vorticity also increases in the path direction, and a noticable region of high vorticity is seen in the plot.

A grid size check was also carried out to ensure that the program was attaining good resolution and that the program was stable with respect to mesh sizing. Figure 4.5 shows the rotordynamic forces as functions of whirl frequency for the conic shroud.

From the figure, the grid size seems to have a significant effect on the forces. The normal force predictions are similar for all grid sizes. A 30x5 grid appears to have problems with the tangential force at negative whirl frequency ratios, but this is not as important for the evaluation of stability. However, this will have a significant effect on the calculated rotordynamic coefficients. Some resolution may be lost by having only 5 increments in the θ direction. In this preliminary study, a grid size of 50x10 was selected for computational time and resolution considerations and is used in most of the reported calculations. However, as there are only 10 increments in the circumferential direction, the grid size should be expanded in the future to ensure adequate resolution of the flow field. Due to the similarity in the 60x10 and 50x10 cases, it appears as though the Courant condition is maintained. The method had convergence problems for whirl frequency ratios higher than $\Omega/\omega = .4$.

4.6 Discussion

In a detailed examination of the bulk flow model, evolutionary equations of the "effective" vorticity and total pressure can be derived. The relations seem to make intuitive sense, in that the vorticity and total pressure are conserved along stream-

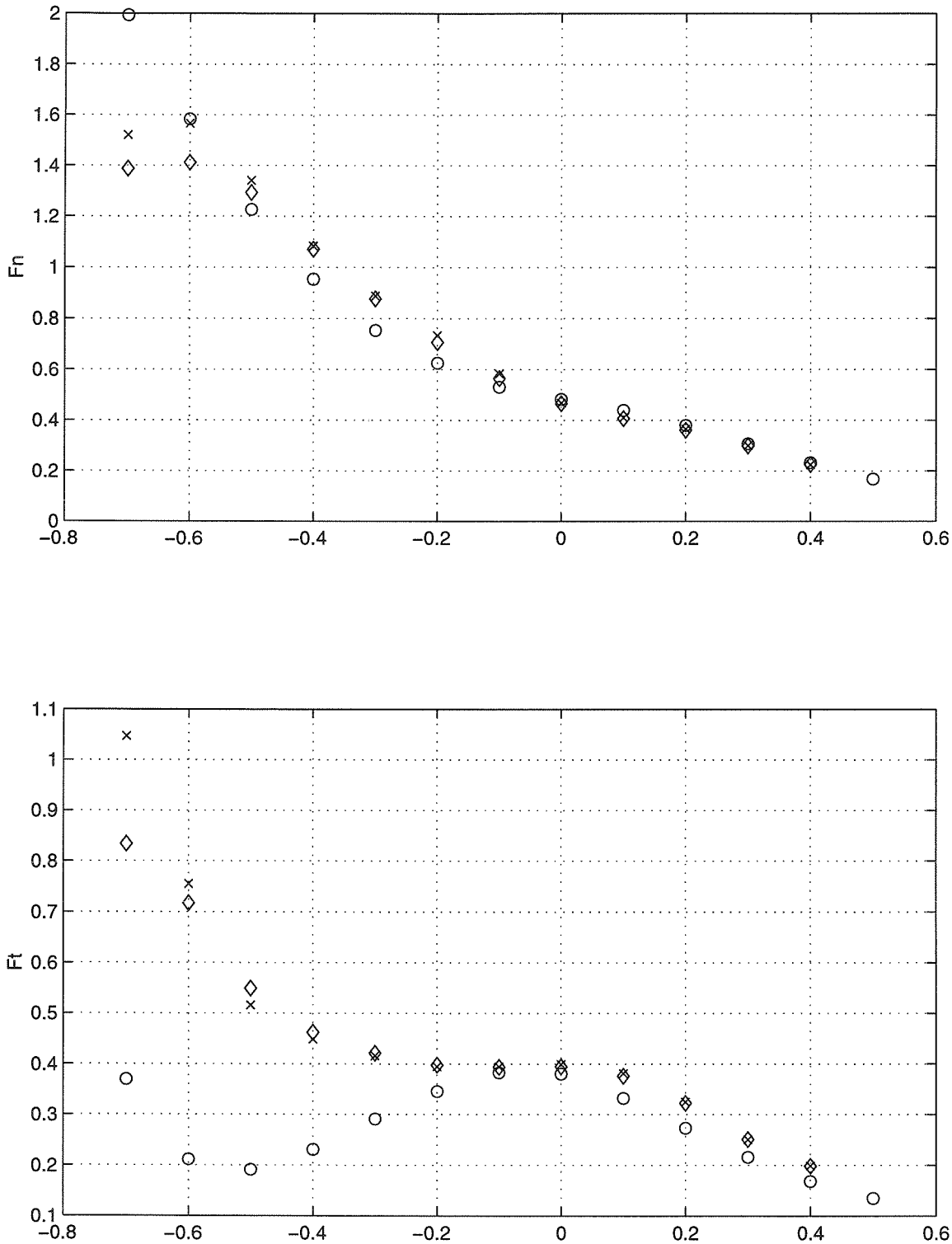

Figure 4.5: Plot of rotordynamic forces versus whirl frequency ratio Ω/ω for the conical leakage path. Results calculated using $\Lambda = .5$ and $\phi = .06$. $30\times5(\circ), 50\times10(\times)$ and $60 \times 10(\diamond)$.

lines in the absence of any dissipative phenomena. In Hir's and Childs' formulation, the only source of dissipation is wall friction. The evolutionary equations of vorticity and total pressure led to the consideration of an alternate means of solution for the bulk flow equations rather than Childs' perturbation method.

There are currently many options for this new method of solution. Uncertainties in the boundary conditions both at the inlet and discharge can play a major role in the determination of the rotordynamic forces. The two downstream boundary conditions appear to give very similar flow variables, but very different forces.

To satisfy the Courant condition, a large grid size is needed to acheive convergent results with this method. However, the use of a 50x10 grid in the calculations ensures that this condition is not violated at the most extreme case, where Ω/ω = -.7 (the largest denominator of equation (4.42)). As the whirl frequency ratio increases, the step size in the path direction becomes smaller than necessary, and at Ω/ω = .4, the condition becomes that $JS \geq 4$. As $JS = 50$ exceeds this by an order of magnitude, the calculations at forward whirl may be more reliable than at the negative whirl frequencies where the grid size is very close to the Courant condition. The selected grid size may also be more reliable as the flow coefficient increases. Despite these concerns, some success in predicting the forces for the conical leakage path and the straight seals, described in the next chapter, has been realized.

A very interesting feature of figure 4.3 is the plot of Γ, the effective vorticity. There appears to be a region of relatively higher vorticity in the domain, that grows as it proceeds downstream. Perhaps a more pronounced example can be seen in figure 4.6, for the same flow conditions but at a whirl frequency ratio Ω/ω = -.7.

From these calculations, areas of relatively high and low vorticity appear to form in the leakage path, and move downstream to the discharge. There appears to be no significant change in the velocities along the leakage path and it is not clear if this is a numerical instability with the method or a physical trait of the flow.

If the vorticity fluctuations are not a numerical instability, then it may be useful to consider the Taylor number. The Taylor number of this particular case, closely related to the Reynolds number based on rotational speed, is $Ta = 2.245 \times 10^7$ with

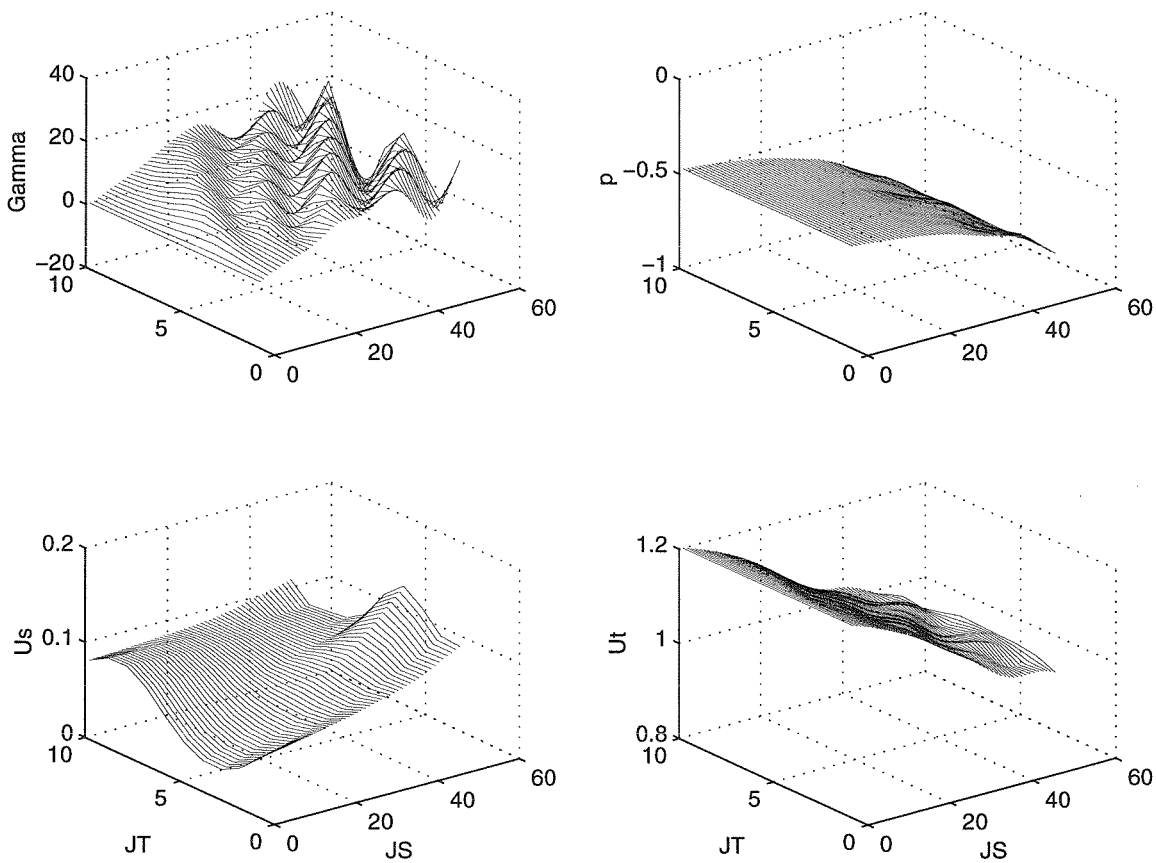

Figure 4.6: Plot of normalized flow variables against mesh location for the conical leakage path. Results using 50x10 grid size, a whirl ratio Ω/ω = -.7 and ϕ = .06.

this number defined as:

$$Ta = R_2(H)^3 \frac{\omega^2}{\nu^2} \tag{4.43}$$

The typical value given for the transition to turbulence in a Taylor Couette flow is $Ta \approx 160000$, but some work examines the flow field at $17000 < Re_\omega < 120000$ and $8 \times 10^7 < Ta < 4 \times 10^9$ (Townsend, 1984). Townsend noted the presence of large toroidal eddies at $Re_\omega < 30000$, and helical eddies for values of the of the Reynolds number above that in the flow between concentric cylinders. The experiments used an axial flow of about 1% of the rotational velocity. Considering the case of the leakage path, a flow coefficient $\phi = .06$ implies an axial flow of the same order of magnitude as Townsend's experiments, and $Re_\omega = 27370$. However, it seems highly unlikely that a two-dimensional model can capture the complex flow patterns associated with this experimental observation.

Another interesting result of considering the Taylor number of these flows is the critical value of this number at $Ta \approx 1700$ (Bjorklund & Kays, 1959). This critical Taylor number denotes the transition region from laminar flow to Taylor vortex flow, and hence different mechanisms of momentum and heat transfer. Above the critical Taylor number, the momentum transfer occurs in sublayers close to the surface, and this may give some insight into the effect the wall friction has on the rotordynamic forces, which will be quantified in section 5.3.2 of the next chapter. While some experimental evidence from Sivo (1994) shows path velocity reversal that may indicate this type of rotating vortex pattern in the leakage path, the reversal is usually isolated near the inlet of the leakage path, and so it is not clear if this wavy vorticity pattern is in error.

The pressure drop in this new calculation is also at substantial odds with experimental observations. As the integration of the static pressure is used to deduce the unsteady forces, any small error may lead to large deviations in the calculated forces. The losses due to the low pressure seal and the inlet to the leakage path should be accounted for if accurate force calculations are expected.

Chapter 5 Numerical Results

5.1 Comparison of Bulk Flow Models

The two solutions of the bulk flow equations, Childs' method and the current stream function/vorticity solution, were examined for consistency.

Childs' perturbation method has been programmed previously (Guinzburg, 1992) and has been validated. With the β term modification in the circumferential momentum equation (see section 4.2.1), results which were well suited to polynomial fits were obtained, and therefore the data from this code in this chapter is presented in the compact form of the rotordynamic force coefficients.

Code validation for the new solution was not satisfactorily acheived. This is due to the observation that certain geometries lent themselves to various means of solution, as outlined for the different boundary conditions in the previous chapter. As a result, only a collection of working cases can be presented rather than an established solution procedure for solving the bulk flow equations using the stream function/vorticity formulation. For the complex geometry of the pump leakage path, results were obtained from the SV method which qualitatively agree with experimental observations. As no resonances were observed, these results are also presented in the form of the rotordynamic force coefficients for ease of comparison.

The simple problem of the straight seal has proven to be difficult for the new model, and convergence using the SV method has occured only for a few conditions. It was felt that the simpler geometry would provide a much better means of validation for this new code, given the amount of data in the literature. However, only partial results are available.

5.2 Comparison of Modified Childs' Model to Experiments

The experimental data presented in Chapter 3 are compared with the results using Childs' bulk-flow model, with appropriate modifications of the β terms for elimination of the force "resonances". This arbitrary modification serves as a reminder that there are limitations to this perturbation model, which prevent it from being a reliable tool in the intial design of pump leakage path annuli. In the data presented, n_S = .13 and n_R = .08 were used as they seemed to offer the best comparison between the calculated forces and experimental data.. The values ms = -0.25 and mr = -0.25 were retained as they correspond to a fully developed turbulent flow in the pipe correlations.

5.2.1 Path Geometries

Figure 5.1 shows the rotordynamic force coefficients versus flow coefficient generated by Childs' model for the conical, contoured and short contoured geometries. These should be compared with the force coefficients of Figure 3.3.

The direct stiffness, K, trend appears to be opposite from what was observed experimentally. In the computations it increases with increasing flow coefficient for all three cases. The cross-coupled stiffness, k, appears to follow the same trend as the experiments, and matches closely in magnitude for the conical and contoured rotor. The direct damping is also fairly close in magnitude to the experimental results for two longer paths. Cross-coupled damping appears to differ slightly in magnitude for all three cases. Direct added mass is underpredicted by the model. The whirl ratio k/C is overpredicted for the contoured rotor, but not too badly estimated for the conic path and the short contoured path. The model appears to greatly underpredict the magnitude of the forces for the short contoured rotor. Thus, the predicted forces of the short contoured path are smaller in magnitude than those of the other rotors, but not all trends and magnitudes match the experimental data.

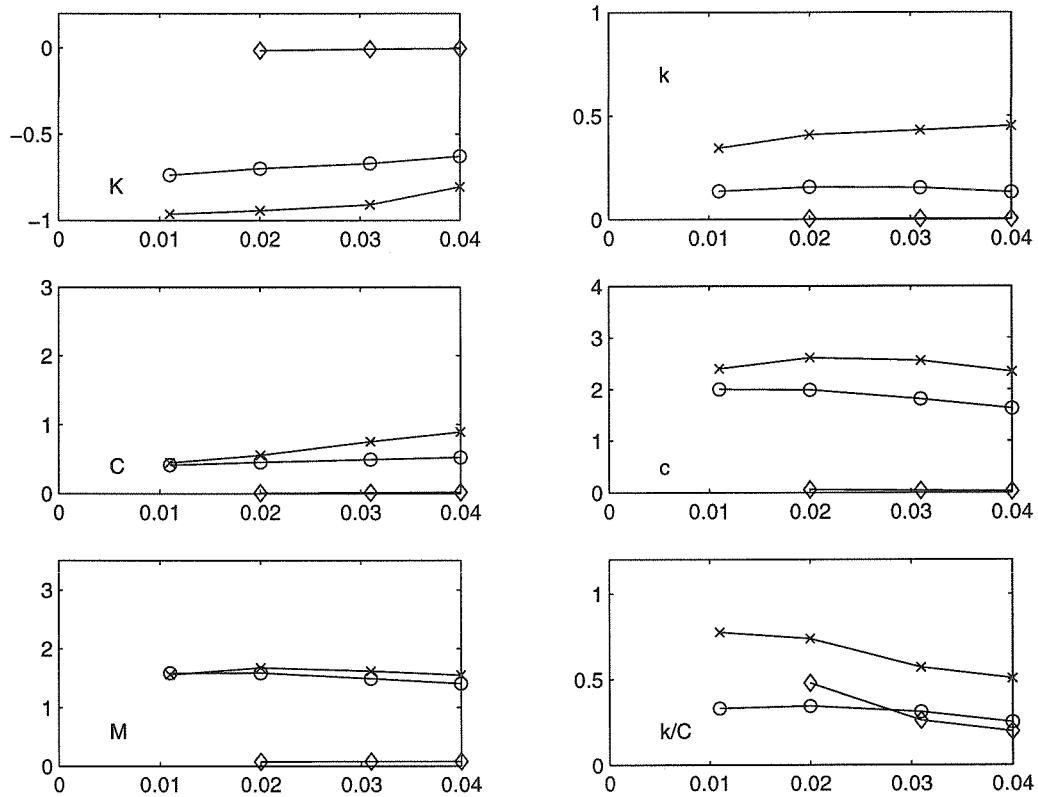

Figure 5.1: Calculated rotordynamic force coefficients versus flow coefficient ϕ for the conic (o), contoured ($\times$), and short contoured ($\diamond$) shrouds.

5.2.2 Seals

Figure 5.2 shows the rotordynamic force coefficients versus flow coefficient for the leakage path geometry which consists of a low pressure axial clearance and radial clearance seal. A comparison with Figure 3.4 reveals some similarities. The increase in the magnitude of the tangential force coefficients for the case with the radial clearance seal is observed in the calculation, as well as the increase in the stiffness, but the magnitudes are poorly predicted.

The direct stiffness in the experiments showed a "Lomakin" effect in which the impeller with the radial clearance seal demonstrated a increasing direct stiffness with flow coefficient. This also appears to be the case in the calculations, as the direct stiffness increases as the flow coefficient is increased. However, this increase is much

smaller in the model than that observed experimentally, and for the axial clearance seal, the magnitude of K is too small and the trend with flow coefficient opposite to that of the experiments.

The variations between the two leakage paths for the cross-coupled stiffness and the direct damping are also similar in the computations. The magnitude of both rotordynamic coefficients is much higher for the radial clearance case, and increase relatively faster with increasing flow coefficient. The magnitudes of the calculated cross-coupled stiffness and direct damping are slightly smaller than the measured values.

The cross-coupled damping seems to match the experimental data well in both trend and magnitude. The trend of the added mass with flow coefficient is also very similar to the measured values, but smaller in magnitude. The whirl ratio appears to be overpredicted in the case of the axial clearance seal, seemingly due to the underpredicted magnitude of the direct damping for this case.

Figure 5.3 shows rotordynamic force coefficients versus flow coefficient for a conical geometry with a high pressure orifice and without. This can be compared with figure 3.5. In the experimental case, the size of the radial gap formed by the high pressure orifice was .0508 *cm*. A computational case proved unstable if this detailed geometry of the inlet was used as an input. Therefore, the results for the case with an orifice were calculated by increasing the inlet loss coefficient in the program until the magnitudes of the forces matched closely. It is interesting to note the similarities between these calculations and those for the low pressure seal. The same increase in the tangential force coefficients is observed, but there is not much variation in the normal force coefficients.

For the direct stiffness, the cross-coupled damping, and the direct added mass, all the calculations show only small variations between the case with no orifice and the case with a large inlet loss coefficient (simulated orifice). The cross-coupled and direct added mass are underpredicted compared with the measured values, and the direct stiffness is overpredicted.

The effect of increasing the inlet loss in the calculation is an increase in the

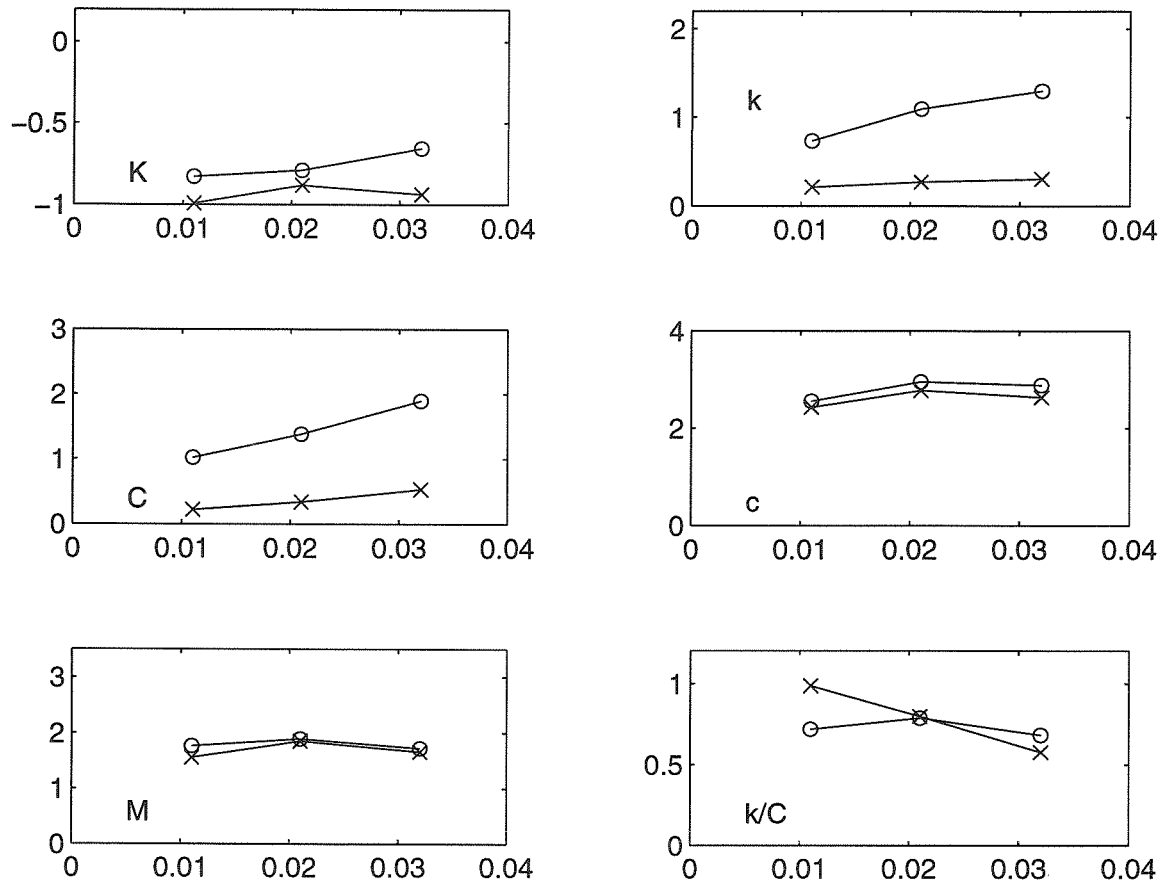

Figure 5.2: Calculated rotordynamic force coefficients plotted against flow coefficient ϕ for radial ($\circ$) clearance and axial ($\times$) clearance low pressure seal.

tangential force coefficients as the flow rate increases. These results are quite similar to the effect observed in the axial and radial clearance low pressure seals. While the relative behavior is similar to the experiments, the magnitudes of the computed orifice are much smaller, and the trends of C and k for the case with no orifice are opposite. This leads to a whirl ratio which shows opposite behavior from that seen in meaurements for both high pressure seal geometries.

5.2.3 Inlet Swirl

Figure 5.4 shows the rotordynamic force coefficients versus the flow coefficient for various inlet swirl ratios, Λ, in the contoured leakage path. The figure can be compared

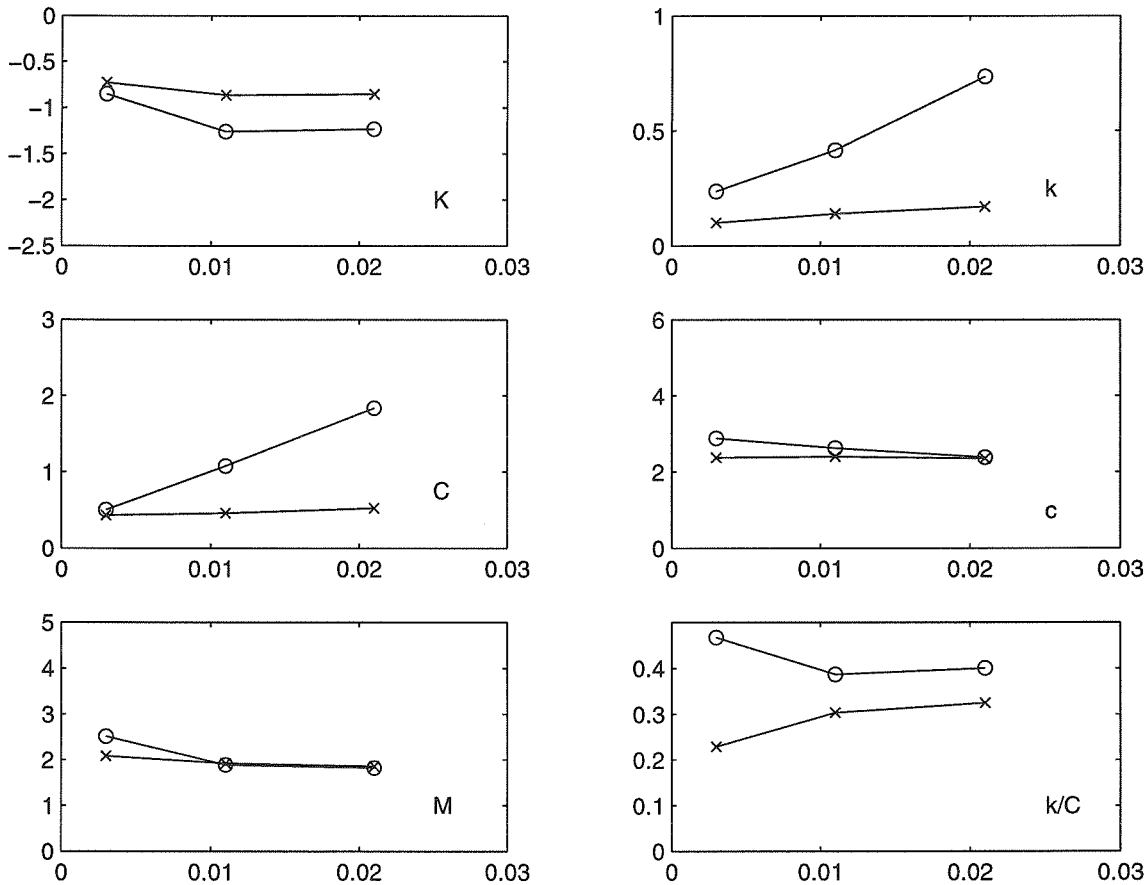

Figure 5.3: Calculated rotordynamic force coefficients versus flow coefficient ϕ for the high pressure orifice, conical geometry. Simulated (high inlet loss) (o) and no ($\times$) orifice.

to the experimentally determined force coefficients in figure 3.6. The experiments showed that the variation of the forces with increasing flow coefficient for different values of inlet swirl was not significant. This also appears to be the case with the computational results. However, some discrepancies with trend and magnitude exist, and they are particularly noticable in the whirl ratio.

For the case with and without inlet swirl, the direct stiffness of the computations appears to match both trend of the experimental results well, but seems to be off by a factor of two in the magnitude. The cross-coupled damping for the calculations appears to match the measured values well in trend and magnitude. As in previous calculations with Childs' model, the direct added mass is again underpredicted for all

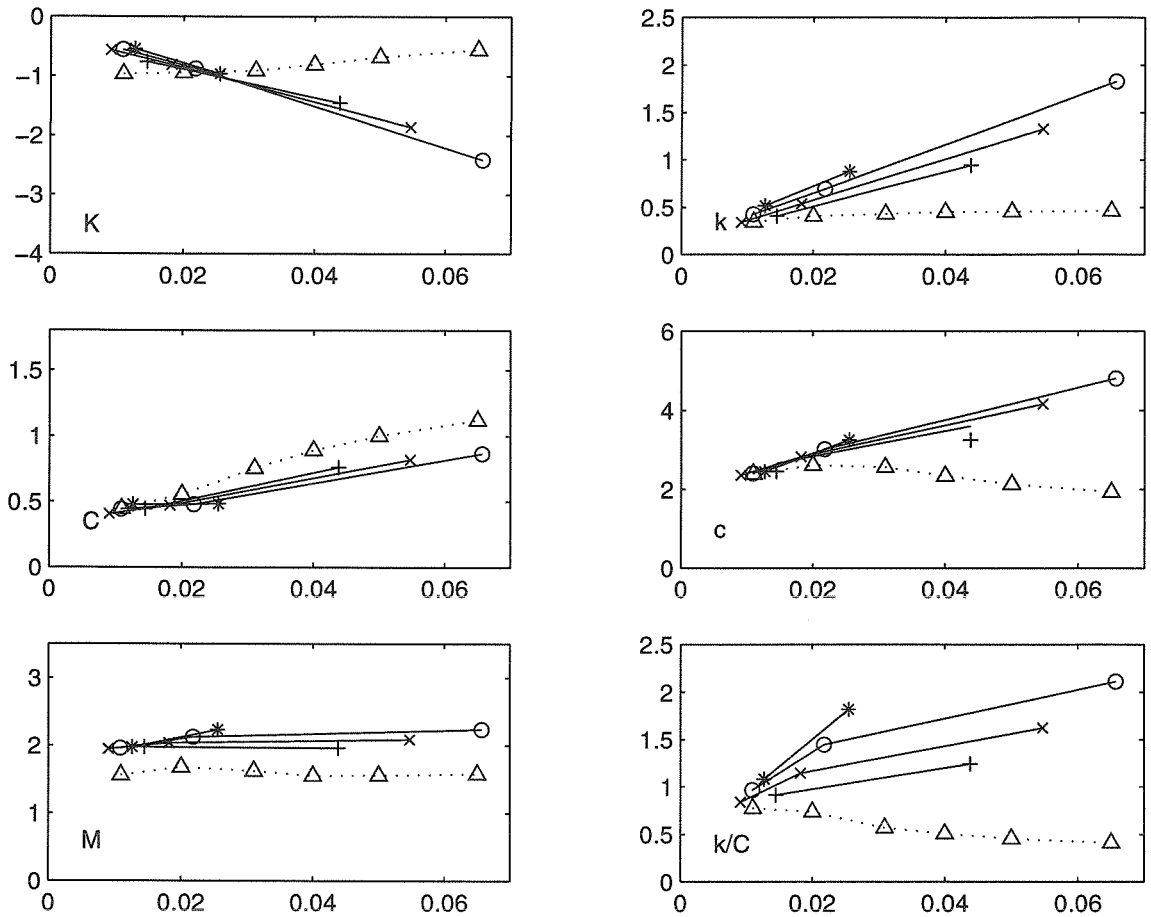

Figure 5.4: Calculated rotordynamic coefficients plotted against flow coefficient ϕ for tests with inlet swirl, $\Lambda = 0.4$ (+), 0.5 ($\times$), 0.6 (o), and 0.7 ($*$), and tests with no swirl, $\Lambda = 0$ ($\triangle$).

the swirl and no swirl cases.

For the force coefficients of the tangential force, the direct damping and cross-coupled stiffness, a steady increase with increasing flow coefficient is calculated for the cases with swirl. This is in contrast to the experiments in which an increase and then decrease was observed. The same observation can be reached for the direct damping of the case with no swirl, however, the model appears to predict the cross-coupled stiffness satisfactorily. In computations with and without swirl, these discrepancies in the tangential force coefficients lead to rather poor predictions of the experiments and an overprediction of the whirl ratio.

In summary, Childs' model can duplicate some of the rotordynamic behavior observed in experimental leakage path studies. Some of the incremental changes observed in cases with and without inlet swirl, with an axial and radial clearance low pressure seal, and even with the different leakage paths are similar to the incremental changes observed in experimental measurements. However, magnitude discrepancies and some incorrect trends seem to make this model less than reliable. Also, there is no obvious way to account for the anti-swirl measures such as ribs and grooves, given the assumption of a harmonic distribution of clearance in the circumferential direction.

5.3 Comparison of SV Model to Experiments

Due to the discrepancies in Childs' model, as seen in the comparison with the experiments in the preceding section, the finite difference model was developed in the hopes that some of the flow phenomenon such as reversals and seperation, documented experimentally by Sivo (1994) and computationally by Baskharone (1993), could be accounted for and thus decrease some of the discrepancies encountered in the previous section. Also, a way to model the changes in the clearance in the circumferential direction, such as anti-swirl ribs and grooves, would add to the capabilities of the bulk flow approach.

To investigate the behavior of this new bulk flow solution, a number of basic physical effects expected from experimental tests of the conical impeller were studied. These included examining the effects of the flow coefficient, the viscous shear stresses and the leakage path clearance. The results presented use a constant pressure downstream boundary condition. Only the simple geometry of the conical leakage path has been considered. Also, rather than attempting to fit the data with the empirical coefficients for the shear stresses, the coefficients n_S and n_R were held to the constant values of 0.079 given by Yamada, to simplify the analysis.

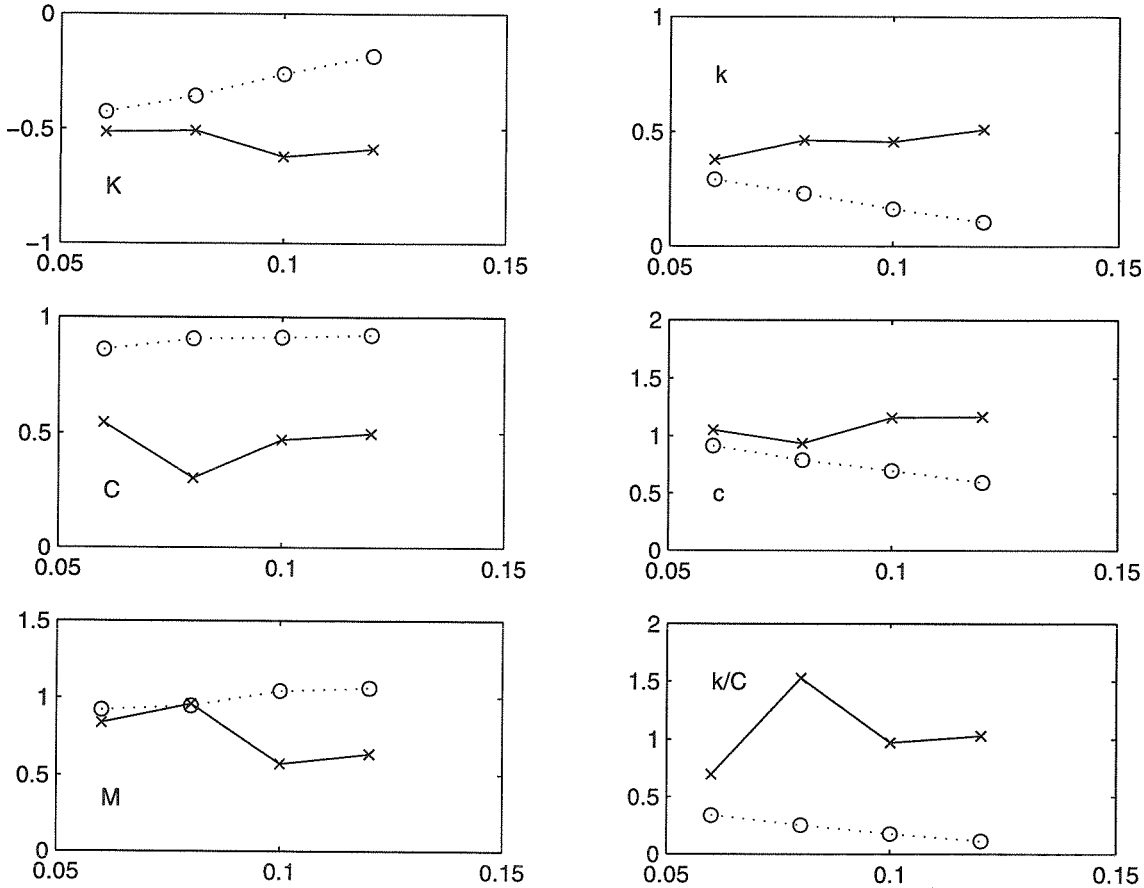

Figure 5.5: Calculated rotordynamic coefficients plotted against flow coefficient ϕ for conical shroud. Childs' perturbation model (dotted line), SV model (solid line).

5.3.1 Effect of Leakage Flow Coefficient

Increasing the leakage flow coefficient in the experimental tests of conical shroud geometry with a face seal has produced effects which have been well documented. Perhaps the most obvious is the decrease in the direct stiffness. For the conical shroud, an increase in leakage flow coefficient has also been accompanied by a decrease in the whirl ratio, k/C.

Figure 5.5 shows the effect of changing the leakage flow coefficient over a range from 0.06 to 0.12 for the conical rotor at 1000 *rpm* with a clearance of $H/R_2 = .03$. Childs' perturbation model results are plotted with the SV prediction for comparison.

Good agreement is observed between the two methods in the rotordynamic coefficients of the normal force for values of the leakage flow coefficient that are less

than about .08. For values of flow rate higher than that, the two predictions of the direct mass, cross-coupled damping and direct stiffness seem to differ in trend and in magnitude. Child's model actually shows an increasing direct stiffness, which is at odds with experimental observations, while the SV model appears to predict a relatively constant trend with flow rate. The trends of the cross-coupled damping with increased flow coefficient appear to be opposite of each other, and the SV model predicts a drop in the direct added mass.

The tangential force coefficients are also inconsistent between the two models. For the cross-coupled stiffness, opposite trends with increasing flow rate are computed. For the direct damping, a large magnitude difference is apparent between Childs' and the SV model, leading to a whirl ratio, k/C which is overpredicted for the SV model.

5.3.2 Effect of the Viscous Shear Stresses

The effect of the shear stress terms in the bulk flow model has been observed to be fairly small for certain geometries (Tsujimoto *et al.* , 1997), and analysis of the Taylor number in the previous chapter showed that the effects of the wall shear should be isolated to sublayers very close to the wall.

The effect of wall shear on the forces for the conical leakage path with $H/R_2 = .03$, $\phi = .06$, and 1000 *rpm* are examined in figure 5.6. The shear factors, n_S and n_R, are varied from 0.0 to 0.079. Experimental data is also plotted.

As can be seen in the figure, there is very little variation of the normal force predictions with and without shear. The method seems to underestimate the experimental values of the normal force at negative whirl frequencies. However, for rotordynamic stability, only the forward whirl frequencies need to be considered, and the normal force prediction appears to be of similar magnitude to the experiments but the direct stiffness will be underestimated by the calculation. The tangential force shows a greater variation with different shear factors. The higher shear factors show good agreement with the experimental tangential force at negative whirl frequency ratios, however, the forward whirl frequency ratios are of greater interest, and none of the

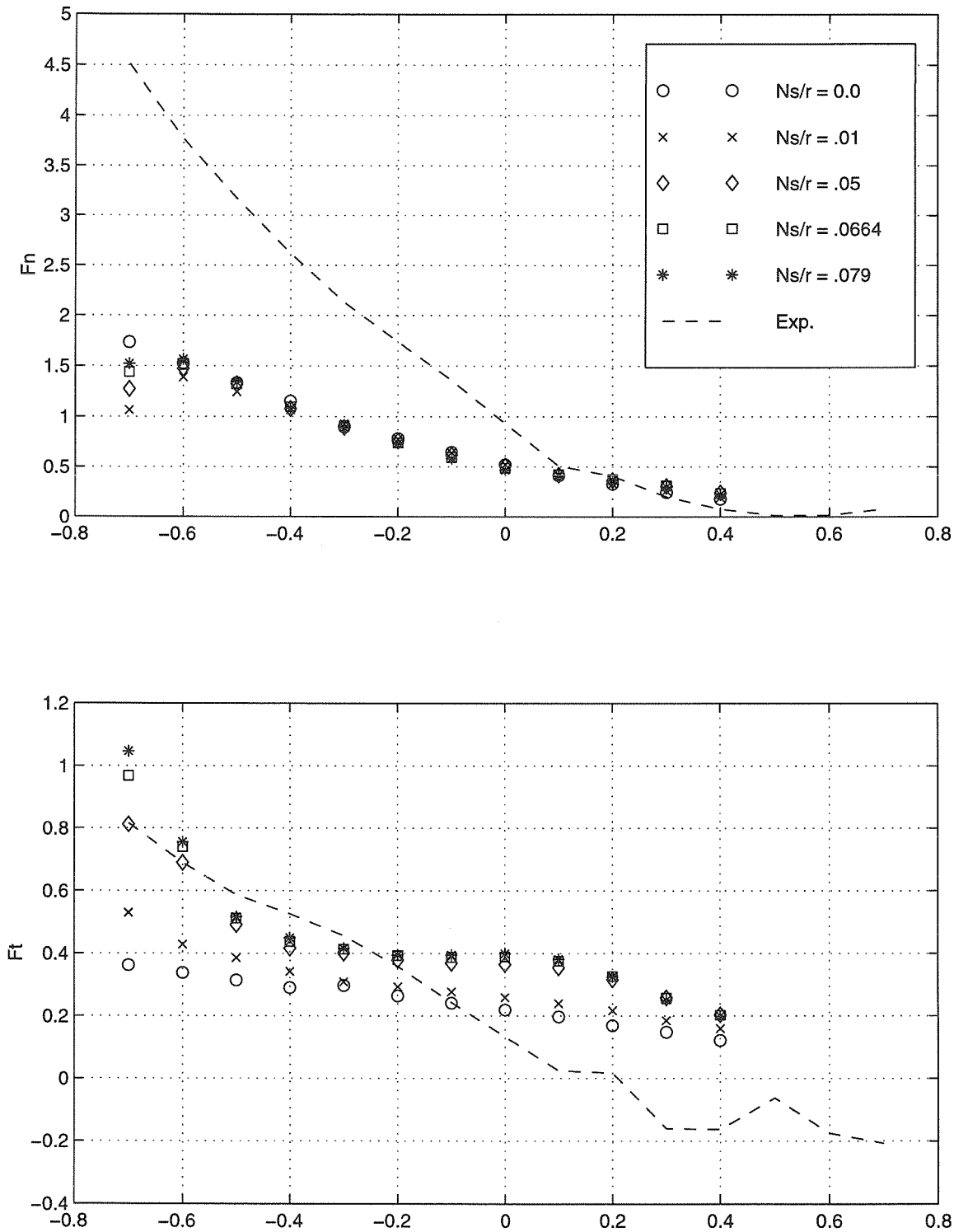

Figure 5.6: Plot of rotordynamic forces as functions of the whirl frequency Ω/ω for the conical leakage path, $\phi = .06$. Results for 50x10 grid with indicated shear factors.

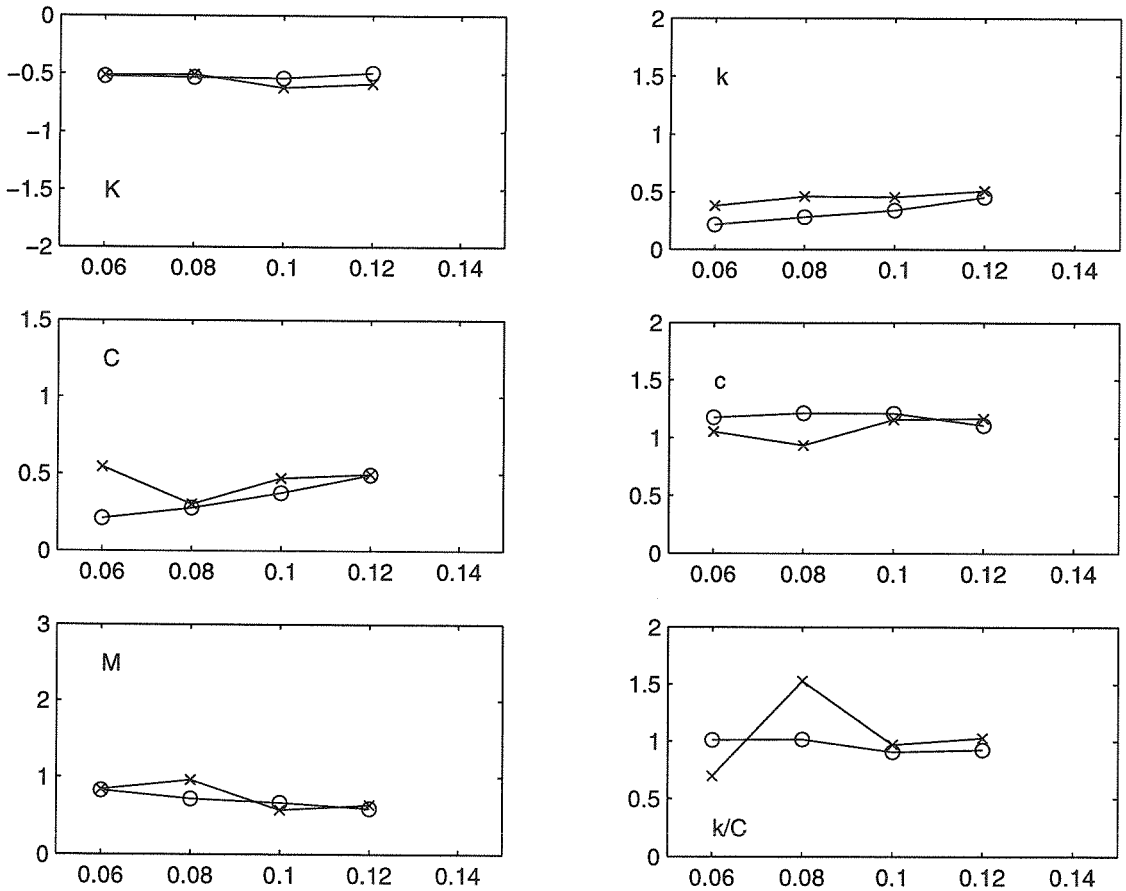

Figure 5.7: Calculated rotordynamic force coefficients versus flow coefficient, ϕ for the conical leakage path, with ($\times$) and without ($\circ$) viscous shear.

shear factors correctly predicts the stability.

This insensitivity of the normal force and the variation of the tangential force to the wall shear is manifested through the curve fitting. Figure 5.7 shows the force coefficients as functions of the flow coefficient for the conical leakage path both with and without shear ($n_S, n_R = 0.079$). Despite the variations noted in the test case, figure 5.6, there is only a small effect on these force coefficients due to the viscous shears. There appears to be very little variation of the normal force coefficients with the flow rate, as noted in the previously. The whirl ratio seems to be affected by the differences in the direct damping.

5.3.3 Effect of Inlet Swirl

The effect of inlet swirl has been documented in Chapter 3. The experiments showed that the amount of inlet swirl did not affect the force coefficients.

The inlet swirl ratio Λ, has some effect on the calculated forces in the SV model, in particular the magnitude of both unsteady forces is increased for the case of the conical leakage path. It appears as though the minimum of the normal and tangential force shift to larger values of positive whirl frequency, resulting in a much larger forces at any given whirl frequency ratio of interest. Figure 5.8 shows the effect of inlet swirl on the conical leakage path with a flow coefficient of $\phi = .06$. In this case, the shear stresses are zeroed, so the forces are for an inviscid case.

Experimental results discussed in Chapter 3 indicated no effects on the rotordynamics due to inlet swirl, but this is clearly not the case with this formulation of the bulk flow model. A constant inlet swirl condition, $\Lambda = .5$, is used for most of the results presented in this research.

5.3.4 Effect of Clearance

Using the SV model, the unsteady forces in the leakage path have been observed to increase as the leakage path clearance decreased. This is in agreement with experimental results (Guinzburg, 1992)(See figure 1.2). The amount of the increase appears to scale as $1/H$.

Figure 5.9 shows the rotordynamic force coefficients versus the flow coefficient for different values of the leakage path clearance. The relative magnitude of the forces is consistent with the experimental observations: as the clearance gets smaller the forces are larger.

The same trends with flow rate as noted previously are again observed. The tangential force coefficients increase as the flow rate increases, and the normal force coefficients appear to be constant functions of the flow rate. The magnitudes of the force coefficients also increase with decreasing clearance, except for the direct stiffness which decreases with decreasing clearance. The magnitude change appears to be

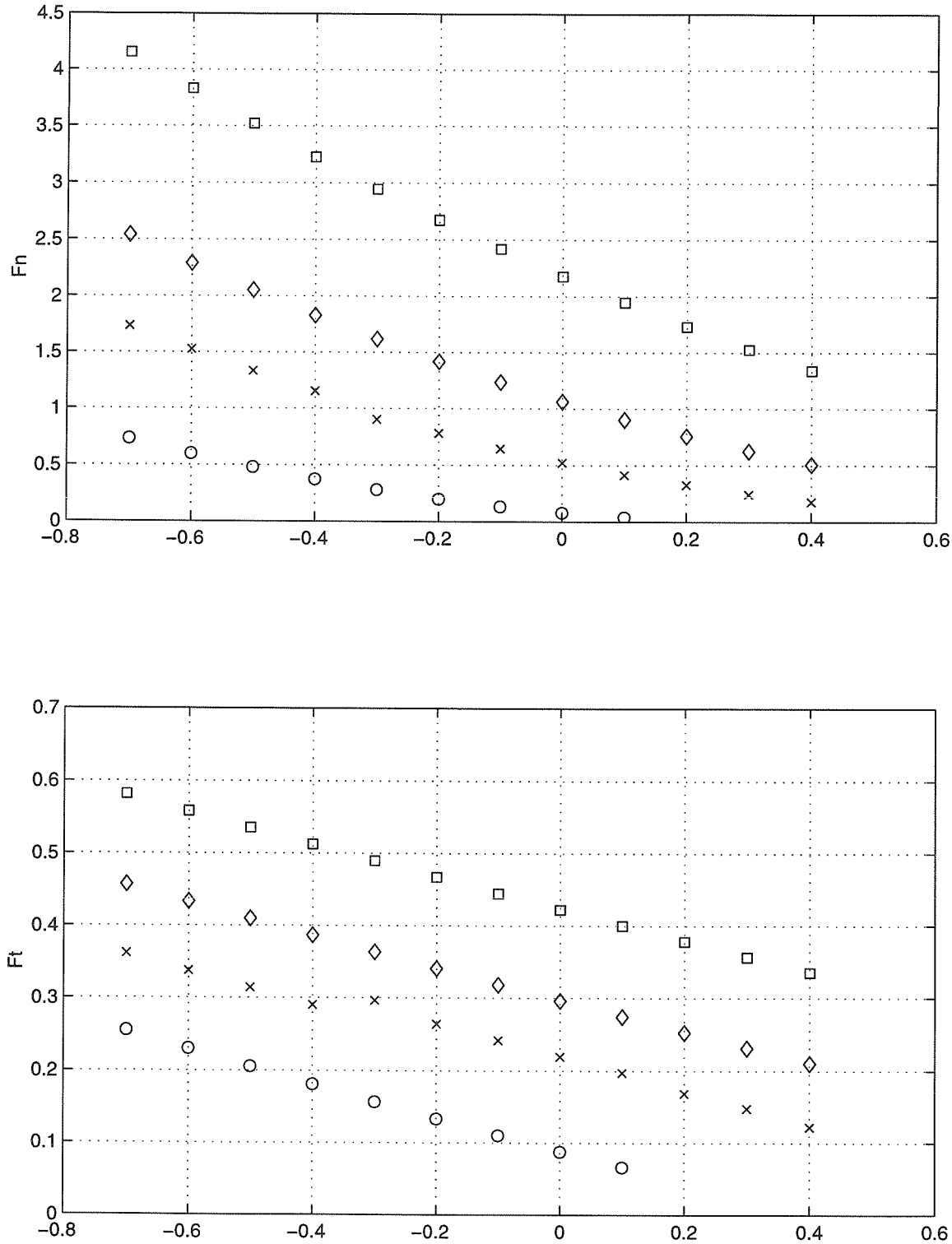

Figure 5.8: Plot of rotordynamic forces as functions of the whirl frequency Ω/ω for the conical leakage path. Results calculated using 50x10 grid size with no shear, $\phi =$ .06. $\Lambda = 0.2$ ($\circ$), 0.5 ($\times$), 0.7 ($\diamond$) and 1.0 ($\square$).

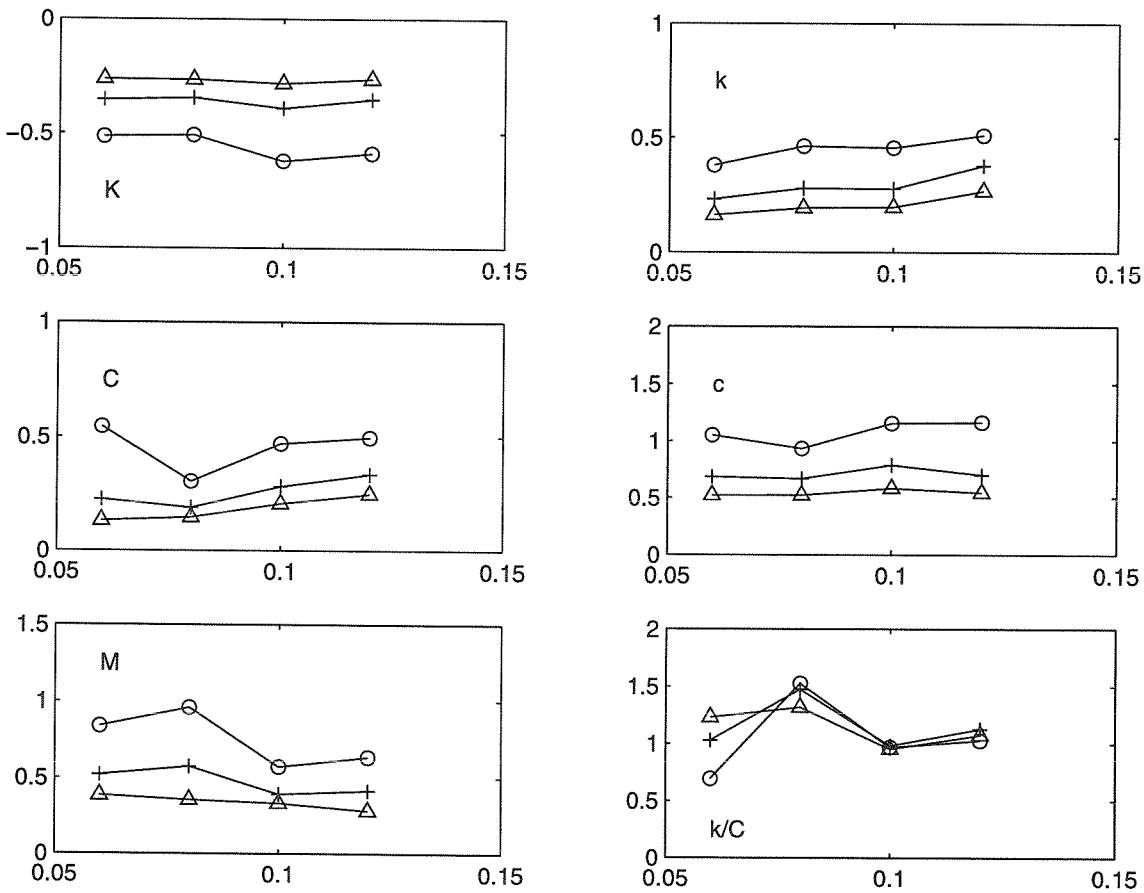

Figure 5.9: Calculated rotordynamic force coefficients versus flow coefficient ϕ for the conical leakage path. $H/R_2 = 0.03$ ($\circ$), 0.045 ($+$), and 0.06 ($\triangle$).

porportional to $1/H$ which has been observed experimentally (Guinzburg, 1992).

5.3.5 Path Geometry

Finally, the effect of path geometry was examined for the new SV formulation. A shorter length impeller was studied, however without the effects of curvature. Using an eye to tip diameter ratio of .700 similar to the experimental short contoured impeller, and using the same axial length to diameter ratio, .088, a conic leakage path 73.6° to the axis of rotation is formed. Again, no curvature effects are included, but as little variation between the contoured and conic leakage path was observed experimentally, this model may be expected to produce similar results, and that is the case.

Figure 5.10 shows SV calculated rotordynamic force coefficients as functions of the flow coefficient for the short conical path and the normal conical path. Some of the same general trends are observed for this comparison that are observed in Childs' model of the paths and the experimental data.

Again, the force coefficients of the normal force appear to be constant functions of the flow rate. The normal force of the shorter length path is much smaller in magnitude than that of the regular length path, in good agreement with prior calculations and experiments. The tangential force coefficients increase with increasing flow rate, typical of SV calculations, and the shorter axial length yields a smaller magnitude tangential force. The same problems of not being able to duplicate experimentally determined trends and magnitudes is again a significant shortcoming of this solution.

5.4 Straight Seals

The case of straight smooth seals was considered as an ideal case to validate the current solution methodology. Numerous experimental and computational results are available in the literature for comparison. However, much difficulty was experienced with the current set of downstream boundary conditions. In some very random cases, convergence could be acheived using a constant pressure boundary condition, but

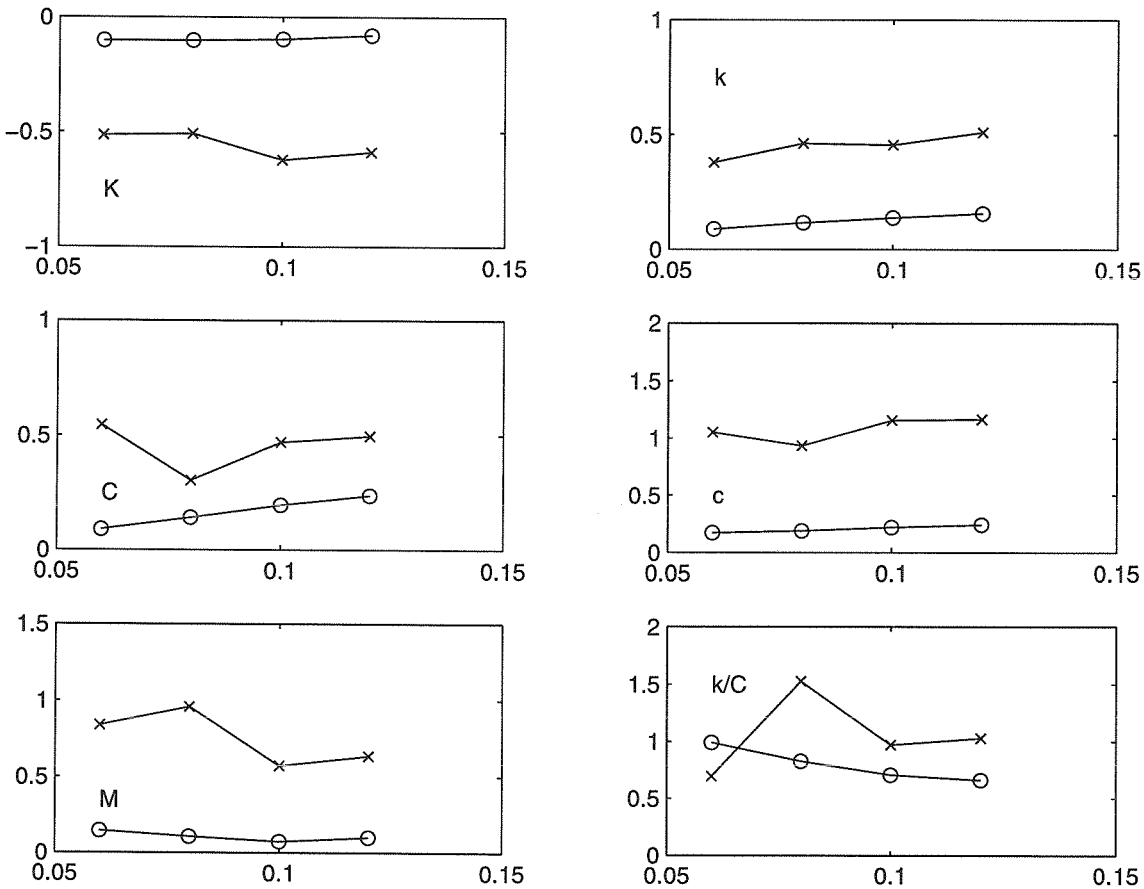

Figure 5.10: Calculated rotordynamic force coefficients versus flow coefficient ϕ for the conical leakage paths. Short axial length ($\circ$) and normal axial length ($\times$).

these cases were almost always very unstable with respect to small changes in parameters like the frictional factors and relaxation factors. The Appendix B contains details of a different approach to the downstream boundary condition that appears to give fairly accurate results.

5.5 Discussion

Both Childs' perturbation solution and the stream function/vorticity method have difficulties in predicting the unsteady forces in discharge-to-suction leakage flows in centrifugal pumps. With the added drawback of assumed harmonic forms for the leakage path clearance in Childs' model, the SV method was devised as a solution of the bulk flow equations with fewer restrictions.

The SV method appears to predict some trends of rotordynamic flows. In particular, the effect of clearance and the effect of a shorter axial length path show the same relative trends in computations and experiments. The near constant behavior of the normal force with flow coefficient is a problem needing further examination.

Another area which should be investigated further is the effect of the Courant condition on the convection calculations. In the case of the shorter axial length path, figure 5.10, the decreased path length makes the 50x10 grid have at least twice the required number of increments in the path direction. The force coefficients appear to be smoother functions of the flow rate. Any such change for the normal length path would result in considerably longer calculations, but may be beneficial for the force predictions.

Chapter 6 Conclusions

The rotordynamic forces generated by fluid structure interaction in annuli have been examined both experimentally and computationally. The current work further elaborates efforts by previous researchers to quantify and predict the contribution of impeller shroud forces to the rotordynamic stability of pumping machinery.

Experimental data from the current research shows good agreement with the work of previous researchers. More typical pump shroud geometries were examined and the effect of curvature on the leakage path appears to be fairly small in the case with no inlet swirl of the fluid. A shorter axial length and larger eye-to-tip ratio makes the measured forces decrease. The effect of the low pressure and high pressure seals can be very significant, and can be stabilizing or destabilizing depending on the design. Inlet swirl was again found to increase the instability of the rotordynamic forces, but the amount of non-zero pre-rotation did not seem to affect the measurements significantly. The effect of curvature of the leakage path when inlet swirl was present had a signficant effect on the force which drives the whirl motion. Efforts to reduce the swirl velocity of the incoming fluid displayed some success at reducing the rotordynamic forces. Disrupting the rotation of the fluid half-way along the passage seemed to offer different benefits to anti-swirl measures at the tip or running the full length of the path.

The bulk flow model was examined. Childs' perturbation solution was modified to reduce the abrupt force fluctuations which appeared in previous work. This modified perturbation model is capable of predicting some of the observed experimental trends of the rotordynamic forces. But some magnitude and trend discrepancies seem to indicate that further modifications are necessary before the perturbation solution can reliably predict the forces in the complex geometry of a pump leakage path.

The basic equations of the bulk flow model were recast into evolutionary equations for the vorticity and total pressure. A solution procedure was then developed

which avoided both linearization with eccentricity and assumed harmonic forms of the flow variables. Some convergent results have been obtained, and the results seem qualitatively similar to experimental measurements.

References

ADKINS, D., & BRENNEN, C. 1988. Analysis of Hydrodynamic Radial Forces on Centrifugal Pump Impellers. *ASME J. of Fluids Engineering*, **110**(1), 20–28.

BASKHARONE, E., & HENSEL, S. 1991a. A Finite Element Perturbation Approach to Fluid/Rotor Interaction in Turbomachinery Elements: Part I. *ASME J. Fluids Eng.*, **113**, 353–361.

BASKHARONE, E., & HENSEL, S. 1991b. A Finite Element Perturbation Approach to Fluid/Rotor Interaction in Turbomachinery Elements: Part II. *ASME J. Fluids Eng.*, **113**, 362–367.

BASKHARONE, E., & HENSEL, S. 1993. Flow Field in the Secondary, Seal-Containing Passages of Centrifugal Pumps. *ASME J. Fluids Eng.*, **115**, 702–709.

BASKHARONE, E., DANIEL, A., & HENSEL, S. 1994. Rotordynamic Effects of the Shroud-to-Housing Leakage Flow in Centrifugal Pumps. *ASME J. Fluids Eng.*, **116**, 558–563.

BJORKLUND, I., & KAYS, W. 1959. Heat Transfer Between Concentric Rotating Cylinders. *ASME J. Heat Transfer*, **81**, 175–500.

BLACK, H. F., & JENSEN, D. N. 1970. Dynamic Hybrid Properties of Annular Pressure Seals. *Proc. J. Mech. Eng.*, **184**, 92–100.

BLACK, H.F. 1969. Effects of Hydraulic Forces in Annular Pressure Seals on the Vibrations of Centrifugal Pump Rotor. *J. Mech. Eng. Sci.*, **11**, 206–213.

BOLLETER, U., WYSS, A., WELTE, I., & STURCHLER, R. 1987. Measurement of Hydraulic Interaction Matricies of Boiler Feed Pump Impellers. *ASME J. of Vibration, Acoustics Stress and Reliability in Design*, **109**, 144–151.

BOLLETER, U., LEIBUNDGUT, E., STURCHLER, R., & MCCLOSKEY, T. 1989. Hydraulic Interaction and Excitation Forces of High Head Pump Impellers. *Pumping Machinery, 3rd Joint ASCE/ASME Mechanics Conference*, **81**, 187–193.

BRENNEN, C. E. 1994. *Hydrodynamics of Pumps.* Concepts ETI and Oxford University Press.

BRENNEN, C.E., & UY, R.V. 1998. Fluid Flow Equations for Rotordynamic Flows in Seals and Leakage Paths. *Proceedings of the 1998 International Symposium on Transport Phenomena and Dynamics of Rotating Machinery, ISROMAC-7*, **C**, 1139–1148.

CHILDS, D. W. 1983a. Dynamic Analysis of Turbulent Annular Seals Based on Hirs' Lubrication Equation. *ASME J. Lubr. Tech.*, **105**, 429–436.

CHILDS, D. W. 1983b. Finite Length Solutions for Rotordynamic Coefficients of Turbulent Annular Seals. *ASME J. Lubr. Tech.*, **105**, 437–445.

CHILDS, D. W. 1987. Fluid Structure Interaction Forces at Pump-Impeller-Shroud Surfaces for Rotordynamic Calculations. *ASME Symp. on Rotating Machinery Dynamics*, **2**, 581–593.

CHILDS, D. W. 1989. Fluid Structure Interaction Forces at Pump-Impeller-Shroud Surfaces for Rotordynamic Calculations. *ASME J. Vibration, Acoustics, Stress and Reliability in Design*, **111**, 216–225.

CHILDS, D. W., & DRESSMAN, J. B. 1982. Testing of Turbulent Seals for Rotordynamic Coefficients. *Proceedings of Workshop on Rotordynamic Instability Problems in High-Performance Turbomachinery, NASA Conf. Publ. 2250*, 157–171.

CHILDS, D. W., & DRESSMAN, J. B. 1985. Convergent-Tapered Annular Seals: Analysis and Testing for Rotordynamic Coefficients. *ASME J. Tribology*, **107**, 307–317.

CHILDS, D. W., & KIM, C. H. 1985. Analysis and Testing for Rotordynamic Coefficients of Turbulent Annular Seals with Different Directionally Homogeneous Surface Roughness Treatment for Rotor and Stator Elements. *ASME J. Tribology*, **107**, 296–306.

CHILDS, D. W., & SCHARRER, J. K. 1986. Experimental Rotordynamic Coefficient Results for Teeth-on-Rotor and Teeth-on-Stator Labyrinth Gas Seal. *Proc. Adv. Earth-to-Orbit Propulsion Tech. Conf., NASA Conf. Publ. 2436*, 327–345.

DIETZEN, F. J., & NORDMANN, R. 1987. Calculating Rotordynamic Coefficients of Seals by Finite-Difference Techniques. *ASME J. Tribology*, **109**, 388–394.

FRANZ, R. 1989. *Experimental Investigation of the Effect of Cavitation on the Rotordynamic Forces on a Whirling Centrifugal Pump Impeller.* Ph.D. thesis, California Institute of Technology.

FRITZ, R. J. 1970. The Affects of an Annular Fluid on the Vibrations of a Long Rotor. Part I—Theory and Part II—Test. *ASME J. Basic Eng.*, **92**, 923–937.

GUELICH, J., FLORJANCIC, D., & PACE, S. 1989. Influence of Flow Between Impeller and Casing on Part-Load Performance of Centrifugal Pumps. *Pumping Machinery, 3rd Joint ASCE/ASME Mechanics Conference*, **81**, 227–235.

GUINZBURG, A. 1992. *Rotordynamic Forces Generated by Discharge-to-Suction Leakage Flows in Centrifugal Pumps.* Ph.D. thesis, California Institute of Technology.

GUINZBURG, A., BRENNEN, C.E., ACOSTA, A.J., & CAUGHEY, T.K. 1993. The Effect of Inlet Swirl on the Rotordynamic Shroud Forces in a Centrifugal Pump. *ASME J. Eng. for Gas Turbines and Power*, **115**, 287–293.

GUINZBURG, A., BRENNEN, C.E., ACOSTA, A.J., & CAUGHEY, T.K. 1994. Experimental Results for the Rotordynamic Characteristics of Leakage Flows in Centrifugal Pumps. *ASME J. Fluids Eng.*, **116**, 110–115.

HIRS, G. G. 1973. A Bulk-Flow Theory for Turbulence in Lubricant Films. *ASME J. Lubr. Tech.*, April, 137–146.

JERY, B. 1986. *Experimental Study of Unsteady Hydrodynamic Force Force Matricies on Whirling Centrifugal Pump Impellers.* Ph.D. thesis, California Institute of Technology.

MARQUETTE, O. 1995. *Experimental Versus Theoretical Comparison of the Static and Dynamic Characteristics of One Smooth and Two Grooved Liquid Annular Seals with L/D = 0.457.* Tech. rept. TL-SEAL-5-95. Texas A&M Turbomachinery Laboratory.

MATROS, M., NEUMER, T., & NORDMANN, R. 1994. Identification of Rotordynamic Coefficients of Centrifugal Pump Components Using Active Magnetic Bearings. *Fifth International Symposium on Transport Phenomena and Dynamics of Rotating Machinery, ISROMAC-5*, **B**, 55–72.

NG, S. 1976. *Dynamic Response of Cavitating Turbomachines.* Ph.D. thesis, California Institute of Technology.

NORDMANN, R., & MASSMANN, H. 1984. Identification of Dynamic Coefficients of Annular Turbulent Seals. *Proceedings of Workshop on Rotordynamic Instability Problems in High-Performance Turbomachinery, NASA Conf. Publ. 2338*, 295–311.

PINKUS, O., & STERNLICHT, B. 1961. *Theory of Hydrodynamic Lubrication.* McGraw-Hill, New York.

PRESS, W., TEUKOLSKY, S., VETTERLING, W., & FLANNERY, B. 1992. *Numerical Recipes in Fortran.* Cambridge University Press.

SAN ANDRES, L. 1993. Dynamic Force and Moment Coefficients for Short Length Annular Seals. *ASME J. of Tribology*, **115**, 61–70.

SIVO, J.M., ACOSTA, A.J., BRENNEN, C.E., & CAUGHEY, T.K. 1994a. The Influence of Swirl Brakes and a Tip Discharge Orifice on the Rotordynamic Forces Generated by Discharge-to-Suction Leakage Flows in Shrouded Centrifugal Pumps. *Fifth International Symposium on Transport Phenomena and Dynamics of Rotating Machinery, ISROMAC-5*, **B**, 86–97.

SIVO, J.M., ACOSTA, A.J., BRENNEN, C.E., CAUGHEY, T.K., FERGUSON, T., & LEE, G. 1994b. Laser Velocimeter Measurements in the Leakage Annulus of a Whirling Centrifugal Pump. *ASME Laser Anemometry-1994, Advances and Applications*, **FED-191**, 111–117.

SIVO, J.M., ACOSTA, A.J., BRENNEN, C.E., & CAUGHEY, T.K. 1995. The Influence of Swirl Brakes on the Rotordynamic Forces Generated by Discharge-to-Suction Leakage Flows in Centrifugal Pumps. *ASME J. Fluids Eng.*, **117**, 104–108.

TOWNSEND, A. 1984. Axisymmetric Coutte Flow at Large Taylor Numbers. *J. Fluid Mechanics*, **144**, 329–362.

TSUJIMOTO, Y., YOSHIDA, Y., & OHASHI, H. 1997. Fluid Force Moment on a Centrifugal Impeller Shroud in Precessing Motion. *ASME J. of Fluids Engineering*, **119**, 366–371.

UY, R.V., BIRCUMSHAW, B.L., & BRENNEN, C.E. 1997. A Parametric Evaluation of the Effect of Inlet Swirl on the Rotordynamic Forces Generated by Discharge-to-Suction Leakage Flows in Shrouded Centrifugal Pump. *3rd Pumping Machinery Symposium, ASME Fluids Engineering Division Summer Meeting.*

UY, R.V., BIRCUMSHAW, B.L., & BRENNEN, C.E. 1998. Rotordynamic Forces from Discharge-to-Suction Leakage Flows in Shrouded Centrifugal Pumps: Effects of Geometry. *JSME International Journal:Fluids and Thermal Engineering*, **41, No. 1**, 208–213.

VANCE, J. 1988. *Rotordynamics of Turbomachinery.* John Wiley and Sons.

YAMADA, Y. 1962. Resistance of Flow Through an Annulus with an Inner Rotating Cylinder. *Bull. JSME*, **5, No. 18**, 302–310.

ZIRKELBACK, N., & SAN ANDRES, L. 1996. Bulk-Flow Model for the Transition to Turbulence Regime in Annular Pressure Seals. *Tribology Transactions*, **39**(4), 835–842.

Appendix A

A.1 Rocketdyne Pump Operating Conditions

Pump	H(cm)	ω(rpm)	Λ	ϕ	Eye/Tip	Length/Diameter
HPOTP	.254	31000	.524	.0464	.708	.088
HPFTP	.305	36353	.736	.007	.53	.12
MA5A-O	.635	6887	.656	.032	.602	.136
MA5A-F	.9525	6887	.693	.01	.489	.135

Table A.1: Typical pump operating conditions provided by Wei Chen. Space Shuttle Main Engine (SSME) High Pressure Oxidizer Turbo Pump (HPOTP), High Pressure Fuel Turbo Pump (HPFTP), and the Atlas MA-5A, oxidizer (-O) and fuel pump (-F).

Appendix B

Straight Seals

The SV model experienced some difficulties using the boundary conditions and convection calculation described in Chapter 4 applied to the case of turbulent annular seals. For the simple geometry of a straight seal, the SV model does well when comparing the resulting rotordynamic force coefficients to existing theoretical and experimental results, under what appear to be more restrictive assumptions at the downstream boundary.

B.1 Downstream Boundary Condition

The downstream boundary condition that was employed in this anaylsis used the first Fourier component of the pressure added to an average tangential fluid velocity at the discharge. So the constant u_θ boundary condition detailed in Chapter 4 is modified with harmonic functions derived from the pressure. The process is very similar to the constant tangential velocity approach. At the exit, an average circumferential velocity at the discharge is first calculated using the current values of the stream function, ψ using equation 4.37. The value of $\overline{u_\theta}$ is then added to the first Fourier components of the pressure, PZ_s and PZ_c. These Fourier components are evaluated using the circumferential distribution of the discharge pressure, and might be considered a simple way to introduce a static pressure contribution to the downstream boundary condition. In practice, these terms almost always went to near-zero numbers during the iterations of a computation, but during the initial part of the calculation, appeared to provide a type of harmonic restriction on u_θ in the circumferential direction. The change in ψ, the stream function at each JT (theta) location, was found using:

$$\Delta\psi = \psi_{(JS-1,JT)} - \psi_{(JS+1,JT)} + 2 * DS * H * (\overline{u_\theta} + PZ_s sin(\theta) + PZ_c cos(\theta)) \quad \text{(B.1)}$$

The calculation proceeds as described in equation 4.35.

This approach has the same advantages of averaging the tangential velocity but now a harmonic restriction on the tangential velocity is introduced. The difference it makes in the convergence of the code for straight seals is significant.

B.2 Comparisons

The simple geometry of a smooth straight seal was used as an initial test of the new SV model. Much work has been done in the area of turbulent annular seals, and different numerical approaches for determining rotordynamic behavior exist, as well as experimental data. Childs' perturbation model was initially developed for this very geometry. Three cases were considered: a seal reported by Nordmann and Massman (1984), a seal and finite difference numerical solution reported by Dietzen and Nordmann (1987), and a set of seal cases reported by Childs (1983a). The new SV model works well in predicting the rotordynamic force coefficients, but only using the Fourier component downstream boundary condition. Some comparisons using the steady pressure downstream boundary condition are shown, however these tests converged only very rarely and were not stable to small changes in parameters such as the relaxation factors.

The first example is the smooth untapered seal tested by Nordmann and Massmann (1984). This has an aspect ratio, $S/R = 1.67$, a clearance, $H/R = 0.0167$ and was tested at a Reynolds number, $Re = Q/2\pi R\nu = 5265$ (where Q is the volume flow rate through the seal). In Figure B.1, the non-dimensional rotordynamic coefficients from the experiments of Nordmann and Massmann are plotted against a flow coefficient, $\phi = Q/2\pi HR^2\Omega$. These are compared with three sets of calculated coefficients. The dashed lines are from the analytical expressions obtained by Childs' (1983a) as

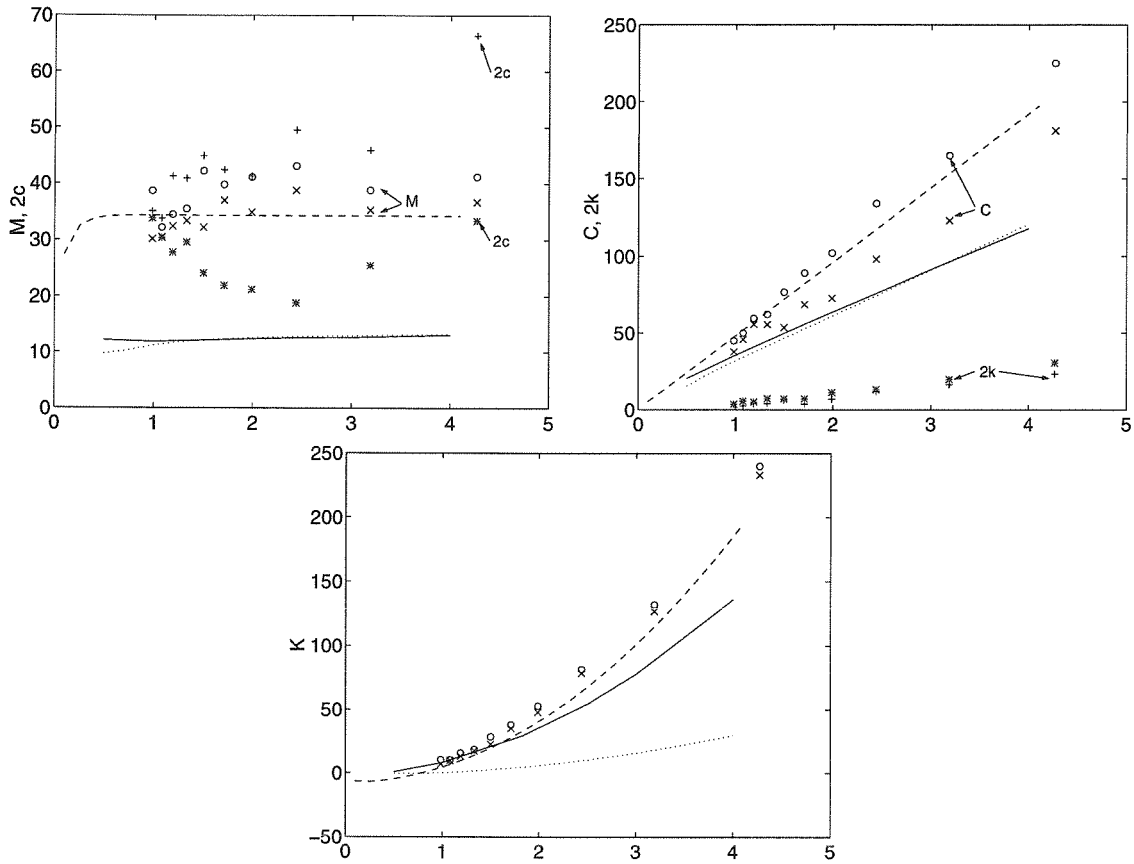

Figure B.1: Comparison of the rotordynamic coefficients from the experiments of Nordmann and Massmann (1984) on a plain, untapered, smooth seal with various calculated results as follows. Dashed line: Childs' (1983a) analytical "short seal" Dotted line: Childs' (1983b, 1987, 1989) perturbation method. Solid line: present bulk flow calculation (SV).

approximate "short seal" solutions to the bulk flow. Later Childs (1983b) published a more accurate "finite length" seal solution which involved the numerical integration of more accurate perturbation equations. The dotted lines represent the results of a similar perturbation analysis applied to the Nordmann and Massmann seal using the Caltech version of Childs' model. The differences between the two Childs' methods are substantial but similar to the differences in the examples presented by Childs (1983b). They are presumably caused by different treatments of the circumferential velocity perturbations. Note that all three sets of calculated results use an inlet swirl velocity equal to a half of the rotor tip speed.

The solid lines represent results using the present numerical method. Apart from the direct stiffness, K, they are similar to Childs' (1983b) more accurate analysis. For reasons which are presently unclear our calculations yield a K which is closer to the short seal value and to the experimental data. Thus, the primary discrepancy between the present results and the experimental data is in the added mass, M, and cross-coupled damping, c. Nordmann and Massmann's data appear questionable according to personal communication with Childs, and more recently the difficulties of accurately measuring these two coefficients have been addressed at Texas A&M, with some newer experimental data pointing to a closer agreement with the predictions of the "finite length", and hence the SV, model (Marquette, 1995).

The calculation in this case utilized the constant u_θ condition with the Fourier component of pressure, on a 40x35 size grid. The calculation also worked using the constant pressure downstream boundary condition, however a grid size with 60 nodes in the path direction and 10 nodes in the theta direction was required, and the code converged only for the particular whirl frequency ratio Ω/ω = -.7. The differences between the two downstream boundary conditions is shown in figures B.2 and B.3 in plots of the flow variables versus the mesh location. The profiles of the vorticity, pressure and velocities appear indistinguishable.

Dietzen and Nordmann also carried out a finite difference calculation to determine the rotordynamics of seals (Dietzen & Nordmann, 1987). However, rather than using the bulk flow model and correlation for the turbulent shear stresses, the Navier-Stokes equations with a $k-\varepsilon$ model for the shear stresses was used. Again, a perturbation using a linear expansion in the eccentricity was applied to the variables, and harmonic functions in the circumferential coordinate θ were assumed for the perturbation velocities. The calculation was carried out on a grid which was placed in a $r-s$ plane section of the seal.

The parameters of Dietzen's smooth untapered seal are given as an aspect ratio, S/R = 1.0, a clearance, H/R = 0.0085 and a Reynolds number, $Re = Q/2\pi R\nu$ = 4702 (where Q is the volume flow rate through the seal). In figure B.4 the non-dimensional rotordynamic force coefficients are plotted versus the flow coefficient for

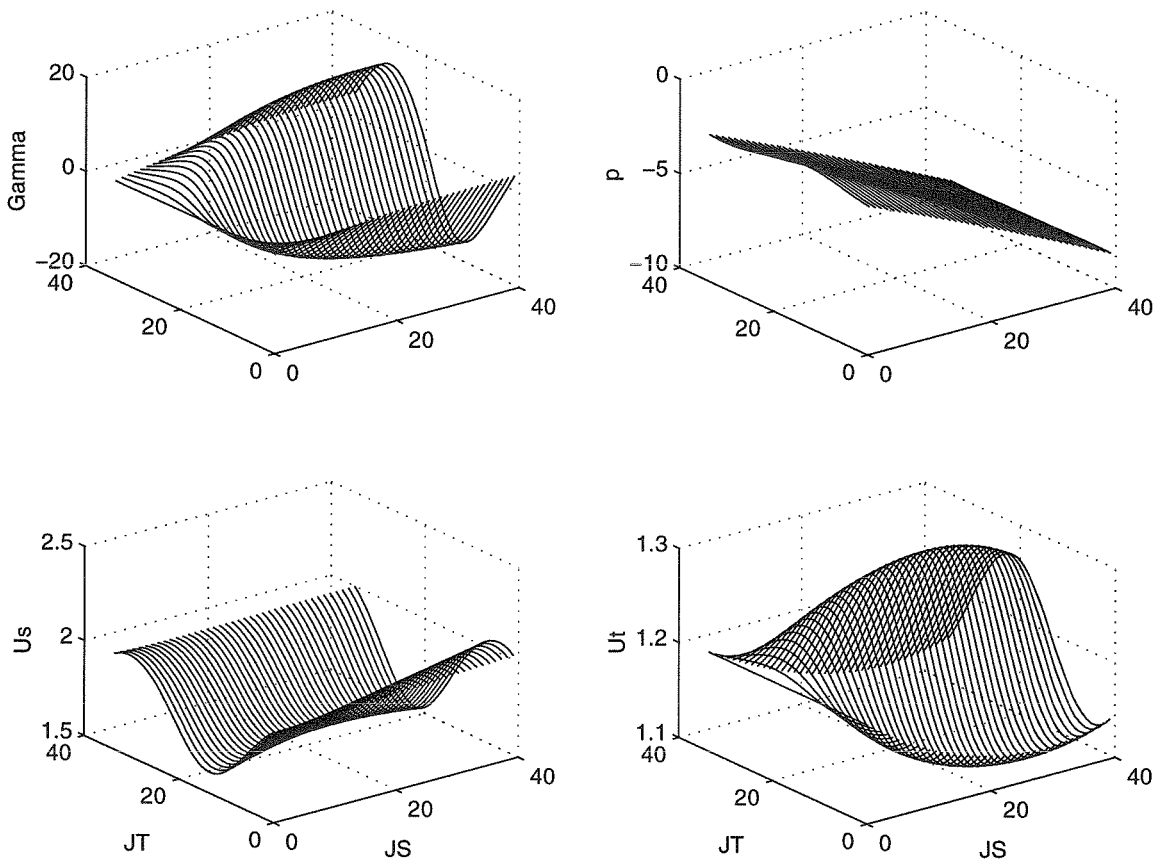

Figure B.2: Plot of flow variables against mesh location for the straight seal reported by Nordmann and Massmann. Results calculated using 40x35 grid size for the Fourier component boundary condition, whirl ratio Ω/ω = -.7 and $\phi = 1.834$.

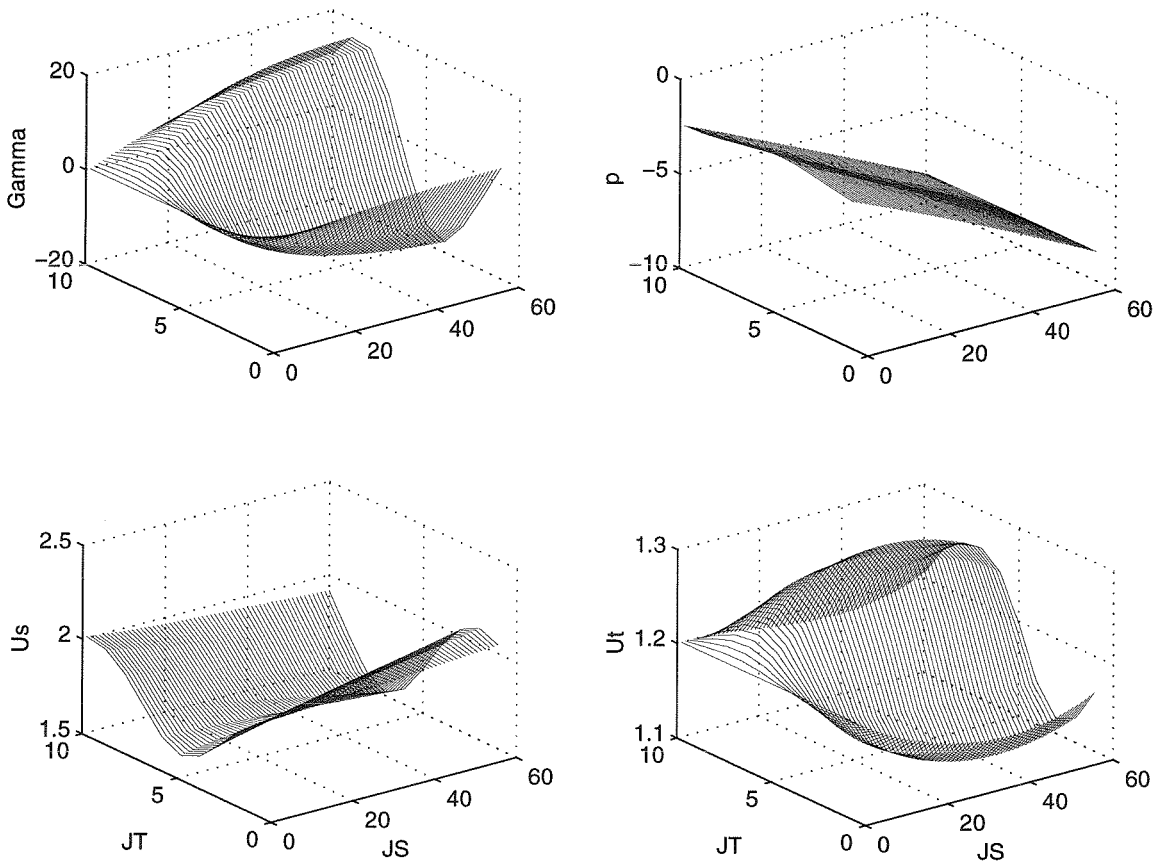

Figure B.3: Plot of flow variables against mesh location for the straight seal reported by Nordmann and Massmann. Results calculated using 60x10 grid size for the constant pressure boundary condition, a whirl ratio Ω/ω = -.7 and $\phi = 1.834$

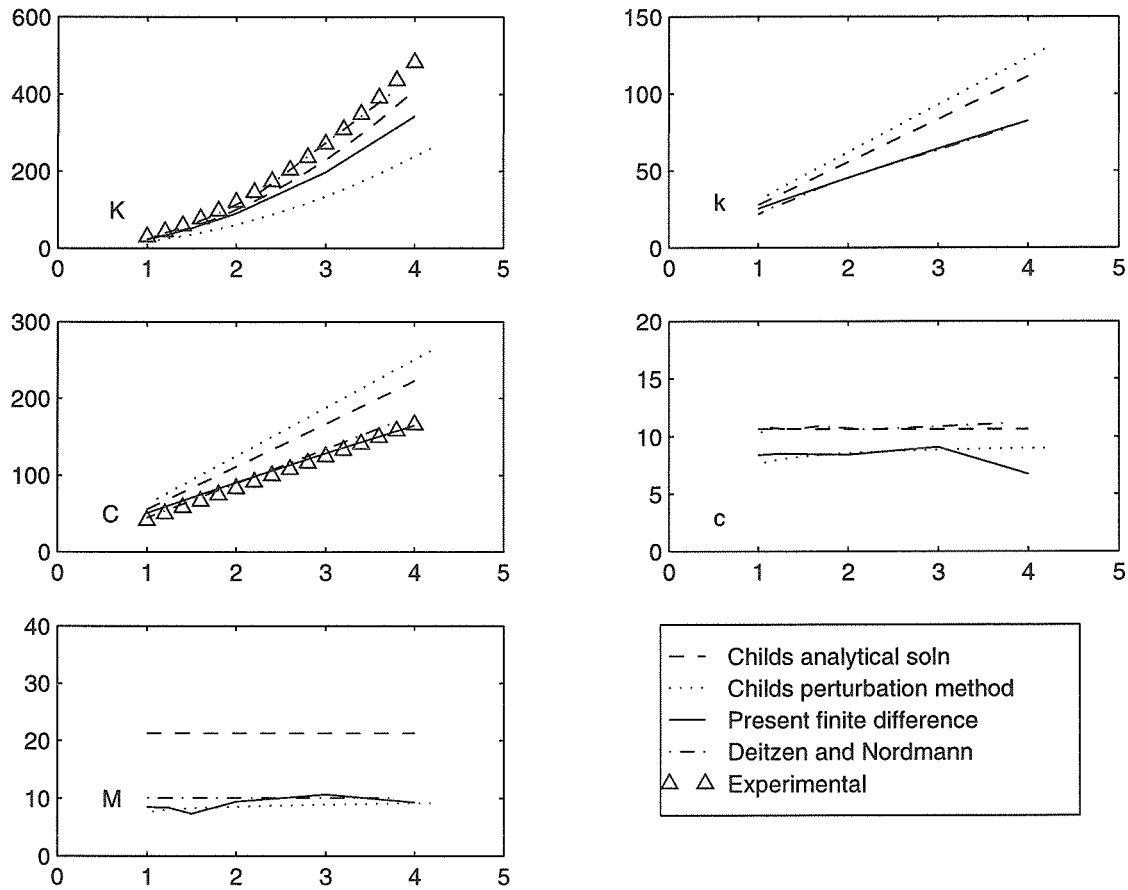

Figure B.4: Plot of rotordynamic force coefficients versus flow coefficient ϕ, for the seal reported by Dietzen and Nordmann (1987).

this seal. Again, Childs' analytical "short seal" expressions appear as the dashed line, the more accurate "finite length" seal solution is the dotted line, and the SV calculation using the Fourier component of the pressure is the solid line. The results from Deitzen's finite difference $k-\varepsilon$ method are the dot-dashed line, with experimental data also included on two of the plots.

As noted in the previous case, all the models seem to predict general trends of the rotordynamic force coefficients fairly well. The present bulk flow model seems to again more closely match the experimental and analytical data for the direct stiffness, K, relative to the "finite length" solution. Differences in the magnitude are noted between all the numerical computations and the analytical solution for the direct added

mass, M, also consistent with what was observed in the Nordmann and Massmann data.

Finally, a sample calculation for the high pressure water seal from Childs' (1983a,1983b) papers was examined. This was also the case chosen by Guinzburg (1992) for validation of the Caltech version of Childs' (1989) model to solve the bulk flow equations. The seal data are as given in Table B.1.

L/D ratio	H/R	L (m)	ϕ	Re(u_s)	ω
0.2	0.0025	0.03048	1.536	12982	3600
0.5	0.0025	0.0762	1.009	8526	3600
1.0	0.0025	0.1524	0.679	5742	3600

Table B.1: Three test cases for high pressure water seal

In the literature, no data for the eccentricity, ε, is provided, so a ratio of eccentricity to rotor radius, $\varepsilon/R = .0003$ was assumed, it being approximately 1/10th of the clearance to radius ratio. The profile of the flow variables in figure B.5 show the same trends observed in the other test cases. The lowest value of the path velocity, u_s occurs at the smallest clearance. This profile remains unchanged for values of the eccentricity from $0.0001 < \varepsilon/R < 0.0004$. As this ratio is increased or decreased past these limits, the computation becomes unstable.

The comparison of force coefficients are given in table B.2. As in the previous two sample seals, good agreement is observed between the finite difference approach and the other bulk flow solutions. The analytical solution and its assumptions about the circumferential perturbation velocity appear to cause large differences in the calculated force coefficients as the path length increases.

This case was examined using the two different downstream boundary approaches, the constant tangential velocity condition with Fourier components, and the constant static pressure condition. Figure B.5 shows the flow parameters plotted versus the mesh location for the seal with L/D = .2, using the Fourier component downstream boundary. A mesh size of 20x15 is used, and the whirl frequency is Ω/ω = -.7. Figure B.6 shows the flow parameters under the same conditions for the constant pressure boundary. Again, with an appropriate adjustment to the mesh size, in this case,

	Childs' finite length 1983b	Guinzburg's version 1992	SV code (current)	Childs' short seal (analytical) 1983a
L/D = 0.2				
K	235.6	237.83	229.95	248.84
k	53.28	70.64	48.32	64.53
C	106.6	143.82	96.93	129.06
c	5.75	2.39	6.54	10.93
M	5.75	2.43	5.63	10.93
L/D = 0.5				
K	111.70	114.60	101.88	134.06
k	130.00	135.79	124.62	158.34
C	260.00	273.13	249.24	316.68
c	33.59	29.34	35.31	49.52
M	33.62	29.41	35.01	49.52
L/D = 1.0				
K	24.7	29.07	13.62	39.71
k	238.0	234.00	241.51	363.21
C	477.4	470.50	483.03	729.6
c	102.5	96.89	124.61	165.38
M	102.6	96.86	125.01	165.47

Table B.2: Force coefficients for the high pressure water seal, (Guinzburg, 1992) and current finite difference model.

60x10, similar profiles for the calculated variables are observed. Also, this is again the only whirl frequency ratio at which the constant pressure boundary condition converges, and so the Fourier component condition was used for the reported force coefficients.

For reasons which deserve further investigation, this downstream boundary condition seemed to give very good predictions of the rotordynamic forces in smooth seals. There is some indication that the constant pressure condition may sometimes work as well, but appears for the moment to be very unstable.

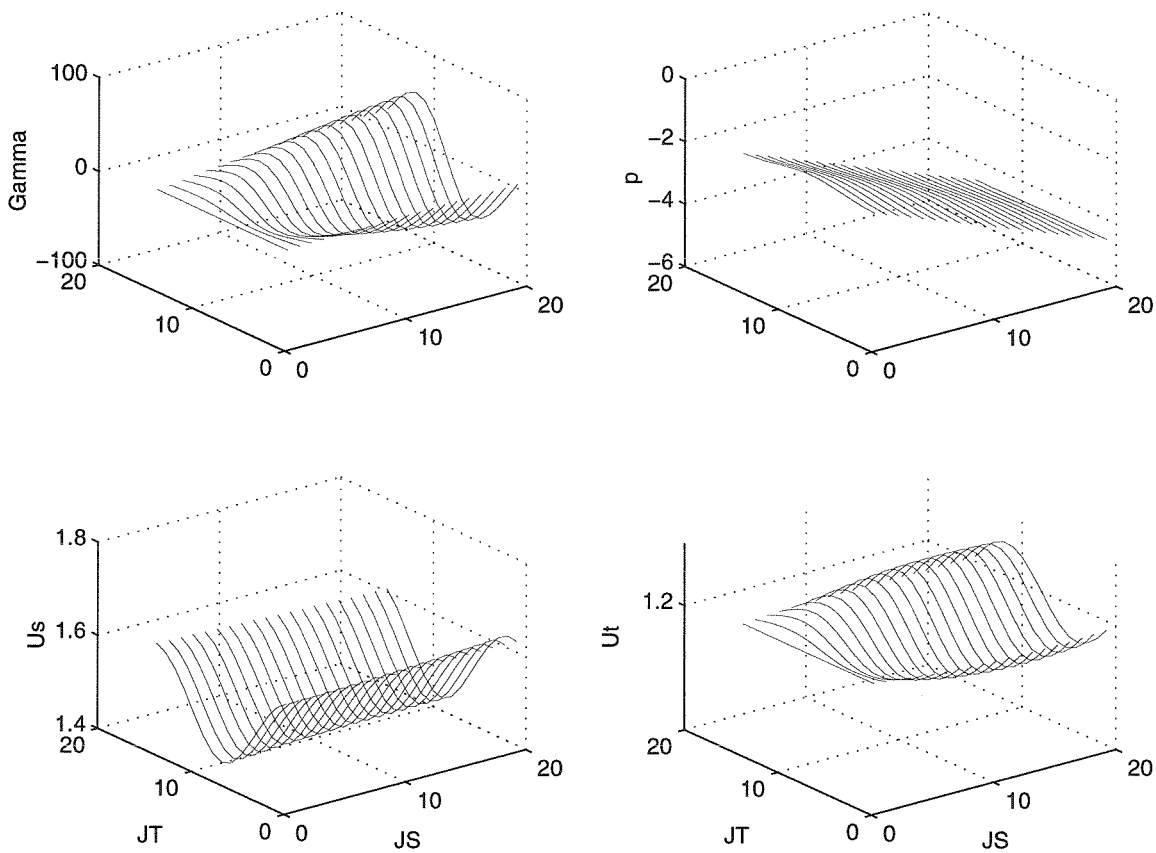

Figure B.5: Plot of flow variables against mesh location for the straight seal reported by Childs. Results calculated using 20x15 grid size for the Fourier component boundary condition, a whirl ratio Ω/ω = -.7, and L/D = .2.

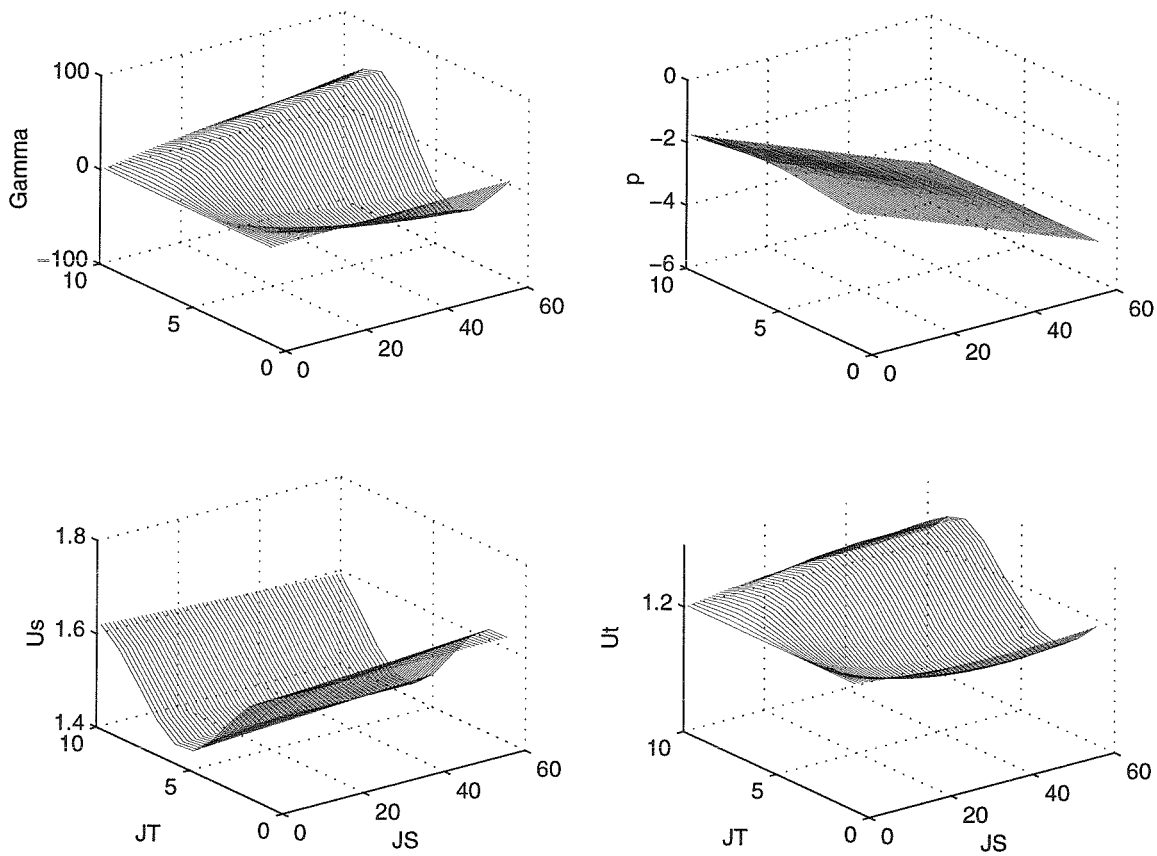

Figure B.6: Plot of flow variables against mesh location for the straight seal reported by Childs. Results calculated using 60x10 grid size for the constant pressure boundary condition, a whirl ratio Ω/ω = -.7 and L/D = .2.

```
c     PROGRAM BFLFD.F - BULK FLOW MODEL
c
c     This is the program which uses a finite difference scheme
c     to solve the Stream Function Vorticity method of the bulk
c     flow equations.
c

      INTEGER ITER, ITERB, JSQ, JST, JTQ, JTT, JS, JT, ITX, ITY, ITYT

      REAL  DZL, DRR, HAA, EP, OM, DET, DES, DSL, FI, UTO, RE, CAS, CAR
      REAL  ORF, DELPSI, ORFB, UTI
      REAL  RES, RESG, RESX, PSJ, FTN, FTT

      DIMENSION R(400),RS(400),RSS(400),HA(400),HB(400,55),S(400),T(55)
      DIMENSION US(400,55),UT(400,55),GS(400,55),GR(400,55)
      DIMENSION TKA(400,55),TKB(400,55)
      DIMENSION PSI(400,55),HE(400,55),PR(400,55),TKC(400,55)
      DIMENSION RHS(400,55)
      DIMENSION GAM(400,55),TTR(400,55)
      DIMENSION DBS(400)

      COMMON ITER, ITERB, JSQ, JST, JTQ, JTT, JS, JT, ITX, ITY, ITYT
      COMMON DZL, DRR, HAA, EP, OM, DET, DES, DSL, FI, UTO, RE, CAS, CAR
      COMMON ORF, DELPSI, ORFB, UTI, PSIDS, WF
      COMMON RES, RESG, RESX, PSJ, RESM, RESMG, DPSI
      COMMON R, RS, RSS, HA, HB, S, T, US, UT, GS, GR, DBS
      COMMON TKA, TKB, PSI, HE, PR, TKC, RHS, GAM, TTR, FTN, FTT
```

```
      open(10,file='psout.dat',status='old')
      open(11,file='fcs.dat',status='old')
      open(12,file='delp.dat', status='old')

        PRINT  *, 'BLKFL - BULK FLOW PROGRAM'
        PRINT  *, '**************************'

c --  GEOMETRY INPUT:
        CALL INDATA

c --  FLOW DATA INPUT:
        DO 104, k=1,13
           OM = -.9+.1*k

1001    CALL INDATB

c -- Initial set up for stream function:
        DA = DELPSI / (JTT - 3)
        DO 11 JT = 2, JTT + 1
        DO 10 JS = 1, JST + 1
        PSI(JS, JT) = DA * (JT - 3)
        GAM(JS,JT) = 0.0
        RHS(JS, JT) = 0.0
   10   CONTINUE
   11   CONTINUE


c     Set iterations in main calculation and in Solveb.
```

```
      ITER = 50
      ITERB = 20

c     These numbers are for convergence of the forces and
c     control over calculation

      ITYT = 0
      FTN = 0.01
      FTT = 0.01

c     Solveb uses velocities to figure downstream boundary.
c     First iteration through need to set the velocities

      CALL VELOCI

      DO 37 JT = 1, JTT+2
      DO 36 JS = 1, JST+1
      UT(JS,JT) = UTO
 36   CONTINUE
 37   CONTINUE

c     Main calculation loop

 17   CONTINUE

         ITYT = ITYT + 1
         ODFN = FTN
         ODFT = FTT
```

```
1630      DO 18 ITX = 1, ITER
             CALL SOLVEB
             CALL VELOCI
             CALL SOLVEA
18        CONTINUE

c     calculate percentage error in forces
c     Conditional to move to next whirl frequency when
c     forces are within 5%

      DT = ABS((ODFT-FTT)/odft)
      DN = ABS((ODFN-FTN)/odfn)

      print *, ftn, ftt

      IF(DN.GT.0.05.or.DT.GT.0.05.or.ITYT.LT.4) GOTO 17

c     print out US, UT, PR, GAM for check of exit condition

345   do 106 JS = 2,JST-1
       do 105 JT = 3,JTT-1
       write(10,*) PR(JS,JT), US(JS,JT), UT(JS,JT), GAM(JS,JT)
105     continue
106     continue

c     This section calculates the delta p pressure difference.

      fsum = 0.0
      rsum = 0.0
```

```
      do 107 JT = 3, JTT-1
         fsum = PR(2,JT)+fsum
         rsum = PR(JST-1,JT)+rsum
 107     continue

      presd = (fsum-rsum)/JTQ
      write(12,*) presd
      write(11,*) OM, FTN, FTT

 104    continue

1000    END


      SUBROUTINE INDATA

      COMMON ITER, ITERB, JSQ, JST, JTQ, JTT, JS, JT, ITX, ITY, ITYT
      COMMON DZL, DRR, HAA, EP, OM, DET, DES, DSL, FI, UTO, RE, CAS, CAR
      COMMON ORF, DELPSI, ORFB, UTI, PSIDS, WF
      COMMON RES, RESG, RESX, PSJ, RESM, RESMG, DPSI
      COMMON R(400),RS(400),RSS(400),HA(400),HB(400,55),S(400),T(55)
      COMMON US(400,55),UT(400,55),GS(400,55),GR(400,55), DBS(400)
      COMMON TKA(400,55), TKB(400,55)
      COMMON PSI(400,55),HE(400,55),PR(400,55),TKC(400,55),RHS(400,55)
      COMMON GAM(400,55), TTR(400,55), FTN, FTT

C -- SUBROUTINE TO INPUT GEOMETRIC AND OTHER DATA TO PROGRAM

        DZL = 0.5
        DRR = 0.5
```

```
        HAA = .03
        EP = .003
        JSQ = 50
        JTQ = 10
        GOTO 1600

c       LENGTH/R_1                = DZL
c       R_2/R_1                   = DRR
c       CLEARANCE/R_1             = HAA
c       ECCENTRICITY/R_1          = EP
c       WHIRL FREQUENCY RATIO     = OM
c       NUMBER OF S INCCENTS      = JSQ
c       NUMBER OF THETA INCCENTS  = JTQ

C --    The inlet boundary is at JS=2
C --    The discharge boundary is at JS=JST
C --    The Theta=0 line is at JT=3
C --    The Theta=2*Pi line is at JT=JTT

C --    HERE WE NEED TO INPUT THE FUNCTIONS R(S) and HA(S)
C --    FOR THE MOMENT WE INPUT THE CONICAL GEOMETRY:

1600    JST = JSQ + 2
        DSL = SQRT(DZL*DZL + (1.0 - DRR)*(1.0-DRR))
        DES = DSL / JSQ
        DO 30 JS = 1, JST + 1
        HA(JS) = HAA
        R(JS) = 1.0 - (JS - 2) * (1.0 - DRR) / JSQ
        S(JS) = (JS - 2) * DES
        RS(JS) = -(1.0 - DRR) / DSL
```

```
        RSS(JS) = 0.0
   30   CONTINUE

C --  NOW TO SET UP THE THETA GEOMETRY:
        JTT = JTQ + 3
        DET = 2.0 * 3.14159265/ JTQ

        DO 31 JT = 1, JTT + 2
        T(JT) = DET * (JT - 3)
   31   CONTINUE

C --  NOW TO SET UP CLEARANCE GEOMETRY:
        DO 33 JS = 1, JST + 1
        DO 32 JT = 1, JTT + 2
        HB(JS, JT) = HA(JS)+EP * COS(T(JT)) * SQRT(1.0 - RS(JS)*RS(JS))
   32   CONTINUE
   33   CONTINUE

      RETURN
      END

      SUBROUTINE INDATB

      COMMON ITER, ITERB, JSQ, JST, JTQ, JTT, JS, JT, ITX, ITY, ITYT
      COMMON DZL, DRR, HAA, EP, OM, DET, DES, DSL, FI, UTO, RE, CAS, CAR
      COMMON ORF, DELPSI, ORFB, UTI, PSIDS, WF
      COMMON RES, RESG, RESX, PSJ, RESM, RESMG, DPSI
      COMMON R(400),RS(400),RSS(400),HA(400),HB(400,55),S(400),T(55)
      COMMON US(400,55),UT(400,55),GS(400,55),GR(400,55), DBS(400)
      COMMON TKA(400,55), TKB(400,55)
```

```
      COMMON PSI(400,55),HE(400,55),PR(400,55),TKC(400,55),RHS(400,55)
      COMMON GAM(400,55), TTR(400,55), FTN, FTT

C -- INPUT FLOW DATA:

        FI = 0.06
        UTI = 0.5
        RE = 1026346.0
        CAS = .079
        CAR = .079

       ORF =  1.5
       ORFB = 1.2

        PSIDS = 0.0
        GOTO 1701

c     FLOW COEFFICIENT                      =  FI
c     INLET SWIRL VELOCITY, U_theta         =  UTI
c     REYNOLDS NUMBER, Omega*R1**2/NU       =  RE
c     SHEAR COEFFICIENT, AS                 =  CAS
c     SHEAR COEFFICIENT, AR                 =  CAR
c     NUMBER OF ITERATIONS                  =  ITER
c     NUMBER OF ITERATIONS ON PSI           =  ITERB
c     OVER-RELAXATION FACTOR FOR FIELD      =  ORF
c     OVER-RELAXATION FACTOR FOR BOUNDARY   =  ORFB

 1701   DELPSI = 2.0 * 3.1415 * FI * HAA
        PSIDS = 0.0
        UTO = UTI - OM
```

```
      RETURN
      END

      SUBROUTINE SHEARS

      COMMON ITER, ITERB, JSQ, JST, JTQ, JTT, JS, JT, ITX, ITY, ITYT
      COMMON DZL, DRR, HAA, EP, OM, DET, DES, DSL, FI, UTO, RE, CAS, CAR
      COMMON ORF, DELPSI, ORFB, UTI, PSIDS, WF
      COMMON RES, RESG, RESX, PSJ, RESM, RESMG, DPSI
      COMMON R(400),RS(400),RSS(400),HA(400),HB(400,55),S(400),T(55)
      COMMON US(400,55),UT(400,55),GS(400,55),GR(400,55), DBS(400)
      COMMON TKA(400,55), TKB(400,55)
      COMMON PSI(400,55),HE(400,55),PR(400,55),TKC(400,55),RHS(400,55)
      COMMON GAM(400,55), TTR(400,55), FTN, FTT

C -- Calculates the viscous shear stress terms.
C     Using same strategy as before, bulk flow model

      DC = (RE * HB(JS, JT))**(-.25)

      DAX = .5 * CAS * DC * ((US(JS, JT)*US(JS,JT) + (UT(JS, JT)
     1 + OM * R(JS))*(UT(JS, JT) + OM * R(JS)))**.375)

      DBX = .5 * CAR * DC * ((US(JS, JT)*US(JS,JT) + (UT(JS, JT) -
     1 (1.0 - OM) * R(JS))*(UT(JS, JT) - (1.0 - OM) * R(JS)))**.375)

         GS(JS,JT) = ABS(DAX)/HB(JS,JT)
         GR(JS,JT) = ABS(DBX)/HB(JS,JT)
```

```
      RETURN
      END


      SUBROUTINE SOLVEA

      COMMON ITER, ITERB, JSQ, JST, JTQ, JTT, JS, JT, ITX, ITY, ITYT
      COMMON DZL, DRR, HAA, EP, OM, DET, DES, DSL, FI, UTO, RE, CAS, CAR
      COMMON ORF, DELPSI, ORFB, UTI, PSIDS, WF
      COMMON RES, RESG, RESX, PSJ, RESM, RESMG, DPSI
      COMMON R(400),RS(400),RSS(400),HA(400),HB(400,55),S(400),T(55)
      COMMON US(400,55),UT(400,55),GS(400,55),GR(400,55), DBS(400)
      COMMON TKA(400,55), TKB(400,55)
      COMMON PSI(400,55),HE(400,55),PR(400,55),TKC(400,55),RHS(400,55)
      COMMON GAM(400,55), TTR(400,55), FTN, FTT

C -- To integrate to find Gamma:

C -- To set pressure at inlet:
        DO 40 JT = 2, JTT + 1
        DE = UT(2,JT)*UT(2,JT)+US(2,JT)*US(2,JT)-(OM*R(2))*(OM*R(2))
        PR(2, JT) = HE(2, JT) - .5 * DE
   40   CONTINUE

C -- To calculate GS, GR, TKA, TKB for all points:
        DO 42 JS = 2, JST
        DO 41 JT = 2, JTT + 1
        CALL SHEARS
        DA = GR(JS, JT) + GS(JS, JT)
        DB = UT(JS, JT) + OM * R(JS)
```

```
      DC = GR(JS, JT) * R(JS)
      TKA(JS, JT) = R(JS) * (DA * DB - DC)
      TKA(1,JT) = TKA(2,JT)
      TKB(JS, JT) = US(JS, JT) * DA
C      TKC(JS, JT) = DC * UT(JS, JT) -
C     1    DA * (US(JS, JT)*US(JS,JT) + UT(JS, JT) * DB)

   41 CONTINUE
   42 CONTINUE

c     Convection calculation.  Use relaxation of the diffusion
c     equation.

      DO 92 I = 1, ITERB

      DO 46 JS = 3, JST
         DO 43 JT = 3, JTT-1

      RHSE = ((TKA(JS,JT)-TKA(JS-2,JT))/(2*DES)-
     2 (TKB(JS-1,JT+1)-TKB(JS-1,JT-1))/
     3 (2*DET))/(R(JS-1)*HB(JS-1,JT))

      DGAM = (RHSE-UT(JS-1,JT)/R(JS-1)*(GAM(JS-1,JT+1)-GAM(JS-1,
     1 JT-1))/(2*DET))/US(JS-1,JT)

      GAM(JS,JT) = GAM(JS-1,JT)+1.1*DGAM*DES

C     Now project head forward using same technique

      HHSE = -1.0*UT(JS-1,JT)*TKA(JS-1,JT)/R(JS)
```

```
     2  -TKB(JS-1,JT)*(R(JS-1)*US(JS-1,JT))

        DHE = (HHSE-UT(JS-1,JT)*(HE(JS-1,JT+1)-HE(JS-1,
     1  JT-1))/(2*DET))/(US(JS-1,JT)*R(JS-1))

        HE(JS,JT) = HE(JS-1,JT)+1.1*DHE*DES

 15       DE = UT(JS,JT)*UT(JS,JT)+US(JS,JT)*US(JS,JT)
     4  -(OM * R(JS))*(OM*R(JS))
        PR(JS, JT) = HE(JS, JT) - .5 * DE

    43  CONTINUE

C -- Set boundary values under Theta=0 boundary:
        DO 44 JT = 1, 2
        GAM(JS, JT) = GAM(JS, JT + JTT - 3)
        HE(JS, JT) = HE(JS, JT + JTT - 3)
        PR(JS, JT) = PR(JS, JT + JTT - 3)
    44  CONTINUE

C -- Set boundary values above Theta=2*Pi boundary:
        DO 45 JT = JTT, JTT + 2
        GAM(JS, JT) = GAM(JS, JT - JTT + 3)
        HE(JS, JT) = HE(JS, JT - JTT + 3)
        PR(JS, JT) = PR(JS, JT - JTT + 3)
    45  CONTINUE

    46  CONTINUE

 92     CONTINUE
```

```
 61        CONTINUE

c     This is the extrapolation of upstream gamma
c     so that the initial gamma effect will be wiped
c     out.

          DO 23 JT = 1, JTT + 2
          GAM(1,JT) = (3*GAM(3,JT)-2*GAM(4,JT))
          GAM(2,JT) =  (2*GAM(3,JT)-GAM(4,JT))
 23       continue

C -- To calculate right hand side:
 1631      DO 48 JS = 1, JST + 1
           DO 47 JT = 1, JTT + 2
           RHS(JS, JT) = (R(JS)*R(JS)) * HB(JS, JT) * GAM(JS, JT)
   47    CONTINUE
   48    CONTINUE

C -- To calculate rotordynamic forces, FN and FT:
          FTN = 0
          FTT = 0
          FTNV = 0
          FTTV = 0

          DO 50 JS = 2, JST
          DFN = 0
          DFT = 0
          DFNV = 0
```

```
      DFTV = 0

      DO 49 JT = 4, JTT

      DFN = DFN + .5*R(JS)*DET * (COS(DET * (JT - 4)) * PR(JS, JT - 1)
     1   + COS(DET * (JT - 3)) * PR(JS, JT))
      DFT = DFT + .5*R(JS)*DET * (SIN(DET * (JT - 4)) * PR(JS, JT - 1)
     2    + SIN(DET * (JT - 3)) * PR(JS, JT))
      DFNV = DFNV + .5 * DET * (SIN(DET * (JT - 4)) * TTR(JS, JT - 1)
     3    + SIN(DET * (JT - 3)) * TTR(JS, JT))
      DFTV = DFTV - .5 * DET * (COS(DET * (JT - 4)) * TTR(JS, JT - 1)
     4    + COS(DET * (JT - 3)) * TTR(JS, JT))

   49 CONTINUE

      DFN = DFN * SQRT(1.0 - RS(JS)*RS(JS))
      DFT = DFT * SQRT(1.0 - RS(JS)*RS(JS))
      DFNV = DFNV * SQRT(1.0 - RS(JS)*RS(JS))
      DFTV = DFTV * SQRT(1.0 - RS(JS)*RS(JS))

      IF (JS.EQ.2) GOTO 1640

      FTN = FTN + .5 * (DFN + DFNP) * DES
      FTT = FTT + .5 * (DFT + DFTP) * DES
      FTNV = FTNV + .5 * (DFNV + DFNPV) * DES
      FTTV = FTTV + .5 * (DFTV + DFTPV) * DES

 1640 DFNP = DFN
      DFTP = DFT
      DFNPV = DFNV
```

```
        DFTPV = DFTV

   50   CONTINUE

c       NORM is a factor which makes this calculation's
c       non-dimensionalization match that of the experiments
c       and that of Adiel's thesis, and of course, the
c       full numerical integration code.  NORM is NOT a normal force.

        NORM = 1.0/(3.14159*DZL*EP)
        FTN = (FTN+FTNV)*NORM
        FTT = (FTT+FTTV)*NORM

 1641 RETURN

      END

      SUBROUTINE SOLVEB

c      DIMENSION DBSI(400)

      COMMON ITER, ITERB, JSQ, JST, JTQ, JTT, JS, JT, ITX, ITY, ITYT
      COMMON DZL, DRR, HAA, EP, OM, DET, DES, DSL, FI, UTO, RE, CAS, CAR
      COMMON ORF, DELPSI, ORFB, UTI, PSIDS, WF
      COMMON RES, RESG, RESX, PSJ, RESM, RESMG, DPSI
      COMMON R(400),RS(400),RSS(400),HA(400),HB(400,55),S(400),T(55)
      COMMON US(400,55),UT(400,55),GS(400,55),GR(400,55), DBS(400)
      COMMON TKA(400,55), TKB(400,55)
      COMMON PSI(400,55),HE(400,55),PR(400,55),TKC(400,55),RHS(400,55)
      COMMON GAM(400,55), TTR(400,55), FTN, FTT
```

```
C -- Solves the stream function equation given current Gamma values.

C -- Stream Function iteration loop:

 3520    DO 80 IT = 1, ITERB

c -- Set boundary values upstream of inlet:
        DO 51 JT = 3, JTT - 1
        UT(2, JT) = UTO
        PSI(1, JT) = PSI(3, JT) + 2 * DES * HB(2, JT) * UTO
  51    CONTINUE

c     Downstream boundary condition, written with Ut, Us
c     constant pressure in this case

 3543    DD = 0
         BD = 0
        DO 53 JT = 3, JTT - 1
        DE = US(JST,JT)
        DF = UT(JST,JT)
        DD = DD + 2.0*HE(JST, JT)-DE*DE-DF*DF+OM*R(JST)*OM*R(JST)
  53    CONTINUE

        PPSIDS = DD / (JTT - 3)

        DO 54 JT = 3, JTT - 1
        DE = US(JST,JT)
        DF = UT(JST,JT)
```

```
      DO 55 I = 1, 25

         IF(DF.EQ.0.0) GOTO 3540

      RESB = DF*DF+PPSIDS-2.0*HE(JST, JT)+DE*DE-OM*R(JST)*OM*R(JST)
      DRESB = 2*DF
      DF = DF - 1.0*RESB/DRESB

 55   CONTINUE

 3540   DC = DF
 3541   DP = PSI(JST - 1, JT) - 2 * DES *
     1  HB(JST, JT) * DC - PSI(JST + 1, JT)

      PSI(JST + 1, JT) = PSI(JST + 1, JT) + ORFB * DP

  54   CONTINUE

C -- Set boundary values under Theta=0 boundary:
 3542  DO 62 JT = 1, 2
      DO 61 JS = 1, JST + 1
      PSI(JS, JT) = PSI(JS, JT + JTT - 3) - DELPSI
   61 CONTINUE
   62 CONTINUE

C -- Set boundary values above Theta=2*Pi boundary:
      DO 64 JT = JTT, JTT + 2
      DO 63 JS = 1, JST + 1
      PSI(JS, JT) = PSI(JS, JT - JTT + 3) + DELPSI
   63 CONTINUE
```

```
   64   CONTINUE

C -- Rezero all psi:

        DA = PSI(2,3)
        DO 66 JT = 1, JTT + 2
        DO 65 JS = 1, JST + 1
         PSI(JS,JT) = PSI(JS,JT)-DA
   65   CONTINUE
   66   CONTINUE

C -- Relaxation of general points:
        DO 69 JT = 3, JTT - 1

        DO 68 JS = 2, JST

        DA = .5 * (R(JS + 1) + R(JS))
        DB = 2.0 * DA / (HB(JS + 1, JT) + HB(JS, JT))
        DC = (PSI(JS + 1, JT) - PSI(JS, JT)) / DES
        DD = DB * DC - OM * DA*DA
        DE = .5 * (R(JS) + R(JS - 1))
        DF = 2.0 * DE / (HB(JS, JT) + HB(JS - 1, JT))
        DG = (PSI(JS, JT) - PSI(JS - 1, JT)) / DES
        DH = DF * DG - OM * DE*DE

        DJ = 2.0 / (HB(JS, JT + 1) + HB(JS, JT))
        DK = DJ * (PSI(JS, JT + 1) - PSI(JS, JT)) / DET
        DL = 2.0 / (HB(JS, JT) + HB(JS, JT - 1))
        DM = DL * (PSI(JS, JT) - PSI(JS, JT - 1)) / DET
```

```
        RES = R(JS) * (DD - DH) / DES + (DK - DM) / DET - RHS(JS, JT)
        RESG = -R(JS) * (DB + DF) / (DES*DES) - (DJ + DL) / (DET*DET)

C -- Relaxation:
        PSI(JS, JT) = PSI(JS, JT) - ORF * RES / RESG

   68   CONTINUE
   69   CONTINUE

  80  CONTINUE

      RETURN
      END

      SUBROUTINE VELOCI

      COMMON ITER, ITERB, JSQ, JST, JTQ, JTT, JS, JT, ITX, ITY, ITYT
      COMMON DZL, DRR, HAA, EP, OM, DET, DES, DSL, FI, UTO, RE, CAS, CAR
      COMMON ORF, DELPSI, ORFB, UTI, PSIDS, WF
      COMMON RES, RESG, RESX, PSJ, RESM, RESMG, DPSI
      COMMON R(400),RS(400),RSS(400),HA(400),HB(400,55),S(400),T(55)
      COMMON US(400,55),UT(400,55),GS(400,55),GR(400,55), DBS(400)
      COMMON TKA(400,55), TKB(400,55)
      COMMON PSI(400,55),HE(400,55),PR(400,55),TKC(400,55),RHS(400,55)
      COMMON GAM(400,55), TTR(400,55), FTN, FTT

C -- Evaluate all velocities Us and Ut:
        DO 211 JQT = 1, JTT + 1
        DO 210 JQS = 1, JST + 1
```

```
      DA = 2.0 * DET * R(JQS) * HB(JQS, JQT)
      DB = 2.0 * DES * HB(JQS, JQT)
      IF (JQT.EQ.1.OR.JQT.EQ.JTT + 1) GOTO 207
      US(JQS, JQT) = (PSI(JQS, JQT + 1) - PSI(JQS, JQT - 1)) / DA
207   IF (JQS.EQ.1.OR.JQS.EQ.JST + 1) GOTO 210
      UT(JQS, JQT) = -(PSI(JQS + 1, JQT) - PSI(JQS - 1, JQT)) / DB

210       CONTINUE
211       CONTINUE


    RETURN
    END
```